



Atmospheric and
Environmental Research, Inc.

Momentum and energy assessments with NASA and other model and data assimilation systems

Final report for project NAS5-98179
(AER project P785)

David Salstein
Peter Nelson
Wenjie Hu

Atmospheric and Environmental Research, Inc
131 Hartwell Avenue
Cambridge, MA 02139

(salstein@aer.com)

Final report

During the project we computed work in a number of areas which are outlined below.

1. Study of aspects of dynamics around the Himalayan Mountains of Asia. We are using the framework of global and local angular momentum to look at how pressure variations produce torques against the mountains of Asia to change the angular momentum there. We have started assessing the differences between the NASA GEOS and NCEP analyses in this context. Results are given in attachment 1.
2. Study of the how models participating in the second Atmospheric Model Intercomparison Project (AMIP-2) have success in simulating the angular momentum of the atmosphere. To date, 20 models have submitted results for this assessment. Earlier results with 2 models are given in the attached set of figures from a presentation given at the International Union of Geodesy and Geophysics symposium at Birmingham, UK. Current results with a set of 15 models that participated in both AMIP-1 and AMIP-2 show that the mean bias has increased; however, the improvement in the subtropical jet strength and the tropical upper troposphere and stratosphere, was not matched by improvement in the higher latitude upper atmosphere when comparing the AMIP-2 models to the earlier AMIP-1 set. So mean signals that largely cancelled each other in AMIP-1 no longer do so in AMIP-2. The seasonal and interannual signals show, however, that AMIP 2 signals are an improvement. The results are scheduled for presentation at the American Meteorological Society's 13th Symposium on Global Change and Climate Variations; a copy of an earlier extended abstract for the presentation is appended here. Some additional figures are appended.
3. Study of aspects of the energetics and momentum cycle from certain runs from the Goddard Laboratory for Atmospheres. Here results from the relaxed Arakawa-Schubert run will be presented. Results are given in attached figures.
4. Study of aspects of dynamics of torques and angular momentum based on the Goddard GEOS and other analyses. We also have examined regions where rapid changes in the angular momentum from mass shifts have yielded large variability in momentum. Figures illustrating these points are given below.
5. Study of the how models participating in the second Atmospheric Model Intercomparison Project (AMIP-2) have success in simulating certain large-scale quantities. Besides NASA models, a fair number of others have submitted results to the archives of AMIP-2. We have enlarged our first focus on angular momentum of the atmosphere to include large-scale water vapor and vapor fluxes, and other aspects of atmospheric variability. To date, 16 models results are available for this assessment. Some of our results from the AMIP-2 experiment for water vapor are given as Attachment 2. This includes an analysis of the model results given for all of and for Southwest North America.

6. Study of the energetics and momentum cycle from certain runs from the Goddard Laboratory for Atmospheres (latest simulation: Sud and Walker, 1999), and other models as well. Some results are synthesized in "Diabatic heating and the Atmospheric Energy Cycle," by D. Salstein, to appear in the proceedings of the Jose P. Peixoto Memorial Symposium, University of Lisbon Press, which is given here as Attachment 3. Further work in this topic is being prepared for the chapter on diabatic heating of the revised edition of *Physics of Climate* (originally Peixoto and Oort 1992). We have also assessed such changes in diabatic heating and related energetics in the community climate model (CCM3) of NCAR, especially with a new radiation code developed at AER. One example of the figures is the generation of APE by latent heating, difference between the CCM3 with and without the new radiation code, named RRTM. Techniques for the generation of APE were developed under this NASA project and its predecessors. One such figure, given as an example, is included as Fig. 3a.1, following Attachment 3.
7. Analyzing modes of climate of the atmosphere, especially the Arctic and North Atlantic Oscillations. This topic relates to the interannual variability found in the NASA Goddard Models, GEOS-1 DAS reanalysis, and other reanalyses. The work was done collaboratively with Judah Cohen of AER. The abstract of a paper on this topic is given as Attachment 4. It has been accepted for publication in *Geophysical Research Letters*.
8. We published a paper entitled: Cohen, J.D., D.A. Salstein, and R.D. Rosen, 2000: Interannual variability in the meridional transport of water vapor, *J. Hydrometeorology*, 547-553.

David Salstein
Principal Investigator

1. PRESSURE PATTERNS RELATED TO MOUNTAIN TORQUES OVER EURASIA

A portion of this study is dedicated to documenting synoptic-scale fluctuations in mountain torques associated with the Himalayan mountains of Asia, and determining the atmospheric sources of these fluctuations. To complete this task, we computed daily-averaged fields of global mountain torques based on topography and surface pressure from the NASA GEOS-1 assimilation system (hereafter "GEOS") for the years 1981 to 1994. We have also acquired global mountain torques for the same years from the NCEP/NCAR (hereafter "NCEP") reanalysis system that were computed at NOAA/CDC. The mountain torques were then area-averaged within in a region bounded by 20°N to 60°N, 20°W to 180°W; this region will be referred to as "Eurasia" in this report.

1) Differences between Eurasia mountain torques in GEOS and NCEP analyses

Figure 1 shows a 1-year time series of GEOS and NCEP Eurasia mountain torque. The timing and amplitude of sub-monthly mountain torque fluctuations agree fairly well in the two time series, and the amplitude of these sub-monthly fluctuations is greater in the cool than in the warm season. There is evidence for a positive bias in mountain torque in the GEOS compared to the NCEP values, and this bias is particularly noticeable in the cool season. For the entire time series, the difference in the means is about 4.7 Hadleys (1 Hadley = 10^{18} kg m² s⁻²). The seasonal dependence of the positive bias in the GEOS mountain torques is shown more clearly by the differences in monthly mean Eurasia mountain torque between the two data sets (Fig. 2). These differences range from 8.5 Hadleys in January to 2 Hadleys in July.

To investigate some possible causes of this discrepancy, we plot the differences in January and July sea level pressure in Fig. 3, as well as the topographic heights to define the Himalayas. We choose sea level pressure rather than surface pressure here because the consistent definition of sea level in the two analyses allows us to more clearly isolate differences in pressure that are due purely to the mass field from those that are due to

differences in topography. In January, sea level pressures are relatively high in the GEOS on the eastern side of the Himalayas, with a maximum centered near 50°N 130°E. Lower sea level pressures are positioned over the Himalayas. This high pressure establishes a relative eastward-directed surface pressure gradient across the mountains which may contribute to the positive mountain torque bias on the atmosphere in the GEOS. In July, lower sea level pressures are situated directly over the Himalayan plateau, however, because mountain torque is produced by differences in pressure across a topographic barrier, this low pressure likely contributes much less to the GEOS torque bias. The sea level pressure on the eastern and western sides of the Himalayas are similar in the two analyses, and this lack of overall gradient likely results in the similarity of the torques in the warm season.

To determine the extent to which the differences in sea level pressure are reflected in the upper air data, we show in Fig. 4 the differences in 500 hPa geopotential height between the two analyses. In January, there are higher geopotential heights in the GEOS analyses on the eastern and lower geopotential heights on the western side of the Himalayas, with typical magnitudes of 5 m. Above the maximum difference in sea level pressure (Fig. 3), however, very little height difference is present. In July, lower heights exist in the GEOS analyses over the Himalayan plateau in a region of lower surface pressure (Fig. 3); these features may be a reflection of more diabatic heating of the elevated land mass in the GEOS relative to NCEP. Positive geopotential height differences of about 10 m and 5 m are present on the eastern and western side, respectively, with little reflection in the sea level pressure field (Fig. 3).

2) Synoptic-scale atmospheric signals in Eurasia mountain torque

To determine the sea level pressure patterns associated with synoptic-scale mountain torque fluctuations, we band-passed filtered the Eurasia mountain torque time series from the GEOS and NCEP analyses to retain fluctuations on the 5- to 12-day time scale. We formed one map of composite sea level pressure on days when the mountain torque is 2 standard deviations from the mean and another map for days when the

mountain torque is 2 standard deviations below the mean, as we did for testing global series in Iskenderian and Salstein (1998; IS). The difference map, which yields patterns associated with positive synoptic-scale mountain torque fluctuations, is shown in Fig. 5. Over Asia, the sea level pressure pattern that leads to large band-passed values in Eurasia mountain torque features relatively low sea level pressure to the north of the Himalayas, and relatively high sea level pressure to the east of the mountains. The magnitude of these pressure features is about 12 and 10 hPa, respectively. These pressure features are part of a wave train that extend from Europe to the Pacific Ocean. This configuration of sea level pressure across the Himalayas, which has a positive eastward gradient, helps to produce a positive mountain torque over Eurasia. This result is stronger than that of IS, though the anomalies are in similar locations over Eurasia. Similar pressure patterns, both in magnitude and location, exist in the NCEP analysis. We will examine the evolution and dynamics of angular momentum transfer in the vicinity of the Himalayas for the strongest oscillations.

Iskenderian, H., and D.A. Salstein, 1998: Regional sources of mountain torque variability and high-frequency fluctuations in atmospheric angular momentum. *Mon. Wea. Rev.*, **126**, 1681-1694.

Eurasia Mountain Torque

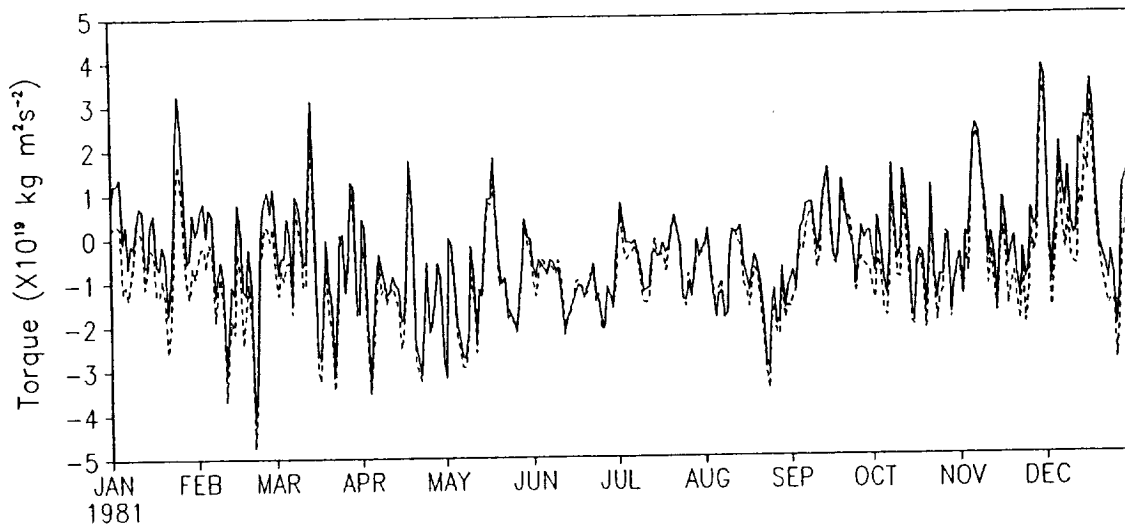


Fig. 1. Daily time series of Eurasia mountain torque for 1981 from the GEOS (solid) and NCEP (dashed) analyses.

Monthly Mean Eurasia Mountain Torque GEOS - NCEP

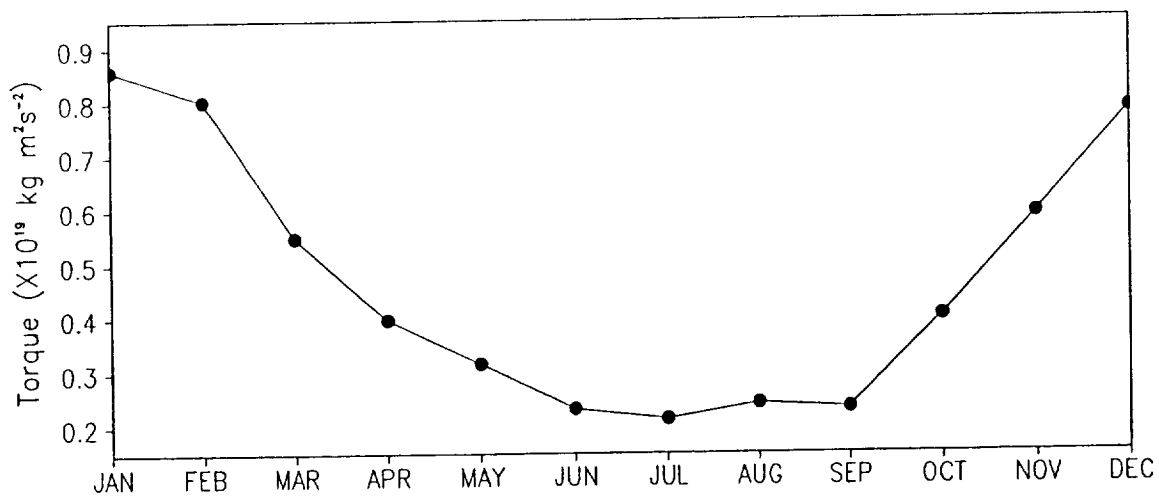
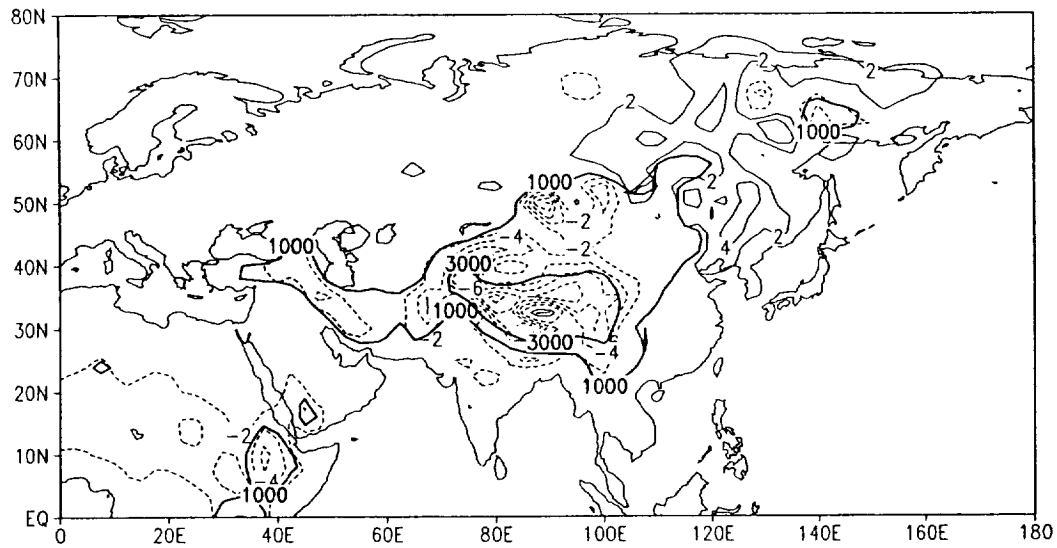


Fig. 2 Differences (GEOS - NCEP) in monthly-mean Eurasia mountain torque. Units are $10^{19} \text{ kg m}^2 \text{ s}^{-2}$.

January Sea Level Pressure (hPa)
GEOS - NCEP



July Sea Level Pressure (hPa)
GEOS - NCEP

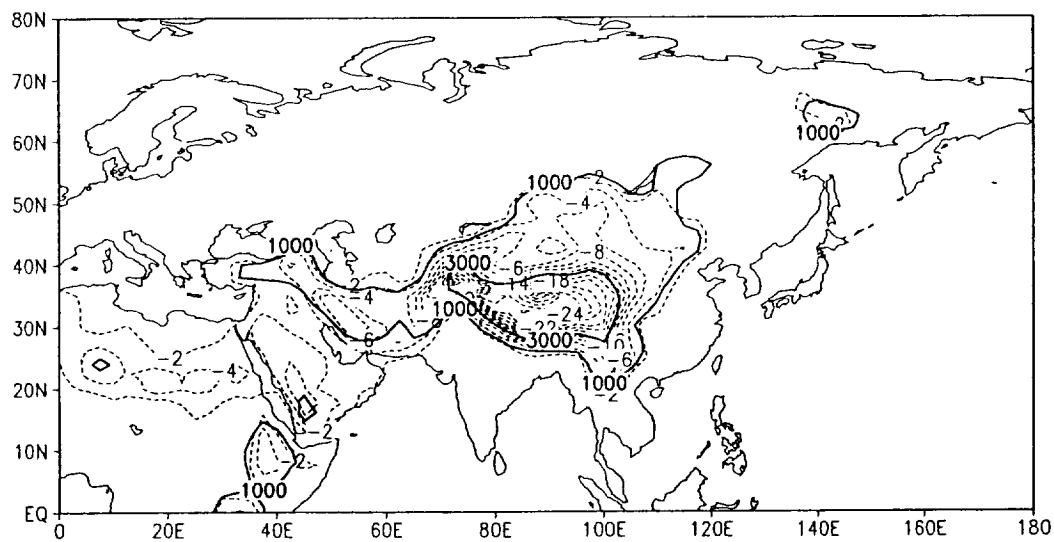
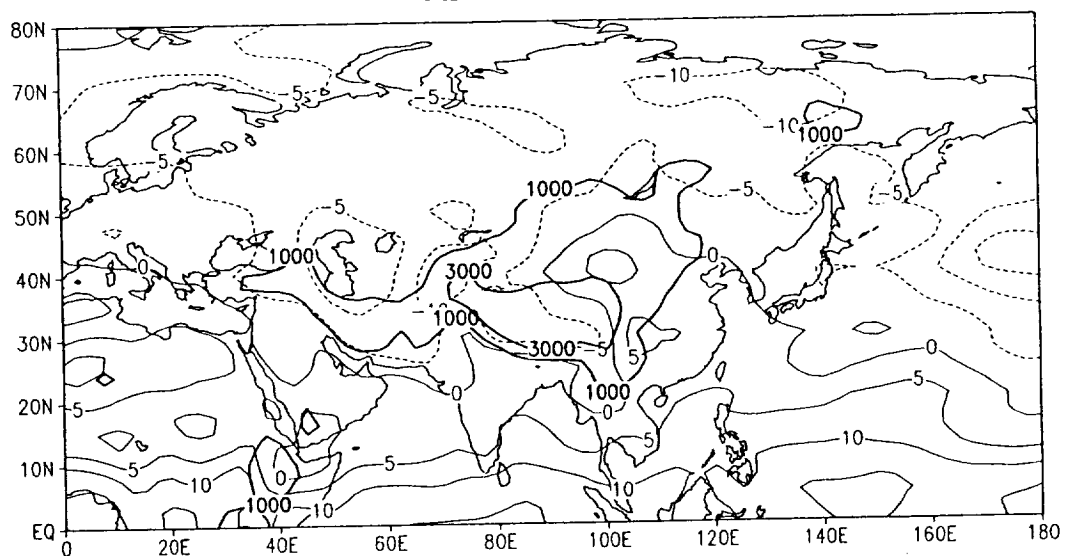


Fig. 3 Differences (GEOS - NCEP) in January and July mean sea level pressure contoured every 2 hPa. Positive values are solid and negative values are dashed. The bold solid line depicts the 1000 m and 3000 m elevation in the GEOS analysis.

January 500 hPa Height (m)
GEOS - NCEP



July 500 hPa Height (m)
GEOS - NCEP

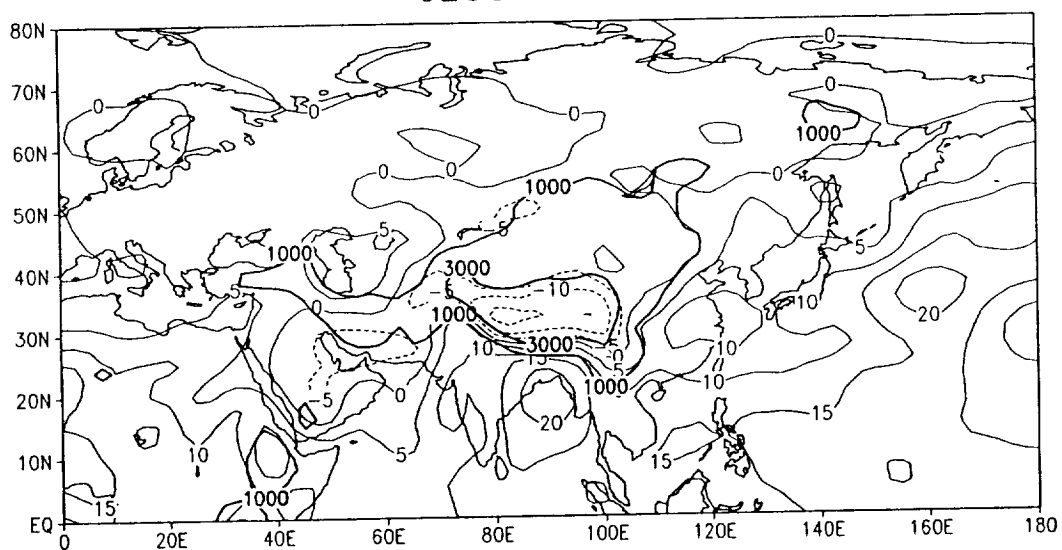


Fig. 4. Same as Fig. 3, except for 500 hPa geopotential height (m).

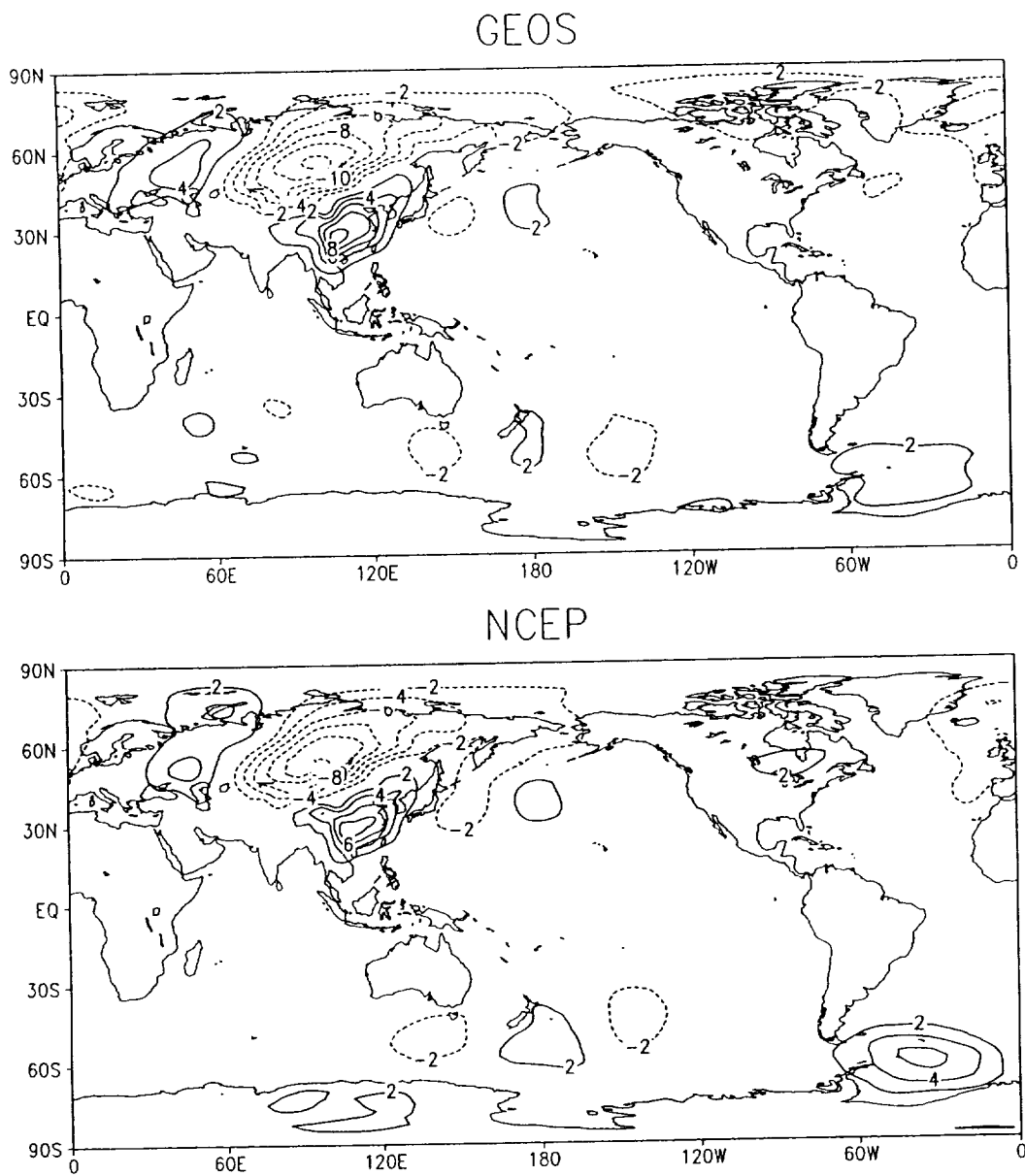


Fig. 5 The difference in sea level pressure (contoured every 2 hPa) for days when the Eurasia band-passed mountain torque is greater than or equal to 2 standard deviations and days when the Eurasia band-passed mountain torque is less than or equal to 2 standard deviations from the mean. Positive values are solid and negative values are dashed.

2. AMIP-2 Angular Momentum study

Study of the how models participating in the second Atmospheric Model Intercomparison Project (AMIP-2) have success in simulating the angular momentum of the atmosphere. To date, only 2 models have submitted results for this assessment, but recent indications from the management of the AMIP project indicate that the release of results from other models is imminent. Results are given in the attached set of figures from a presentation given at the International Union of Geodesy and Geophysics symposium at Birmingham, UK.

Further results are given in the extended abstract, entitled, "Assessment of atmospheric angular momentum parameters in AMIP-2 simulations, by David A. Salstein, AER, Lexington, MA; and R. D. Rosen, J. O. Dickey, and S.L. Marcus," also given below.

Two figures include diagrams describing the results of Seasonal and Interannual statistics in a so-called Taylor diagram. The radial distance in these diagrams indicate the variance in the signals, while the distance along the azimuth indicates the correlation coefficient with a verification field, the NCEP-NCAR reanalyses. Distances from the filled in circle indicate root mean square errors from the NCEP-NCAR reanalyses. The various AMIP models are given by their abbreviations, while the GLA model is given as a filled-in triangle. Seasonal statistics indicate that the GLA model is among the better compared to the group of models, while the interannual statistics indicate that the GLA is within the range of the other models.

Assessing atmospheric general circulation models using angular momentum diagnostics

David A. Salstein and Richard D. Rosen
Atmospheric and Environmental Research, Inc.
Cambridge, Massachusetts, USA

Jean O. Dickey and Steven L. Marcus
Jet Propulsion Laboratory
Pasadena, California, USA

International Union of Geodesy and Geophysics
1999 Meeting
Birmingham, United Kingdom

July 20, 1999



Outline

Atmospheric angular momentum (AAM) is an excellent index of climate fluctuations on seasonal to interannual time scales.

Relative AAM is calculated from zonal winds, weighted more strongly at lower latitudes.

Angular momentum is a conservative quantity within the Earth system: changes in AAM are directly related to those in length of day.

AMIP-1 (10 years) provided the opportunity to verify how 23 models produced AAM, globally and regionally:

Hide, R., J.O. Dickey, S.L. Marcus, R.D. Rosen, and D.A. Salstein, 1997 J. Geophys. Res., 102, 16423-16438.

AMIP-2 (17 years): Japan Meteorological Agency (JMA) and the United Kingdom Meteorological Office (UKMO) models are now available.

Comparisons between AMIP-2 and AMIP-1 results.

Torques effecting changes in AAM will be compared:

“Friction torque” from axial wind stresses

“Mountain torque” from surface pressure distribution around topography

Selected differences between AMIP-1 and AMIP-2 versions of models

JMA:

T63 vs T42 spectral model; 30 levels vs 21 levels

Arakawa-Schubert scheme simulates penetrative convection, re-evaporation of rainwater

Includes downdraft scheme

UKMO

Method of filling “negative” moisture has been changed, done on a local, rather than global, basis.

Diffusion: switched off near steep topography

Horizontal diffusion for winds, potential temperature, moisture, 6th order

Enhanced gravity wave-drag scheme

Cloud treatment

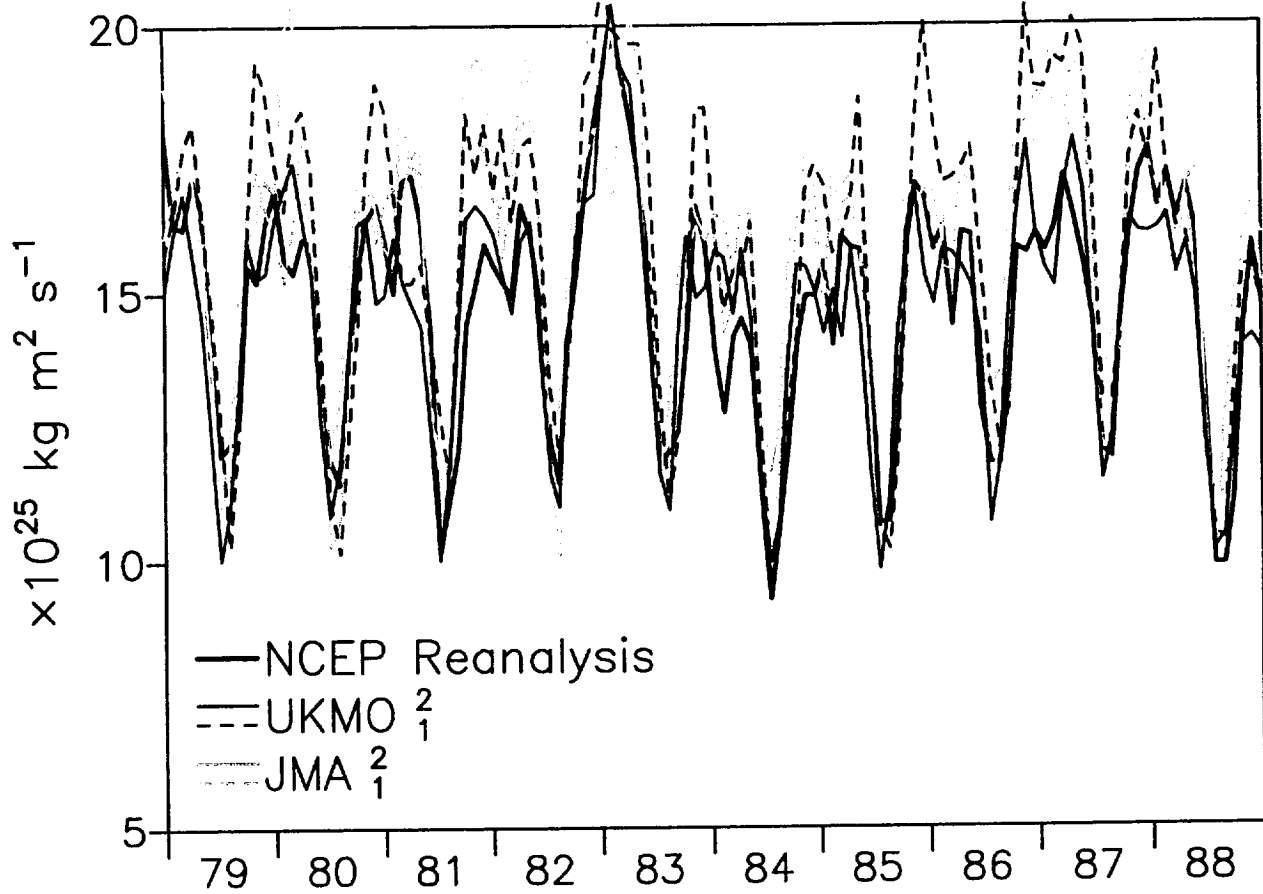
Convective momentum transport added

Liquid/ice decision more sophisticated

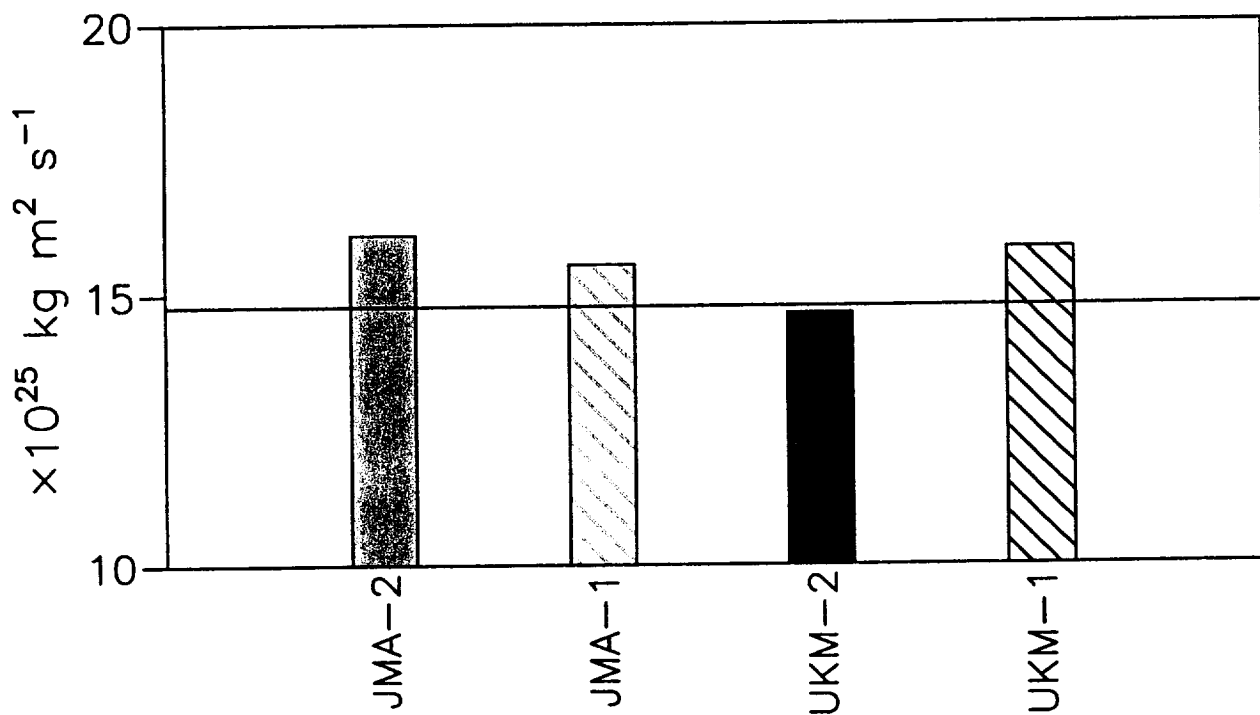
Moisture fluxes from land surface from evaporation, transpiration

$M^w(10)$, 1979–1988

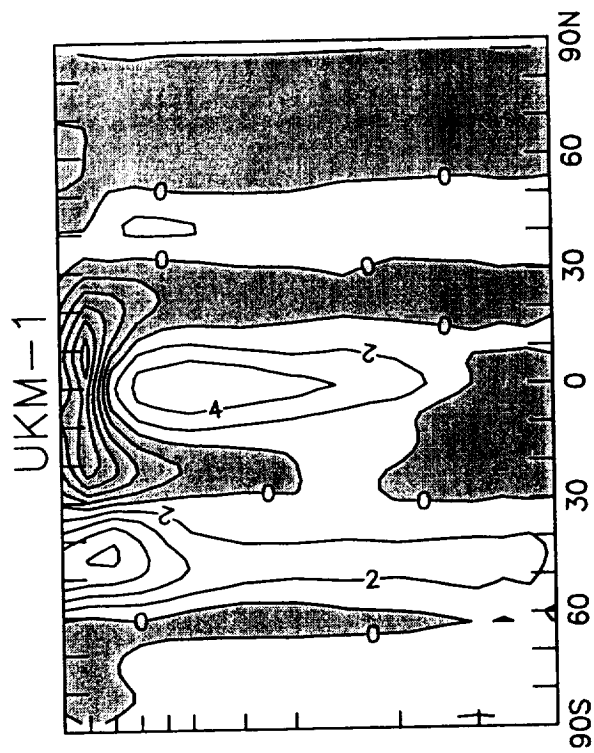
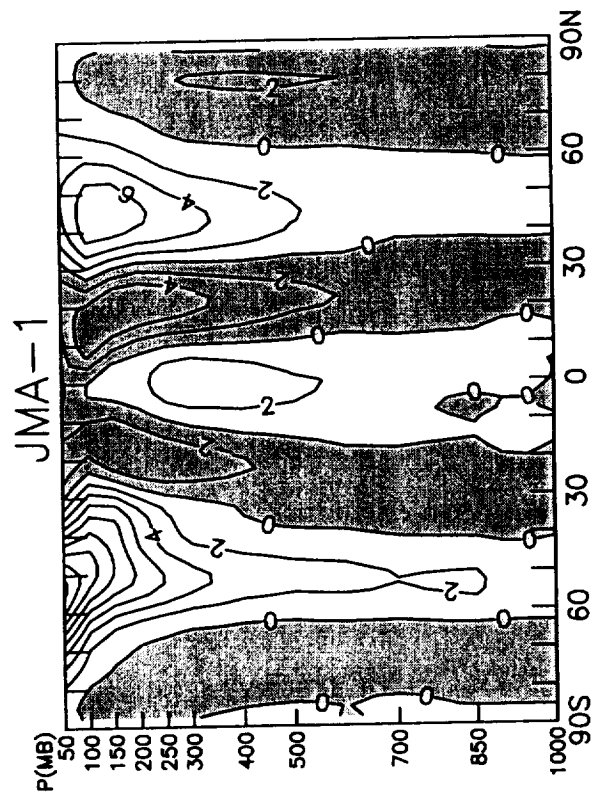
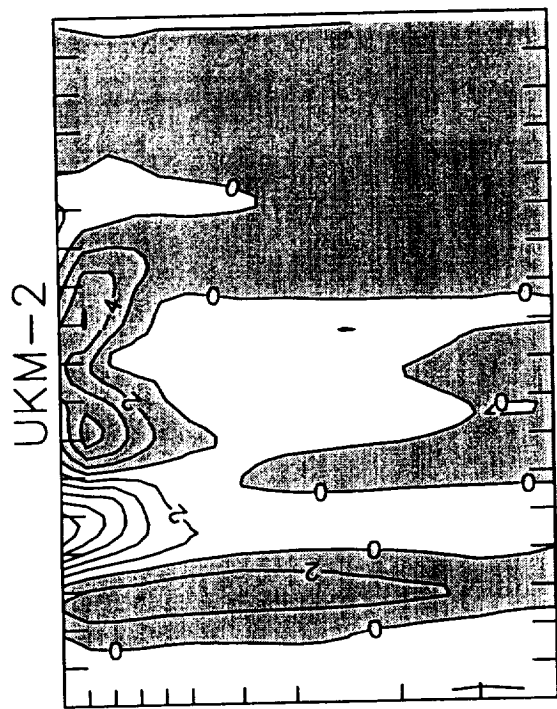
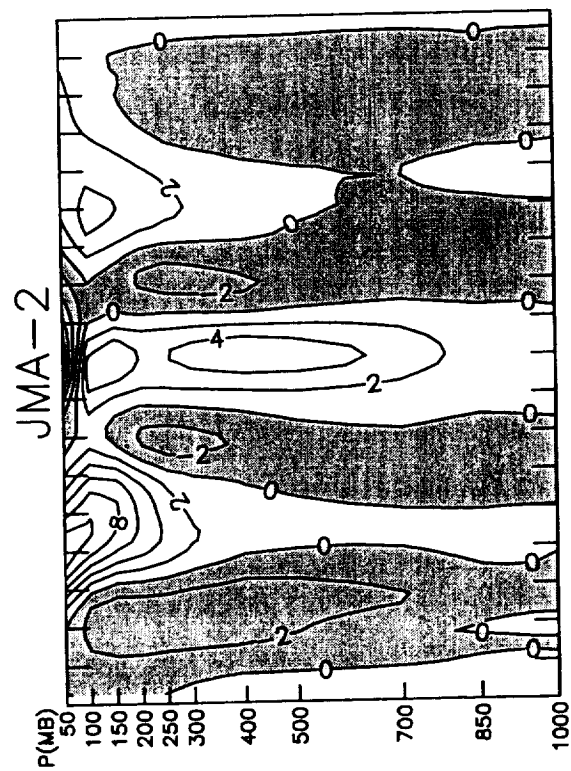
AMIP-2 vs. AMIP-1



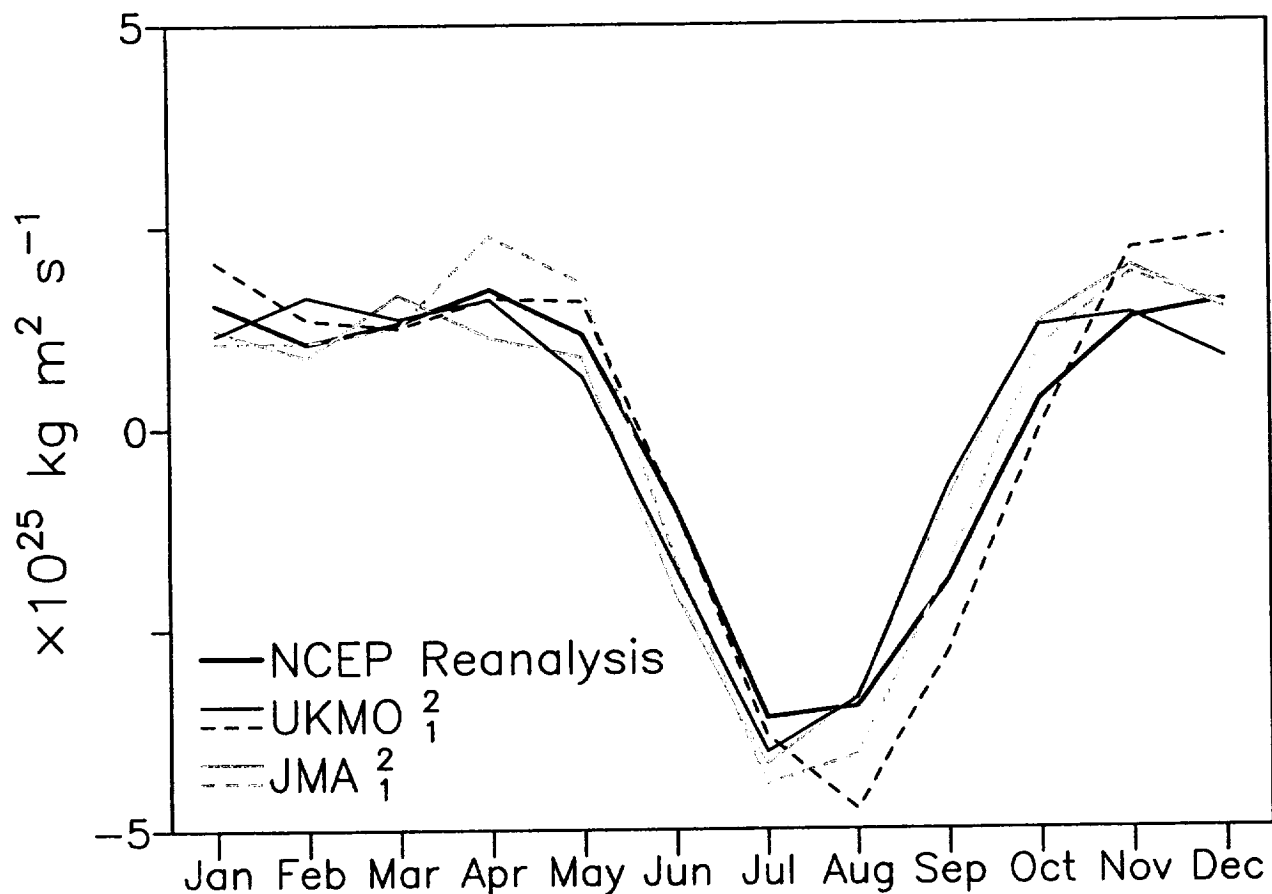
Mean



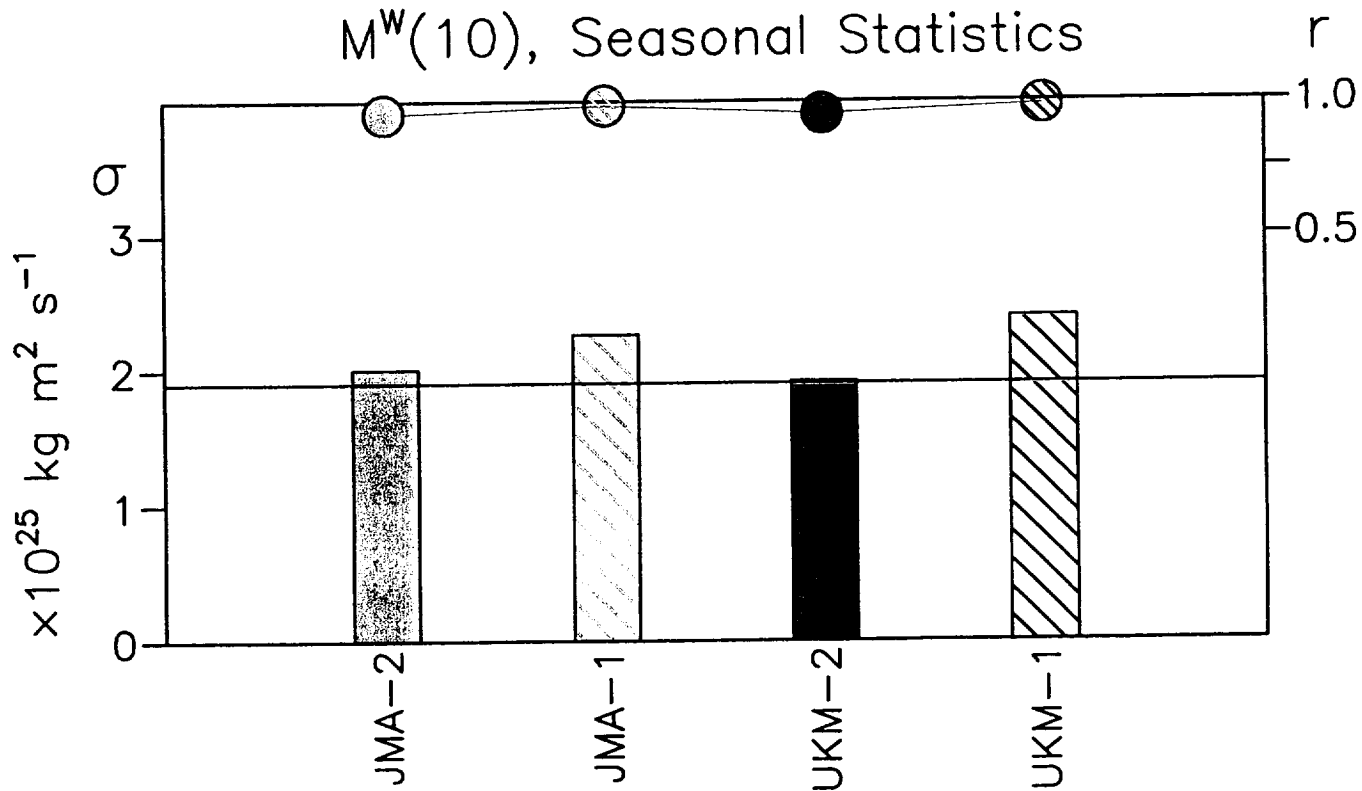
AMIP [u], 1979-1988 Bias (m s^{-1})



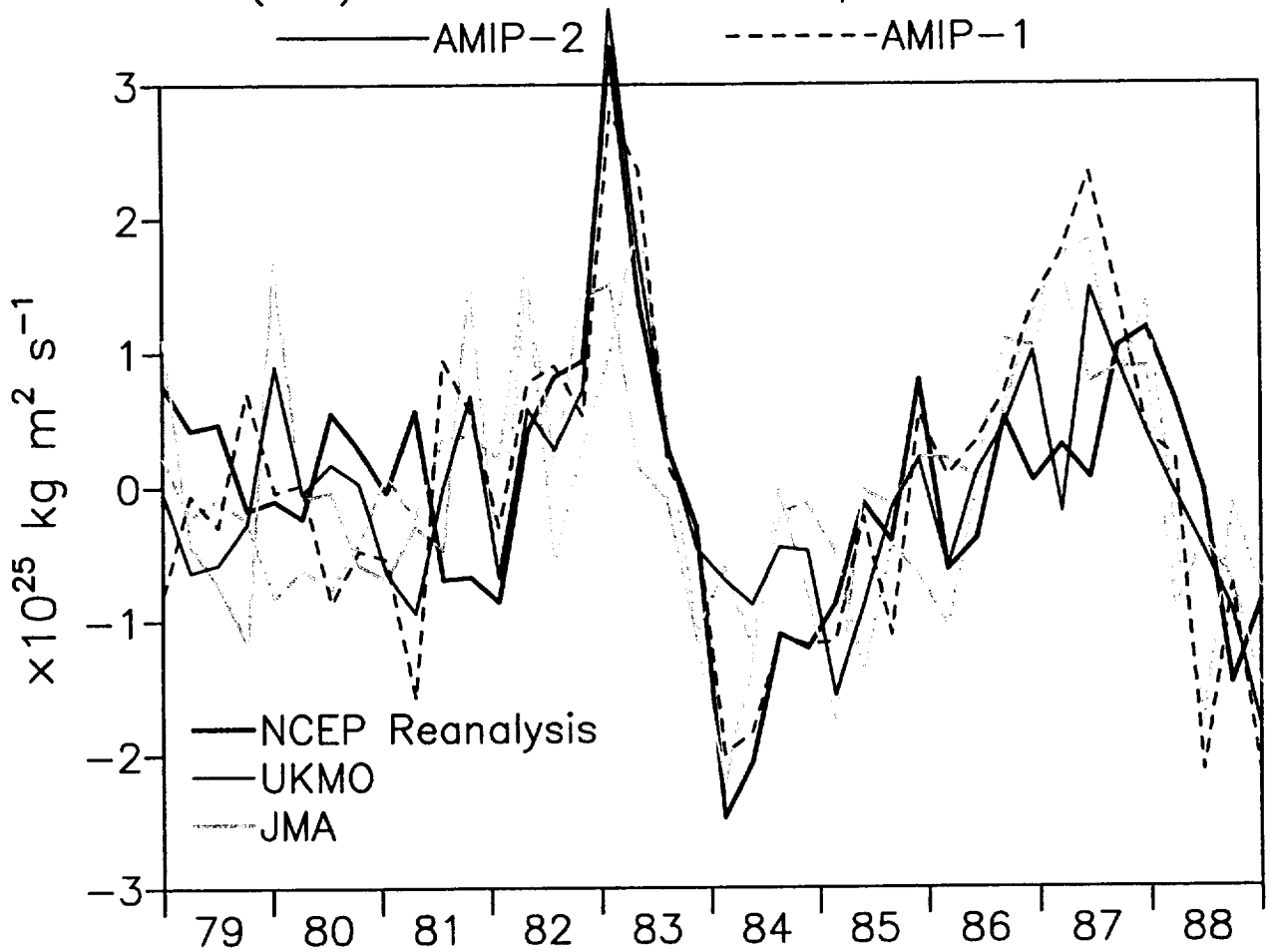
$M^W(10)$ Seasonal Cycle, 1979–1988 AMIP–2 vs. AMIP–1



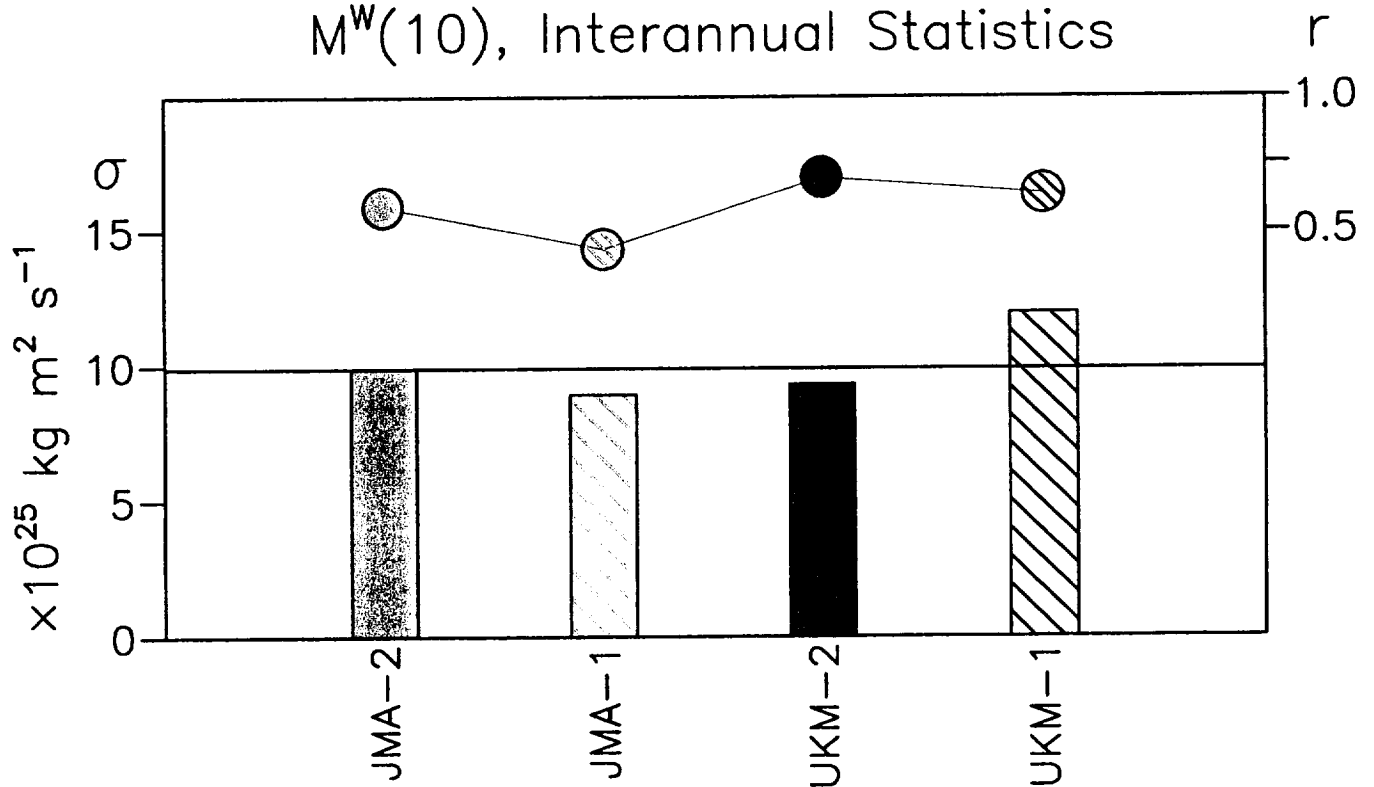
$M^W(10)$, Seasonal Statistics



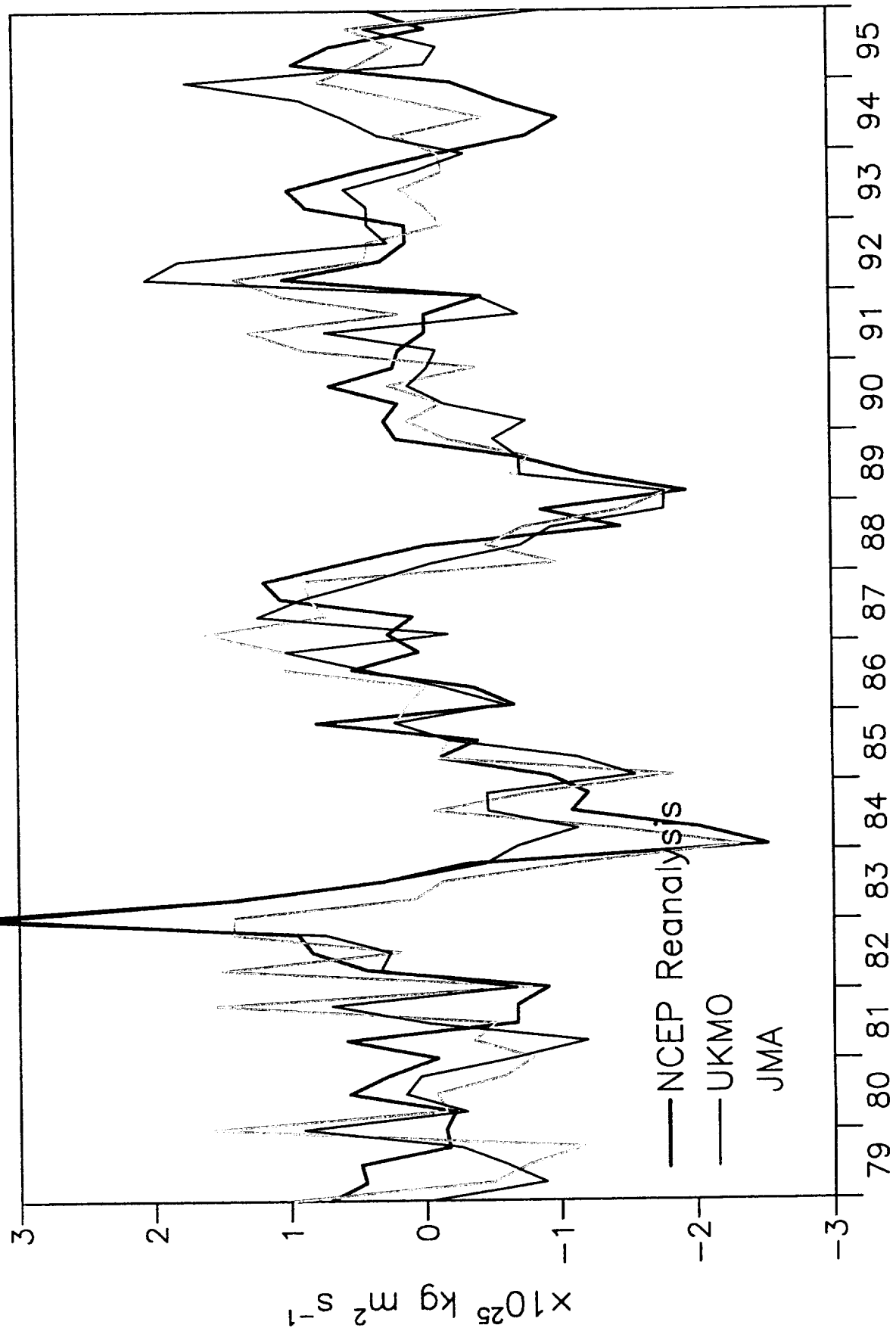
AMIP $M^W(10)$ Interannual Component, 1979–1988



$M^W(10)$, Interannual Statistics



AMIP-2 $M^w(10)$ Interannual Component, 1979-1995

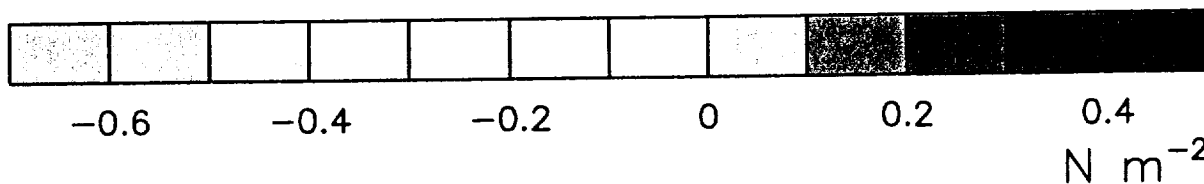
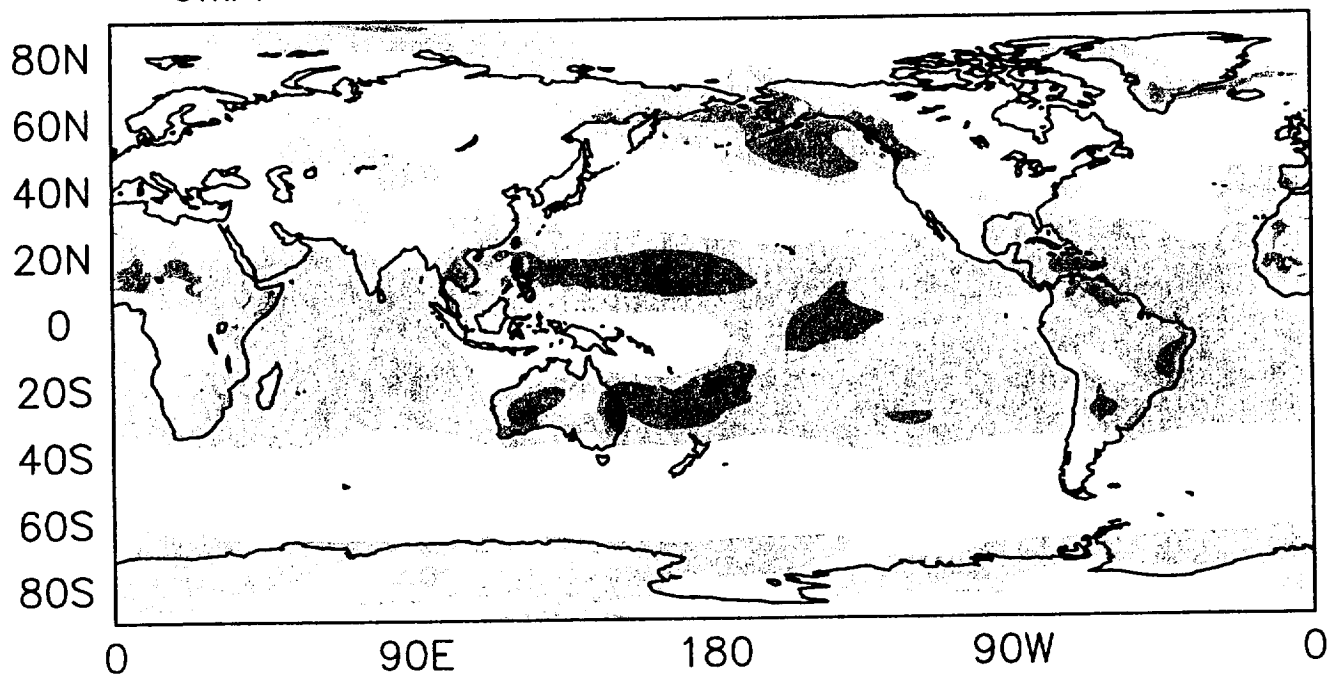


AMIP-2 Zonal Surface Stress, Jan. 1979

UKMO



JMA



CONCLUSIONS

1. *UKMO model improved noticeably in the mean by reduction of biases in near-equatorial upper troposphere*
2. *Both JMA and UKMO models showed notable improvement in amplitude of both seasonal and interannual signals*
3. *Significant correlation occurs between models and reanalysis for 17-year period, involving several ENSO peaks*
4. *AMIP-2 offers the opportunity to diagnose the reasons for improved results, by close interactions with modeling groups*

ASSESSMENT OF ATMOSPHERIC ANGULAR MOMENTUM IN AMIP-2 SIMULATIONS

David A. Salstein and Richard D. Rosen
Atmospheric and Environmental Research, Inc., Lexington, Massachusetts

Jean O. Dickey and Steven L. Marcus
Jet Propulsion Laboratory, California Institute of Technology, Pasadena, California

1. INTRODUCTION

As part of a diagnostic subproject of the second phase of the Atmospheric Model Intercomparison Project (Gates et al. 1999), we are evaluating how well the current generation of general circulation models simulates relative atmospheric angular momentum (AAM), a fundamental measure of the atmosphere's circulation that depends on the strength and distribution of the zonal winds. We focus on the spread in the mean, seasonal, and interannual components of AAM among the currently available models and use the NCEP-NCAR reanalysis for the AMIP-2 period of 1979-95 as our primary verification data set. We also compare AAM from the AMIP-2 models with that from their AMIP-1 predecessors (Hide et al. 1997) to comment upon model evolution (Sperber et al. 1999).

2. MEAN, SEASONAL, AND INTERANNUAL SIGNALS

We calculate AAM between pressure levels 1000 and 10 hPa using the zonal wind fields archived for the 16 AMIP-2 models currently available.

The ensemble median value of AAM for the 17-year period is some 17% above that of the NCEP-NCAR reanalysis (Fig. 1), and the spread, as measured by the ensemble's interquartile range, is 12% of the median value. Eight of the model values are higher than their counterparts in AMIP-1 (for the overlapping period of 1979-1988), and four are lower. Upon analyzing the zonal winds that contribute to the model bias, we find that the four highest AAM values, for example, exhibit zonal wind biases with several features in common (Fig. 2). Among these are a positive bias in the upper regions of the extratropics of both hemispheres as well as much of the tropics, and a negative bias in the subtropics.

The variability in AAM produced by the available AMIP-2 models is generally realistic. The median of the 16 models' 17-year seasonal signature closely resembles that of NCEP-NCAR (Fig. 3), though failing to achieve the amplitude of the observed seasonal cycle. The shortcoming of the AMIP-1

models noted by Hide et al. (1997) in underestimating the seasonal component of AAM during northern winter continues to exist in AMIP-2.

The interannual anomaly series (Fig. 4) shows a strong relationship with the phase of the El Niño/Southern Oscillation. AAM is greater than normal during the El Niño events of the period: 1983 (strong), 1987 (weak), and early 1990s (weak, but prolonged). The observed AAM anomalies are somewhat better matched by the AMIP-2 median than by that of AMIP-1 in the years the experiments overlap. Note that although the 1988-89 La Niña minimum in AAM is well simulated by both AMIP experiments, the very low minimum observed during the 1984 cold event is not fully reproduced in either.

3. CONCLUDING REMARKS

As in AMIP-1, the variability in AAM is reasonably well simulated by AMIP-2 models. The difference among the model results remains quite large, however, especially in the case of the climatological mean. Here, and in the case of the amplitude of the seasonal cycle, AMIP-2 results are thus far not an improvement. In individual cases, the updates to certain models have provided improvements. For example, biases were reduced in the UKMO model, particularly in the tropical upper troposphere when changes were made involving treatment of low moisture values, diffusion, enhanced gravity wave-drag, and a cloud scheme with sophisticated convective momentum transport.

Further analyses, including the EOF approach used by Hide et al. (1997), will help identify common sources of error among the AMIP-2 simulations of AAM. This work will await the addition of more model results to the AMIP-2 archive beyond the 16 considered here.

Acknowledgments. Grant ATM-0002688 from NSF and contract NAS5-98179 from NASA to AER supported the work reported here. The work of JOD and SLM was performed at the Jet Propulsion Laboratory, California Institute of Technology, under contract with NASA.

Corresponding author address: David A. Salstein,
Atmospheric and Environmental Research, Inc.,
131 Hartwell Ave., Lexington, MA 02421;
email: salstein@aer.com

4. REFERENCES

- Gates, W. L., et al., 1999: An overview of the results of the Atmospheric Model Intercomparison Project (AMIP I). *Bull. Amer. Meteor. Soc.*, 80, 29-55.
- Hide, R., J. O. Dickey, S. L. Marcus, R. D. Rosen, and D. A. Salstein, 1997: Atmospheric angular momentum fluctuations during 1979-1988

simulated by global circulation models. *J. Geophys. Res.*, 102, 6423-16438.

- Sperber, K. R. and participating AMIP modeling groups, 1999: Are revised models better models? A skill score assessment of regional interannual variability. *Geophys. Res. Lett.*, 26, 1267-1270.

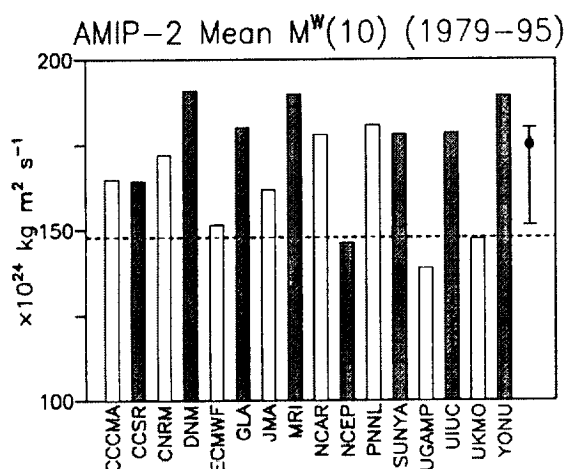


Fig. 1. Mean value of 16 model runs for 1979-1995 of relative angular momentum to 10 hPa. The dashed line shows the value based on NCEP-NCAR reanalyses. On the right, the dot indicates the median model value and the length of the bar indicates the interquartile range. Models are more fully identified within Gates et al. (1999).

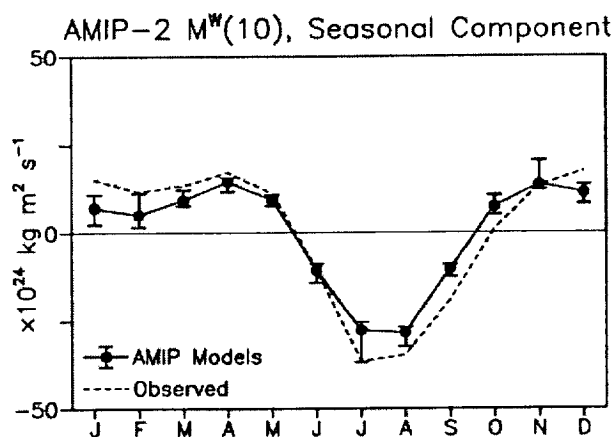


Fig. 3. Seasonal cycle of the 17-year series of AAM determined from monthly means averaged over the period. Solid line connects the model median, with vertical bars the interquartile range. Broken line is from the NCEP-NCAR reanalyses.

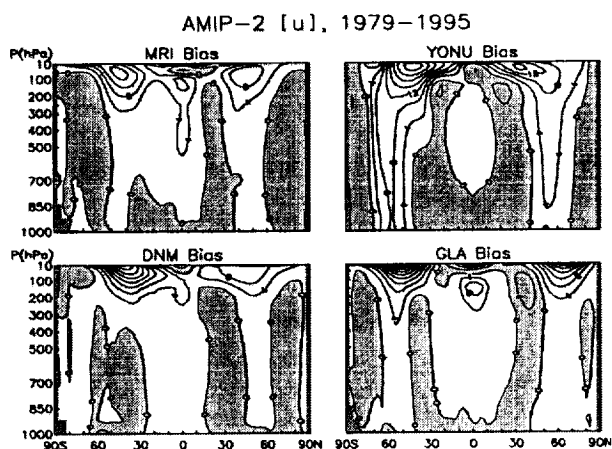


Fig. 2. Zonal mean zonal wind biases of four models with high AAM values, obtained by subtracting the NCEP-NCAR reanalysis from the original model fields.

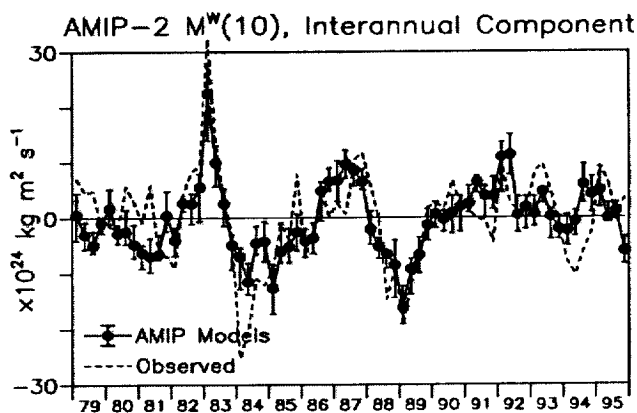
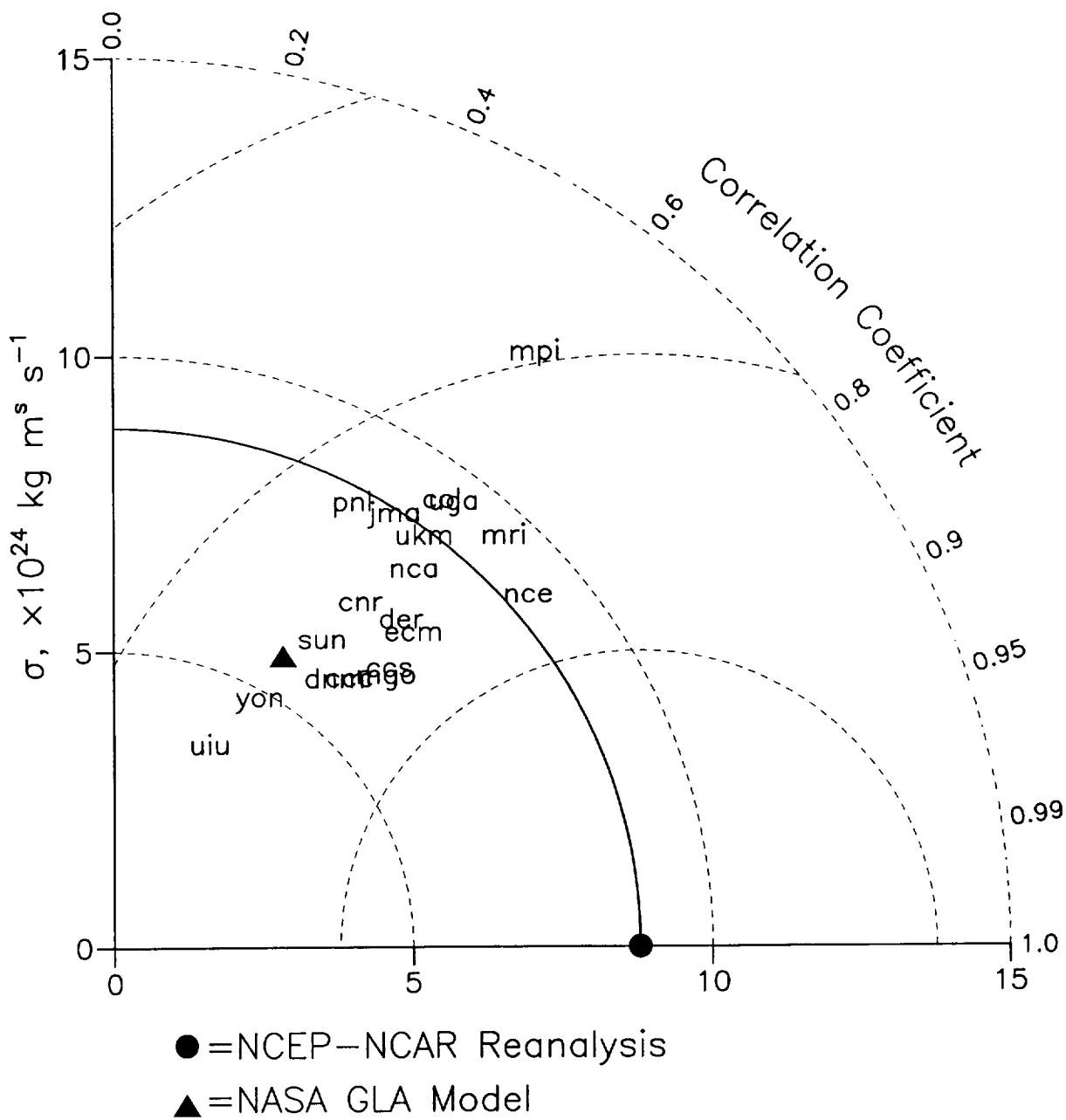
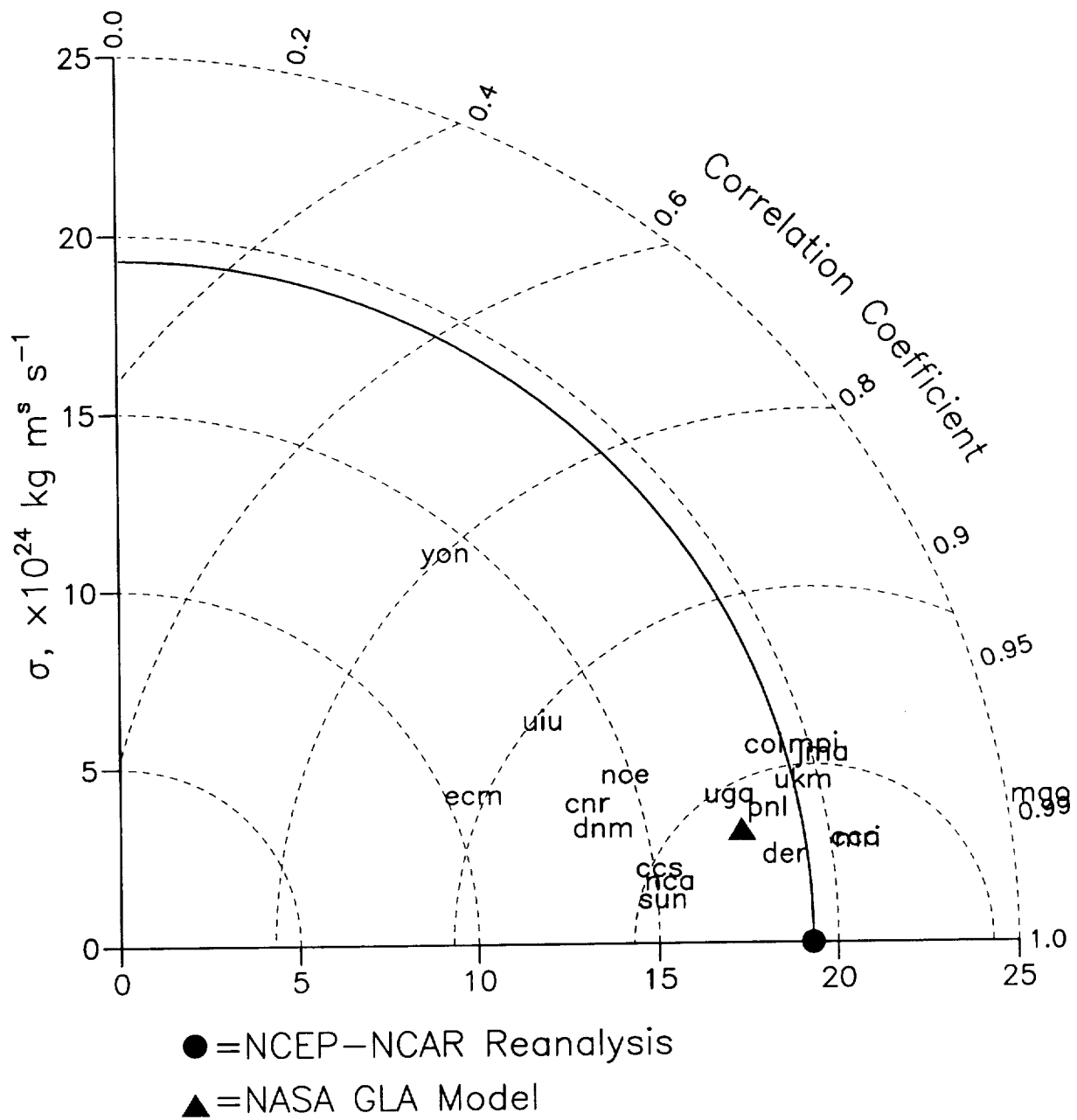


Fig. 4. Same as Fig. 3, but for interannual anomalies for all seasons in the 17-year period.

AMIP-2 M(50) Interannual Statistics



AMIP-2 M(50) Seasonal Statistics



3. Energetics and momentum from the GEOS -2 McRAS run.

We have been investigating global diagnostics of the atmosphere based on different model and data assimilation systems. Here we have taken a recent run of the NASA Goddard Earth Observing System -2 model using the prognostic McRAS scheme (Microphysics of Clouds with Relaxed Arakawa-Schubert Scheme) and the Simple SiB package. Sud and Walker (1999) have shown that the scheme improves the cloud-radiative forcing and effect the climatology of the model atmosphere so produced, especially in the region of the Intertropical Convergence Zone. We take a recent run of the GEOS-2 model including the McRAS scheme to assess the impacts on the larger scale heating rates, as well as the implications for the global energy budgets of the atmosphere. We have started calculations of the fields needed to calculate energetics and momentum information. We chose 1987 to look at the seasonal cycle of some quantities. We also focus on January 1987 as a sample month.

First we note the basic parameters, zonal wind, u (in units of m s^{-1}), meridional wind, v (m s^{-1}), temperature, T (K) and specific humidity, q (gm kg^{-1}), between the 1000 and 30 hPa levels. All appear quite realistic. Calculation of eddy terms include those based on transient eddies (indicated by the prime (') notation, and the standing eddies, indicated by the asterisk (*) notation. The fields $[u'v']$, $[u^*v^*]$, proportional to the meridional transports of momentum, and $[v'T']$ and $[v^*T^*]$, proportional to that of heat, are related to conversions between forms of kinetic energy (u, v terms) and potential energy (vT terms) are given as a sample. Here the brackets indicate zonal mean.

Hemispheric mean potential energy P and kinetic energy K terms (both 10^5 J m^{-2}) for each month are given, as are the conversions (Wm^{-2}) noted above (Peixoto and Oort 1992). The values of the energy terms are consistent with earlier analyses of other models and data assimilation systems, although the zonal mean potential and kinetic energy values in the southern hemisphere are somewhat higher.

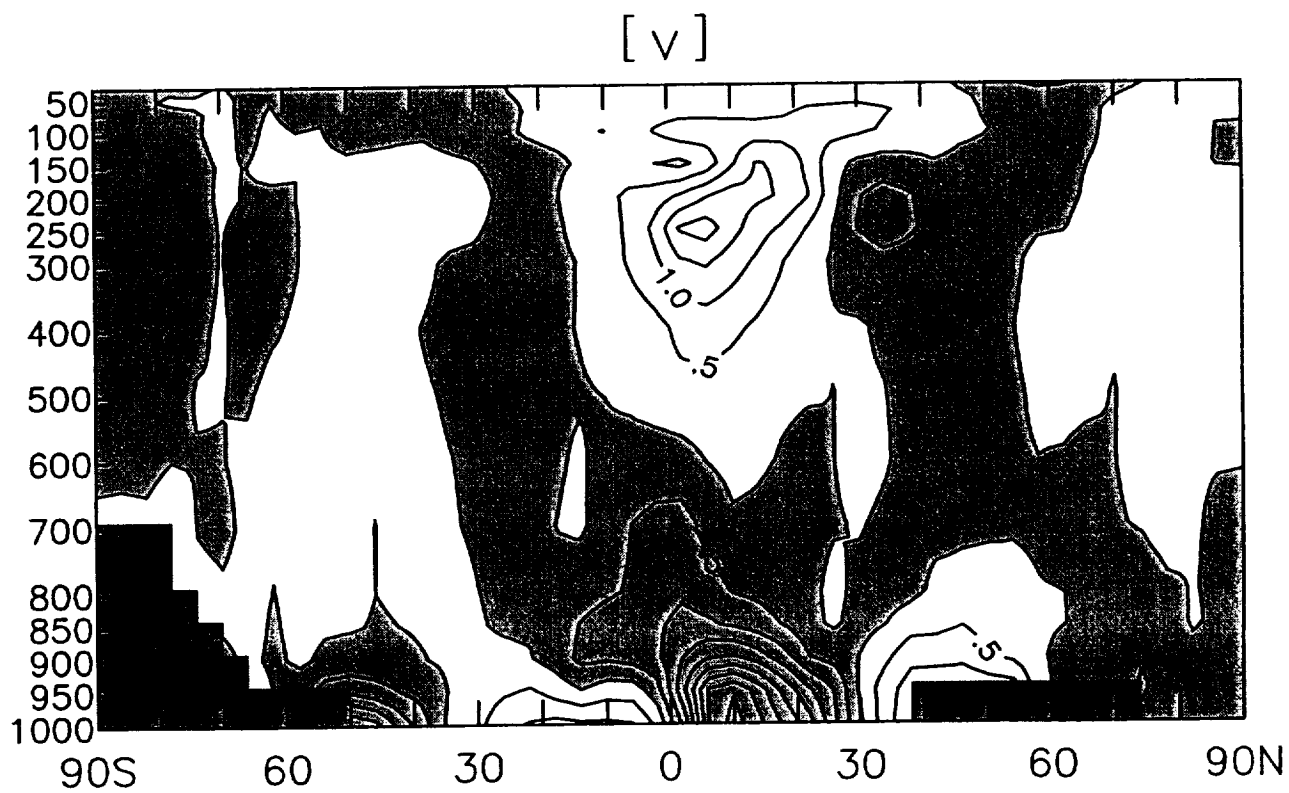
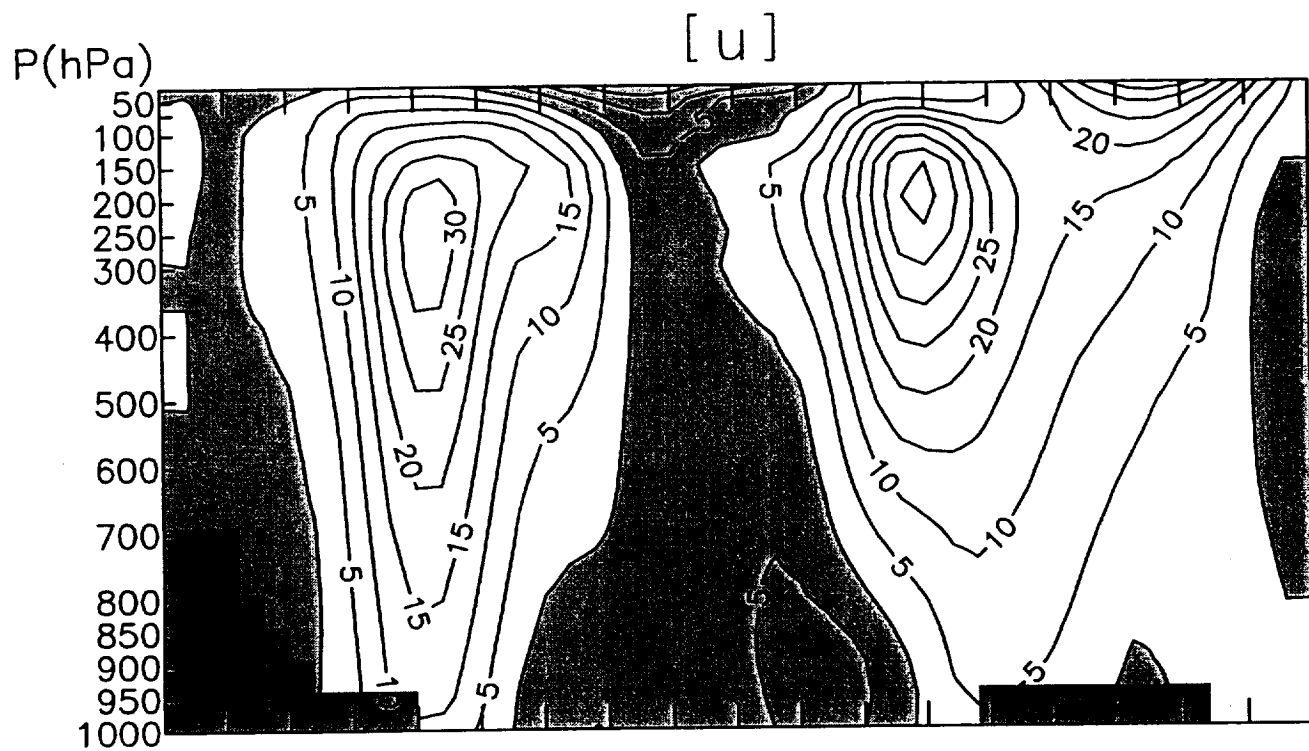
We also show cross sections of the four diabatic heating rates, namely, latent, sensible, shortwave radiational and longwave radiational heating for the sample month of January (units: K day^{-1}). From these two are computed the generation of available potential energy by the individual terms, which we show as a time series for the months of the year 1987. As in most earlier analyses, the influence of the latent heating dominates the sign of the generation of available potential energy. We have calculated the individual heating maps are also given for 850 hPa and 500 hPa levels for January and July over Asia and vicinity. Here we seek to understand how heating over the Eurasian land mass will influence the dynamics of the circulation, leading in part to the interactions reviewed in part 1. We will draw conclusions based on these figures in a paper to be prepared later.

References

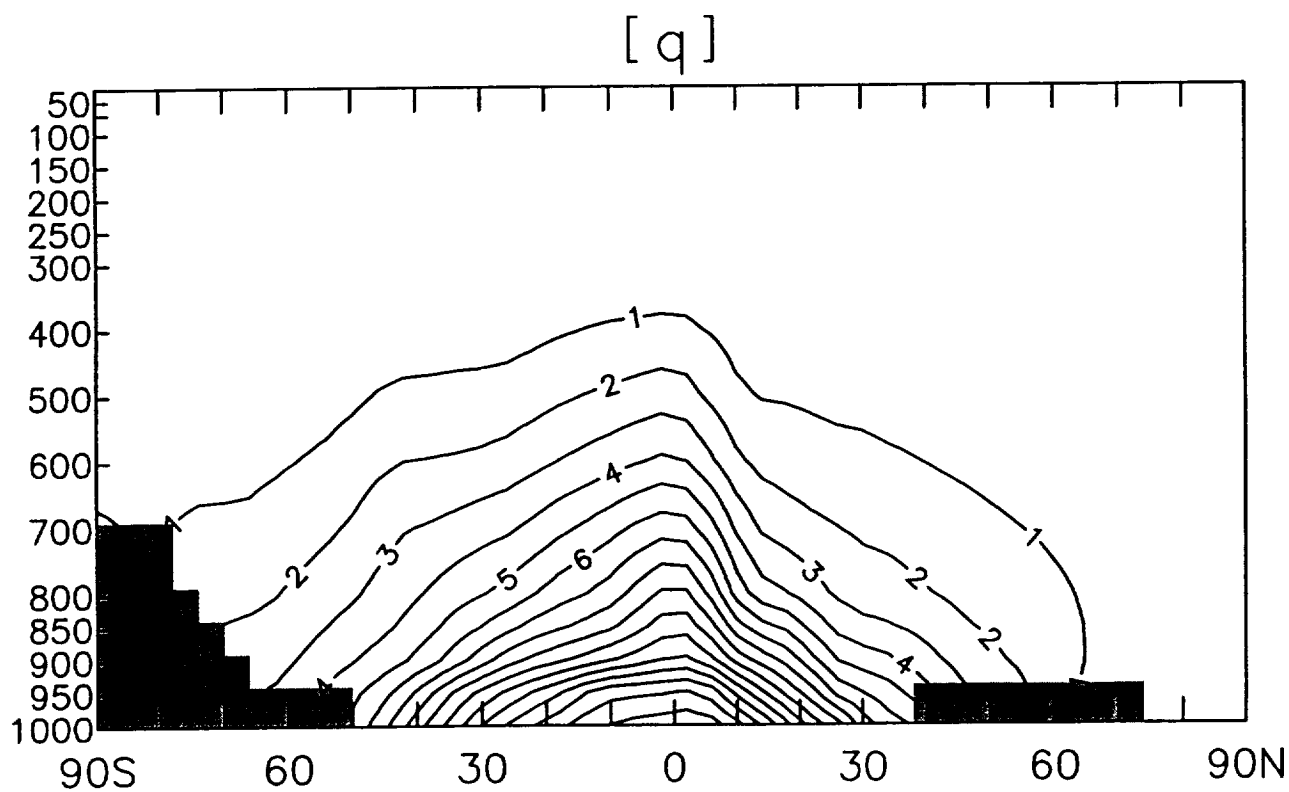
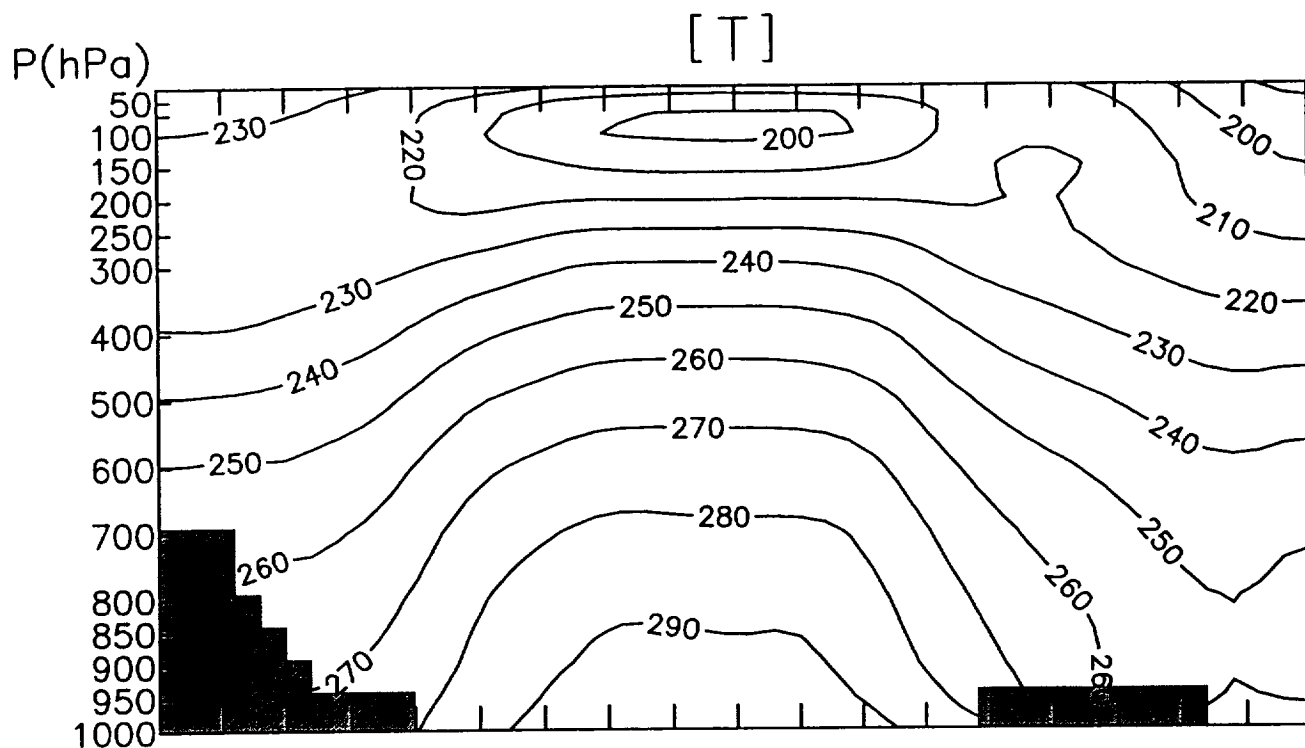
Peixoto, J. P. and A. H. Oort, 1992: *Physics of Climate*, AIP Press, New York.

Sud, Y. C., G. K. Walker, 1999: Microphysics of Clouds with the Relaxed Arakawa-Schubert Scheme (McRAS). Part II: Implementation and Performance in GEOS II GCM. *Journal of the Atmospheric Sciences*: Vol. 56, No. 18, pp. 3221-3240.

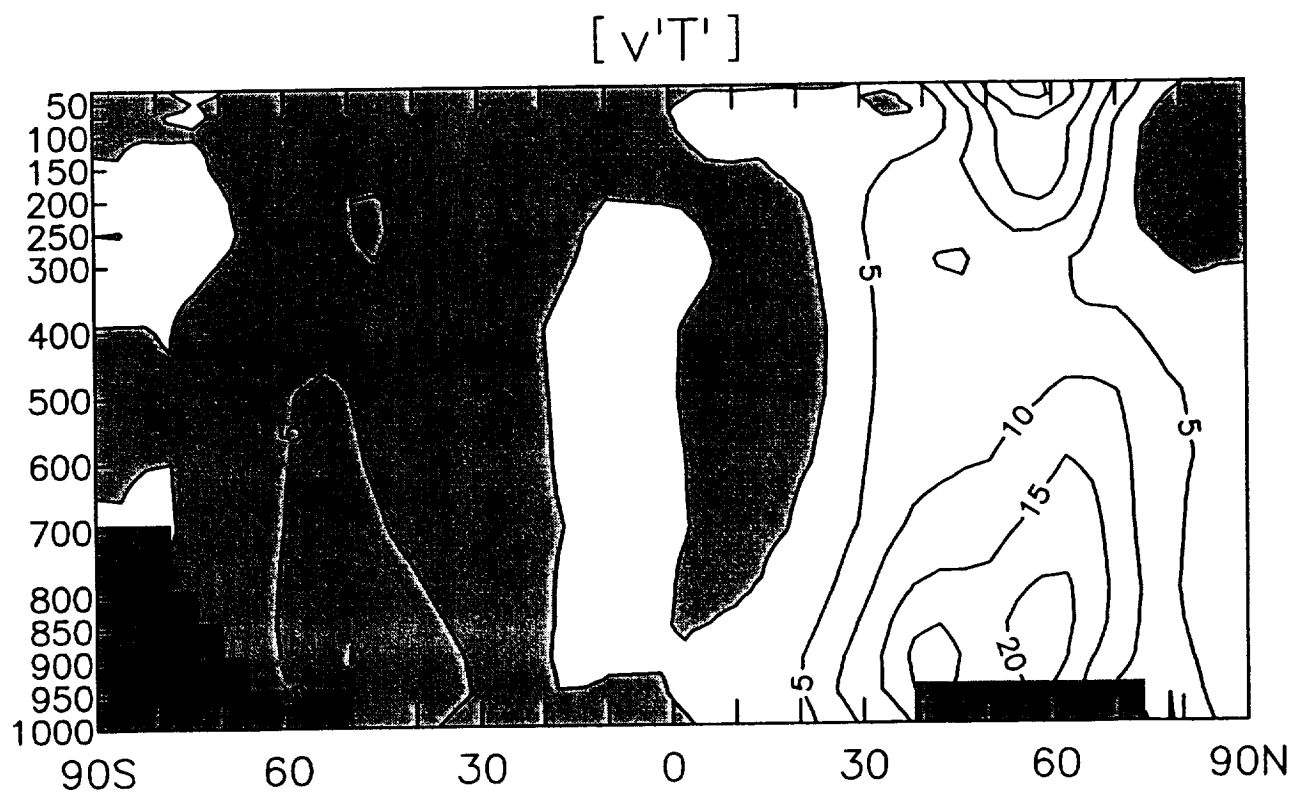
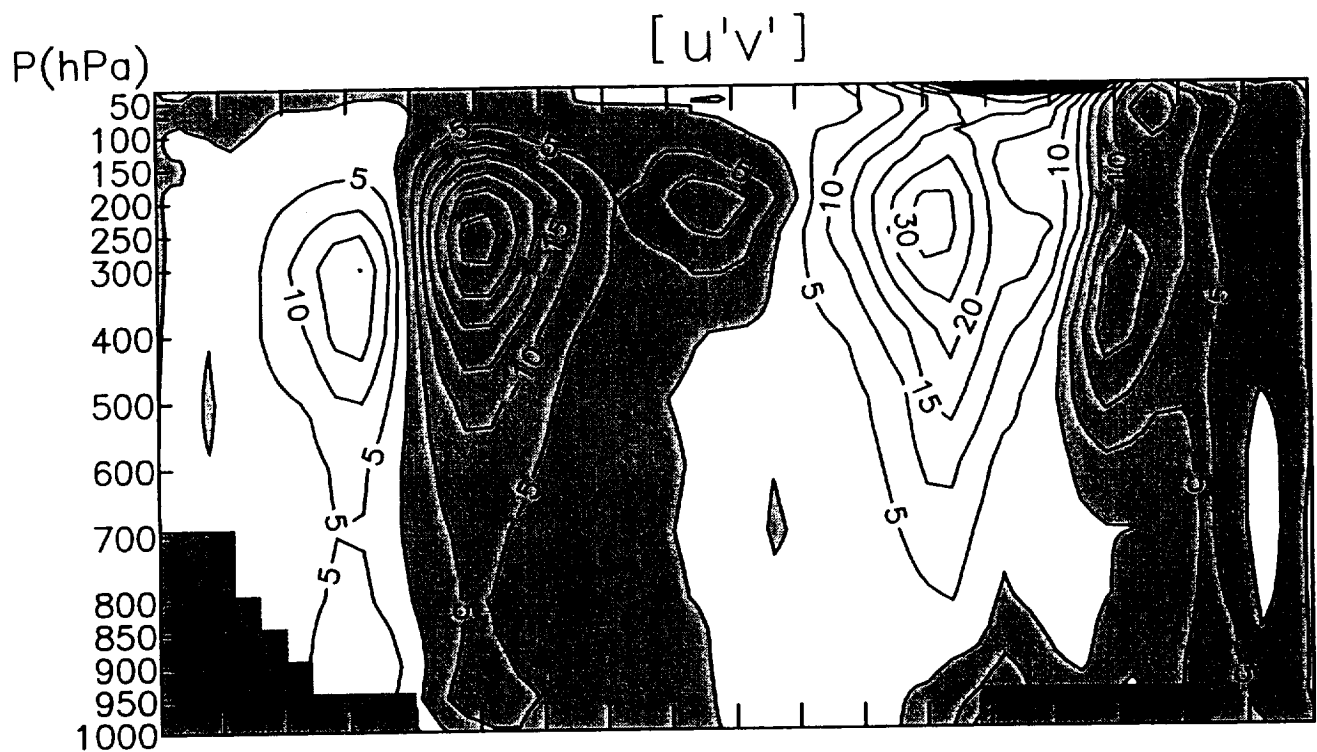
GEOS-2 McRAS, January, 1987



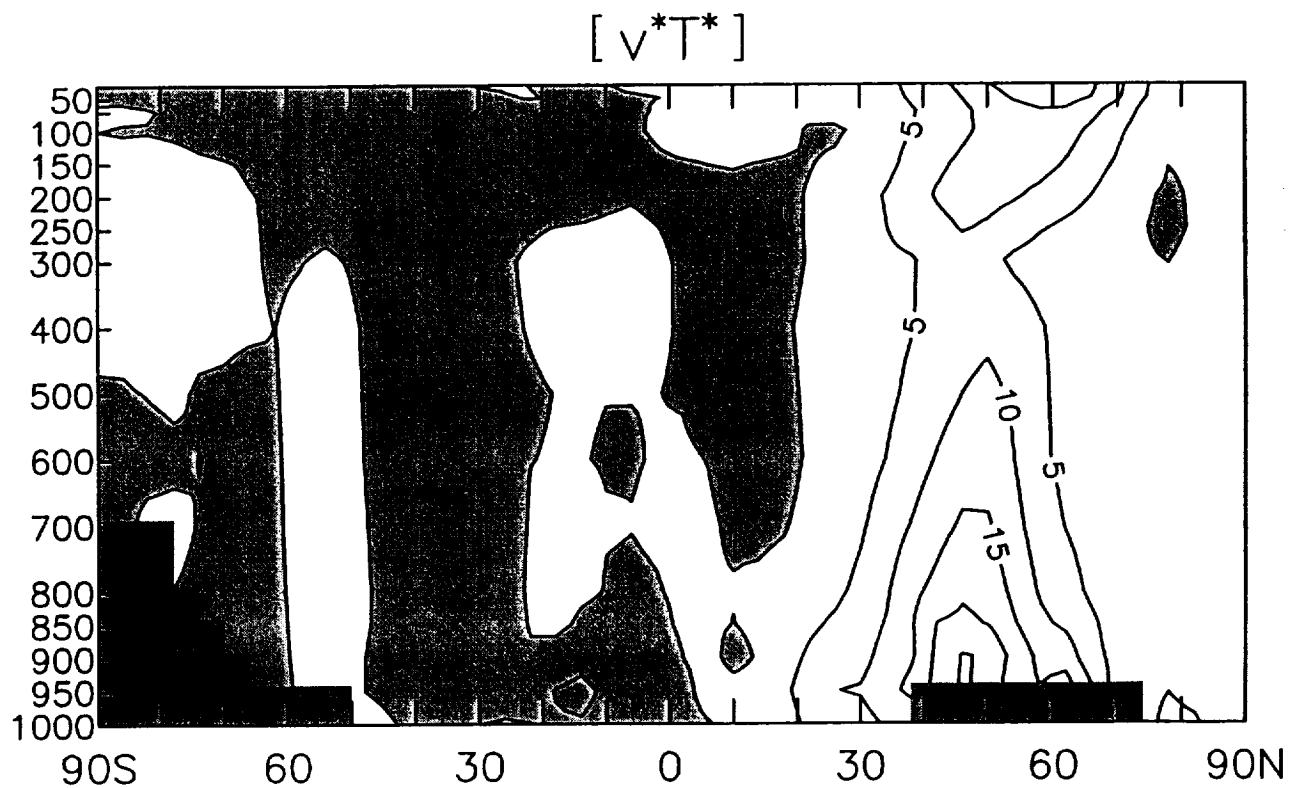
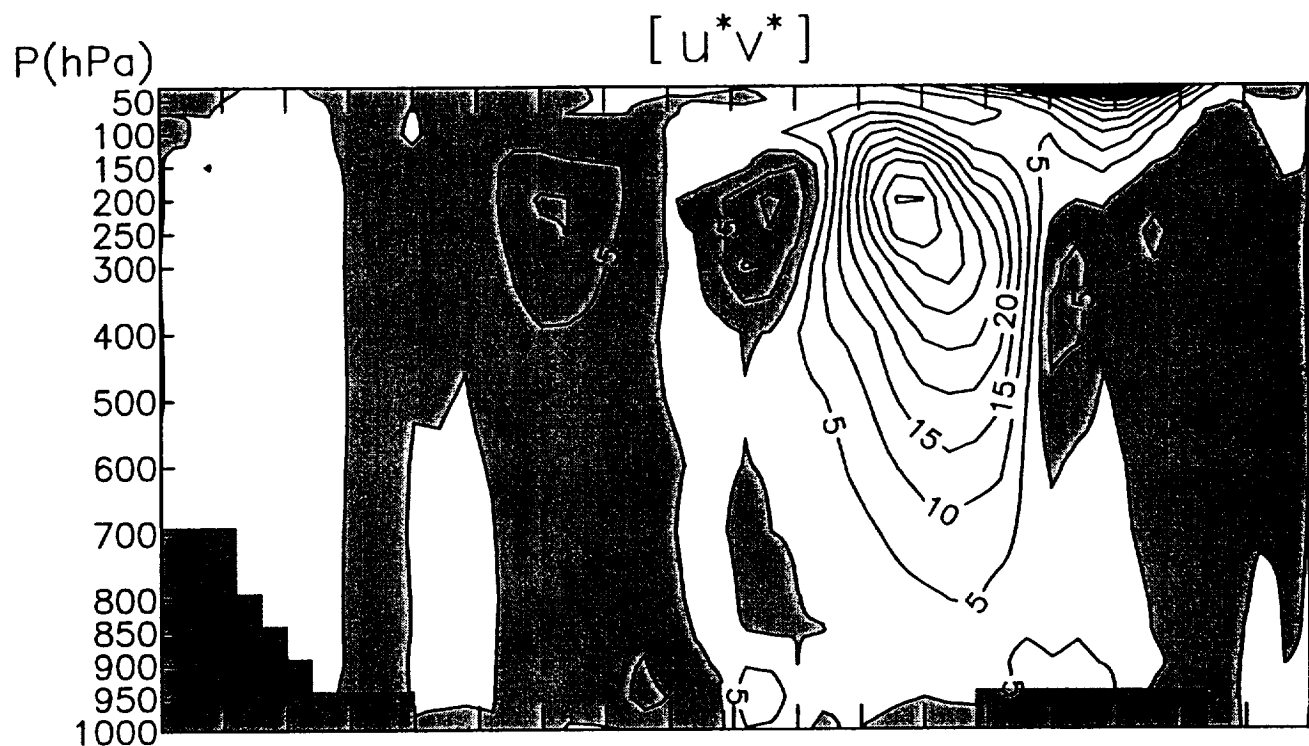
GEOS-2 McRAS, January, 1987



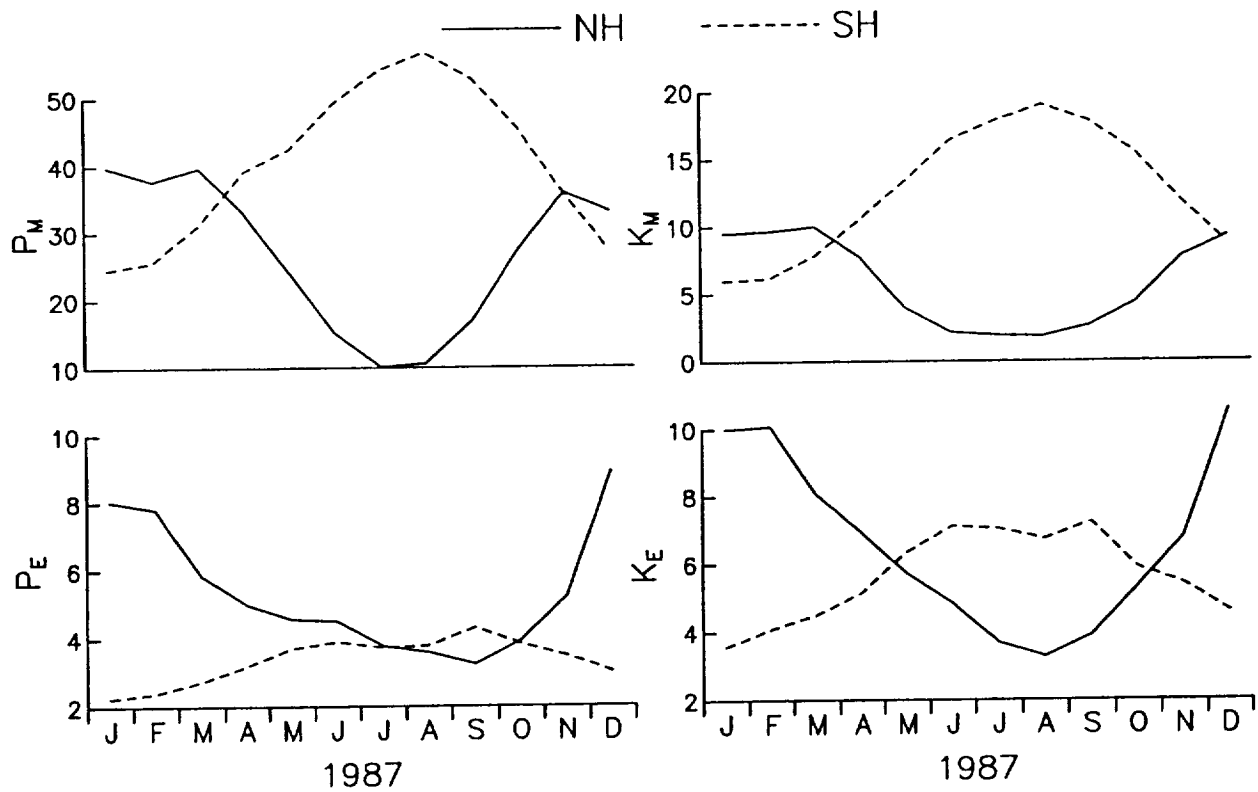
GEOS-2 McRAS, January, 1987



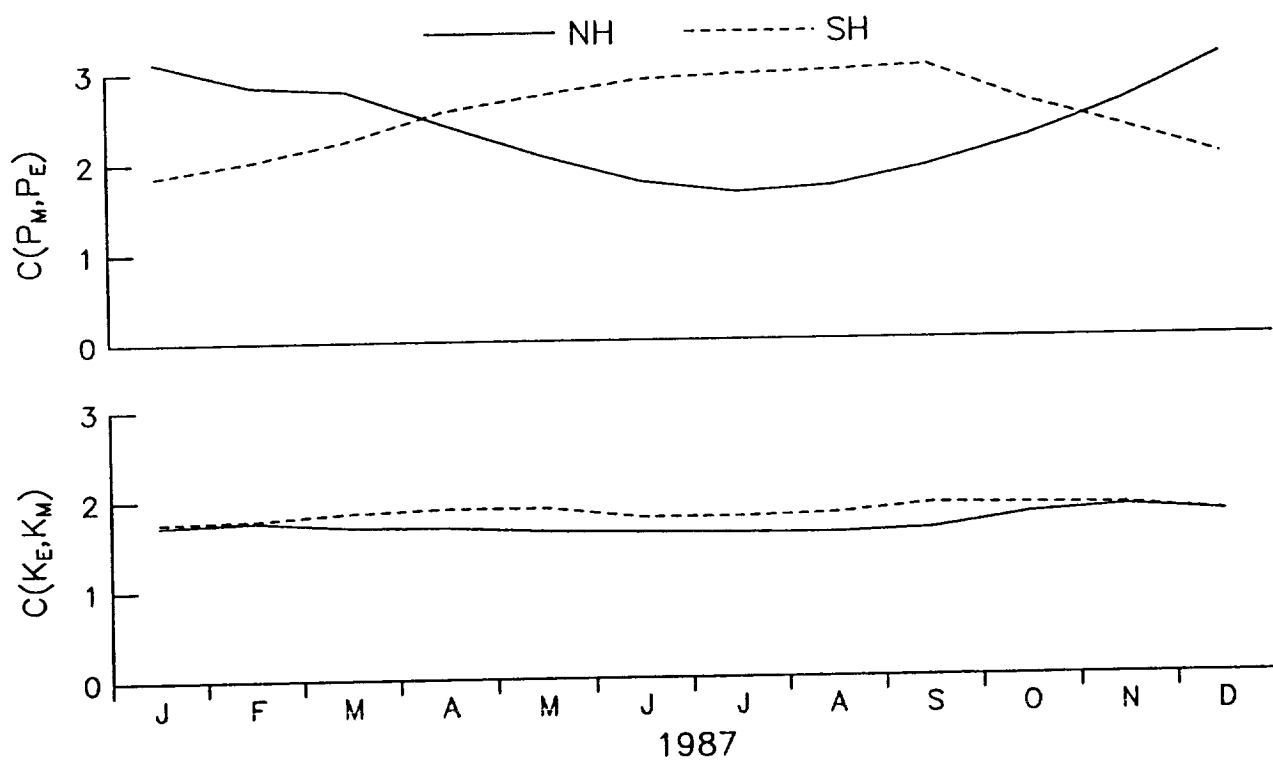
GEOS-2 McRAS, January, 1987



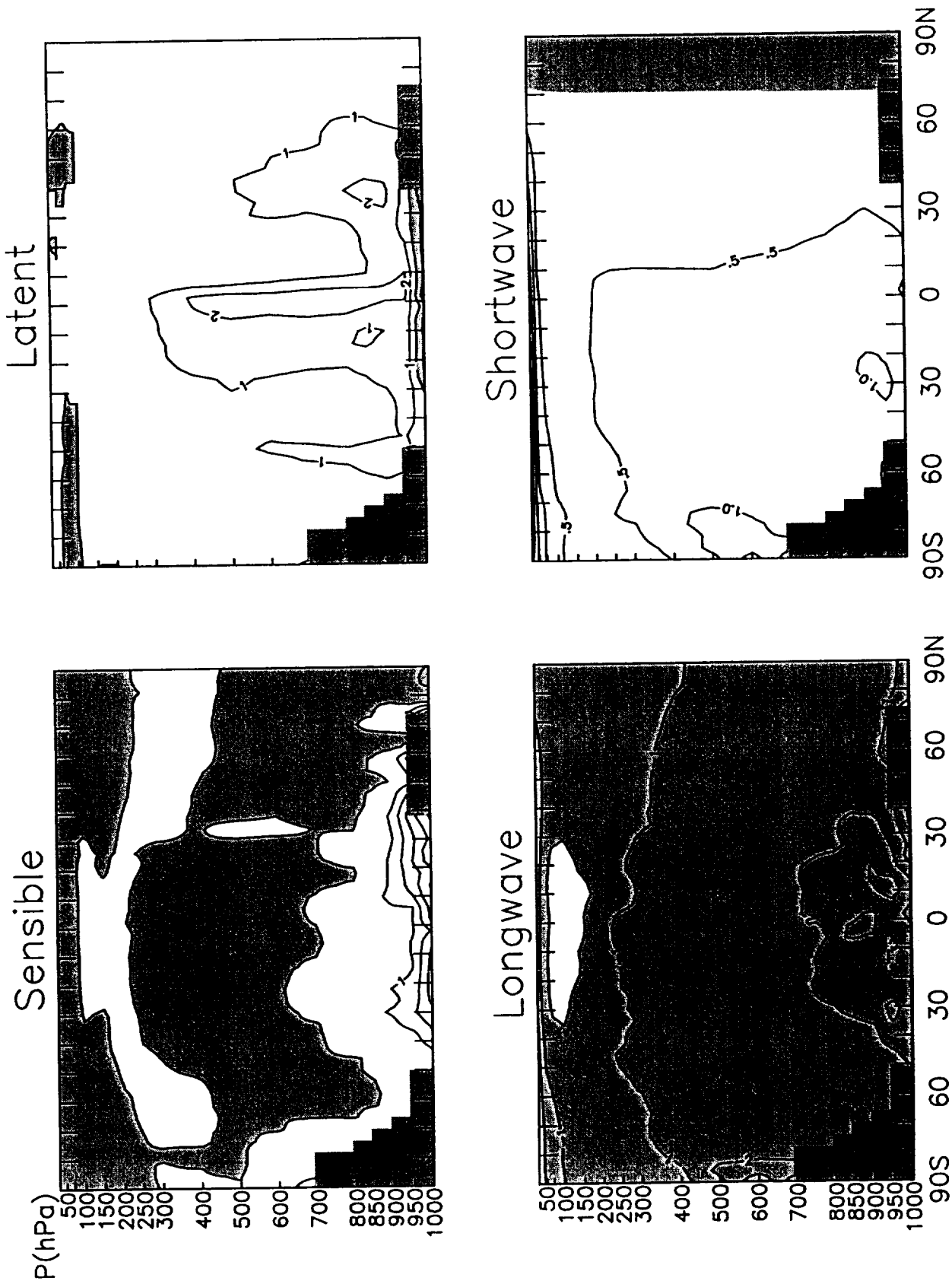
GEOS-2 McRAS Energy Terms



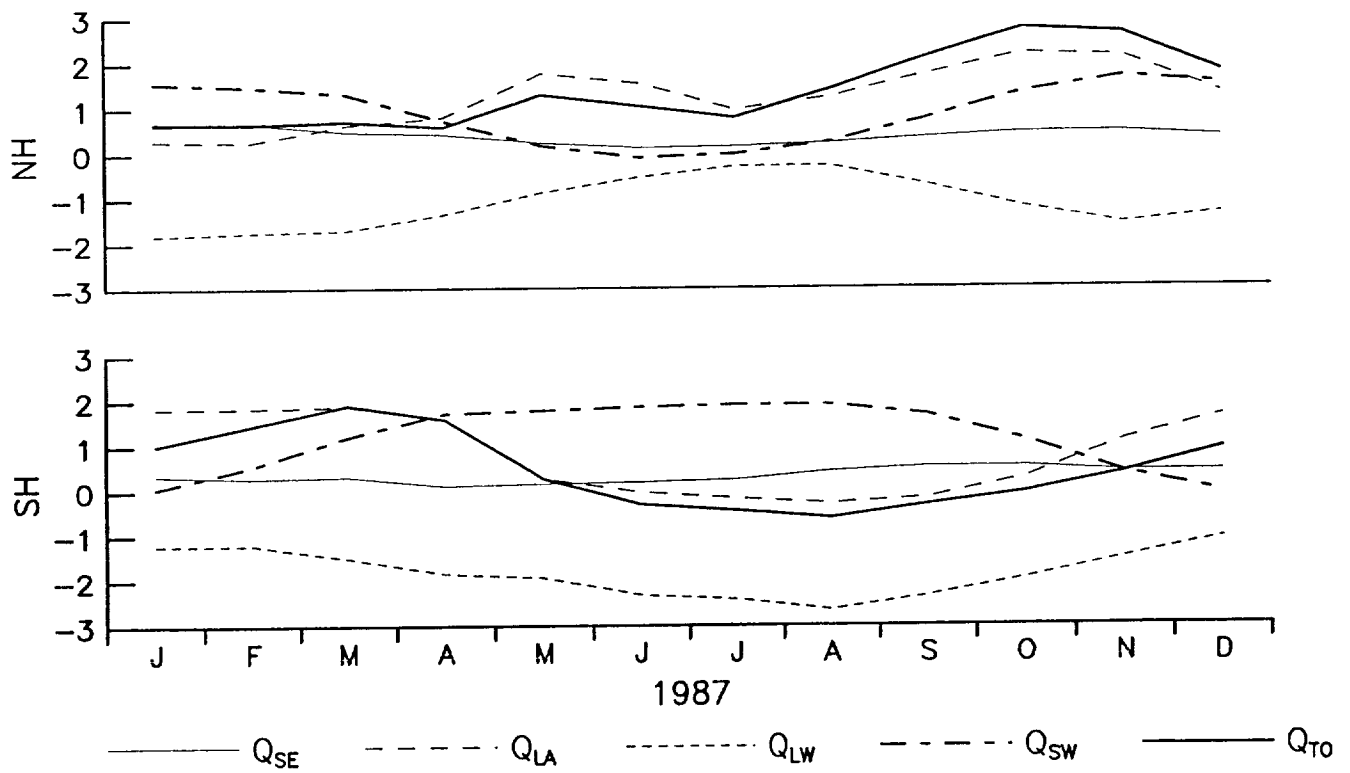
GEOS-2 McRAS Conversion Terms



GEOS-2 McRAS, January, 1987 Heating



GEOS-2 McRAS $G(P_M)$ Terms

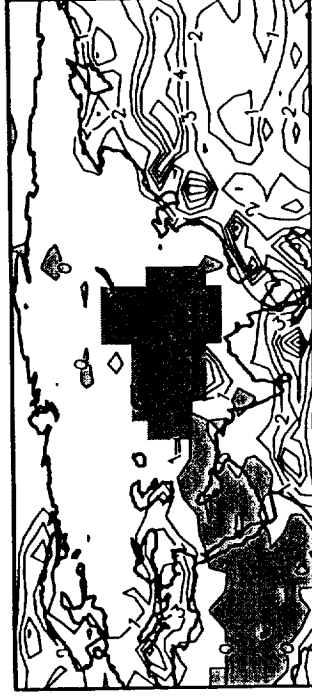


GEOS-2 McRAS 850 hPa Heating, Jan. 1987

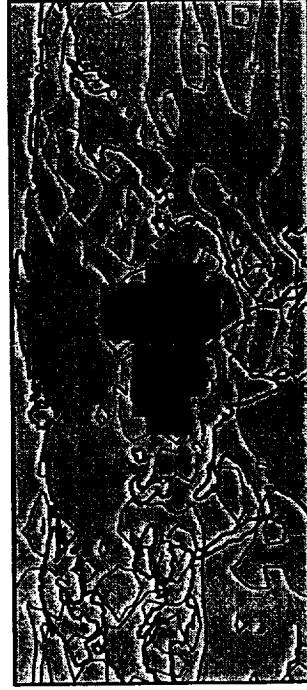
Sensible



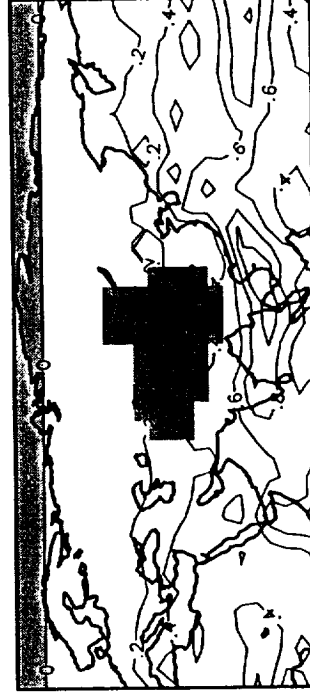
Latent



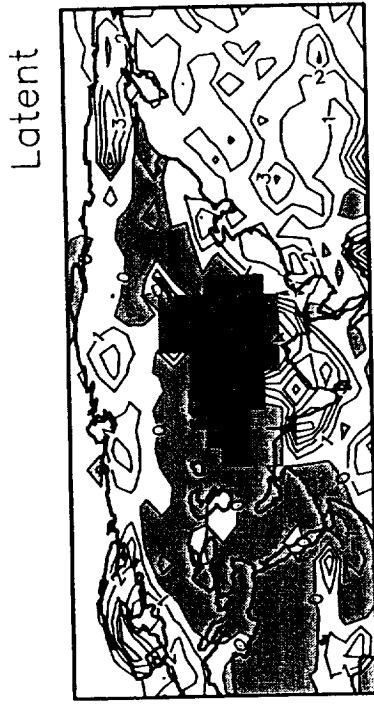
Longwave



Shortwave



GEOS-2 McRAS 850 hPa Heating, July 1987



GEOS-2 McRAS 500 hPa Heating, Jan. 1987



GEOS-2 McRAS 500 hPa Heating, July 1987

Sensible



Latent



Longwave



Shortwave



4. Torques and angular momentum of a noted signal in 1992

The angular momentum mass term based on both the NASA GEOS-1 DAS and the NCEP-NCAR reanalyses is given between 1991 and 1995. We focus on the large jump occurring in the middle of 1992 (Fig. 4.1). This jump also appears in the NCEP-NCAR reanalyses. (Fig. 4.2; though for 1991-2000). Noting that this jump in 1992 is also noted in independent measures of the length of day (Fig. 4.3 and 4.4) allows us to presume that it is a real signature. We then analyze the period June- July 1992 to determine that the change in these values are especially strong over the middle to high latitude southern hemisphere. The fractional covariance between belt and global signal is highest near 40 S latitude (Fig. 4.5). Focusing on that we look at 5 day sequences of the anomalies of pressure-based atmospheric angular momentum (Fig. 4.6) to see the rapid changes across the southern oceans near the 40 degree parallel. The movement is even more obvious with the daily progression between July 12 and 17 (Fig. 4.7), at the height of the episode.

Lastly we wish to contrast the two torque mechanisms that convey angular momentum between the atmosphere and solid earth for 1991-2000, here from the NCEP-NCAR analyses. In the mountain torque (Fig. 4.8), normal pressure gradients across topographic features, the high frequencies, such as those associated with the synoptic storms and signals are most evident, whereas the friction torque (Fig. 4.9), a tangential stress caused by low-level winds is much steadier.

Atmospheric Angular Momentum, Mass Term (M^P)
NASA GEOS-1 DAS

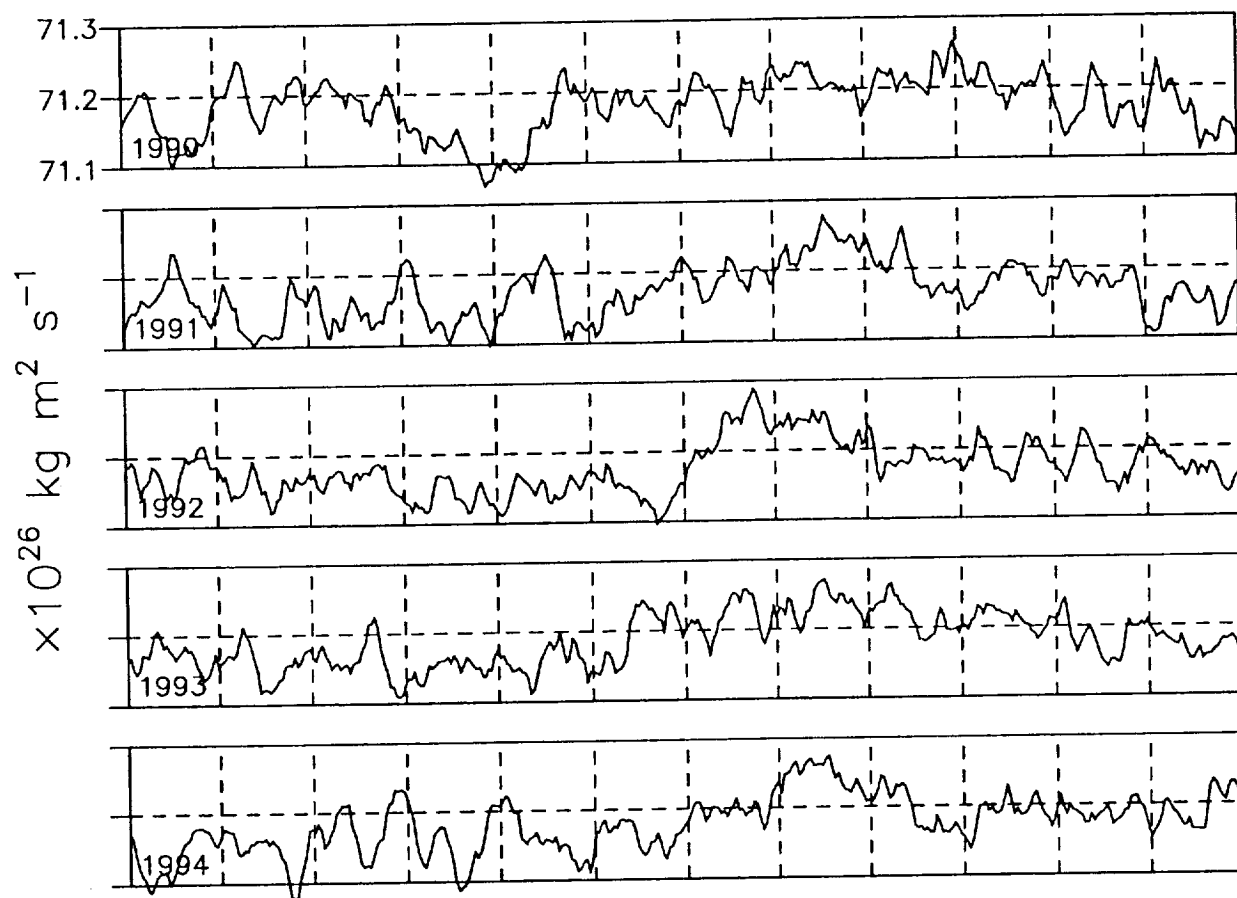


Fig. 4.1

Atmospheric Angular Momentum, Mass Term (M^P)

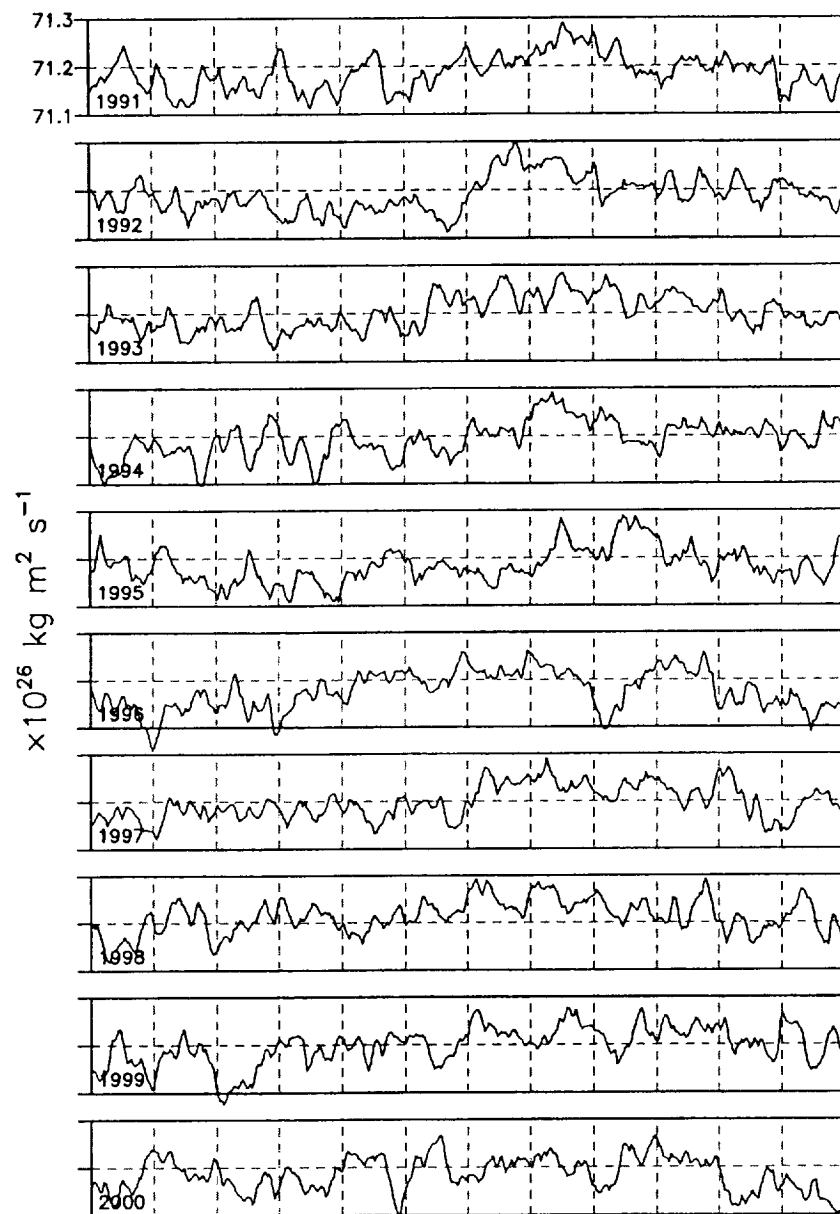


Fig. 4.2

Atmospheric Angular Momentum and Length of Day (mean terms removed)

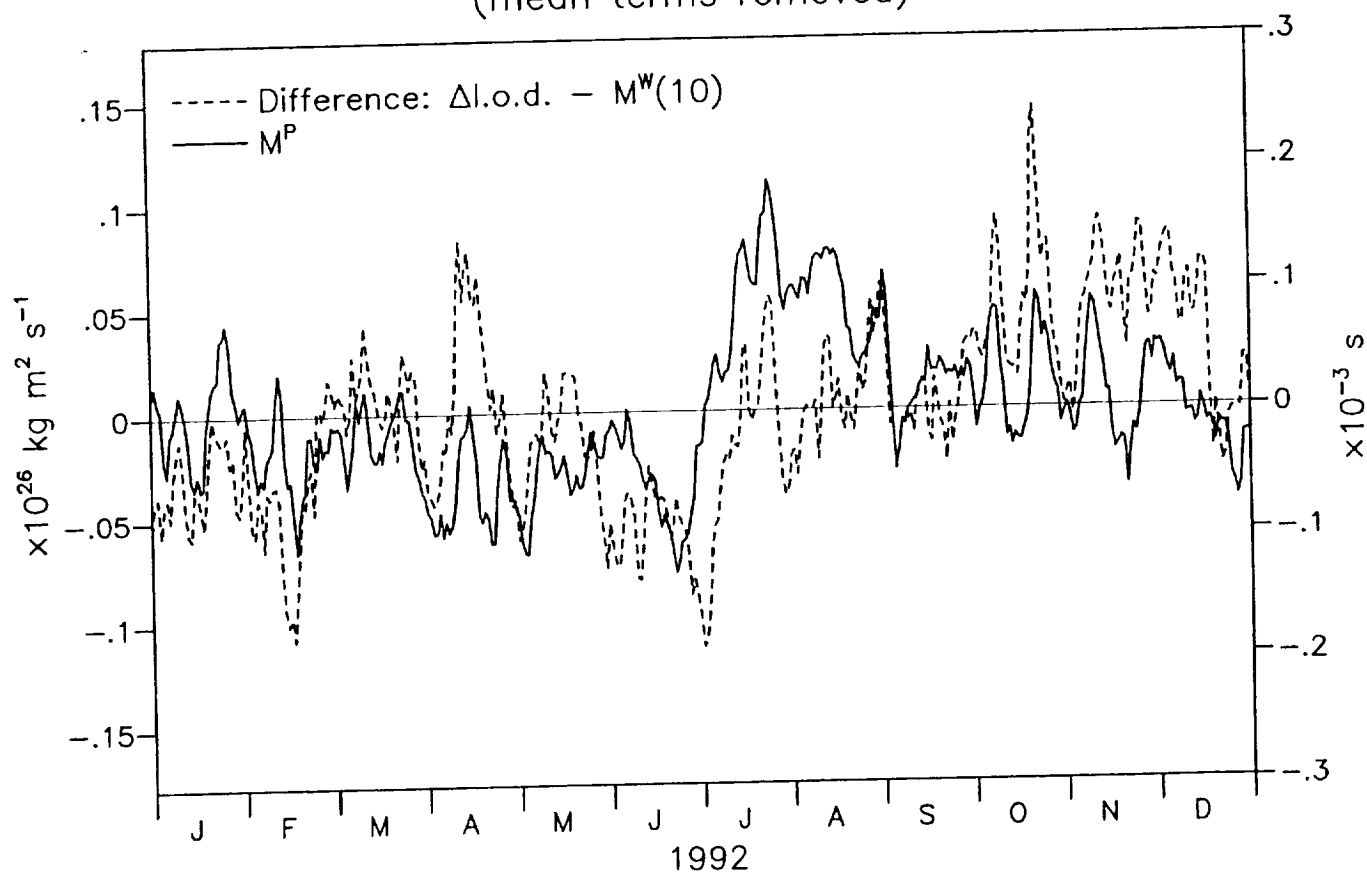


Fig. 4.3

NASA GEOS-1 DAS Atmospheric Angular Momentum and
Length of Day
(mean terms removed)

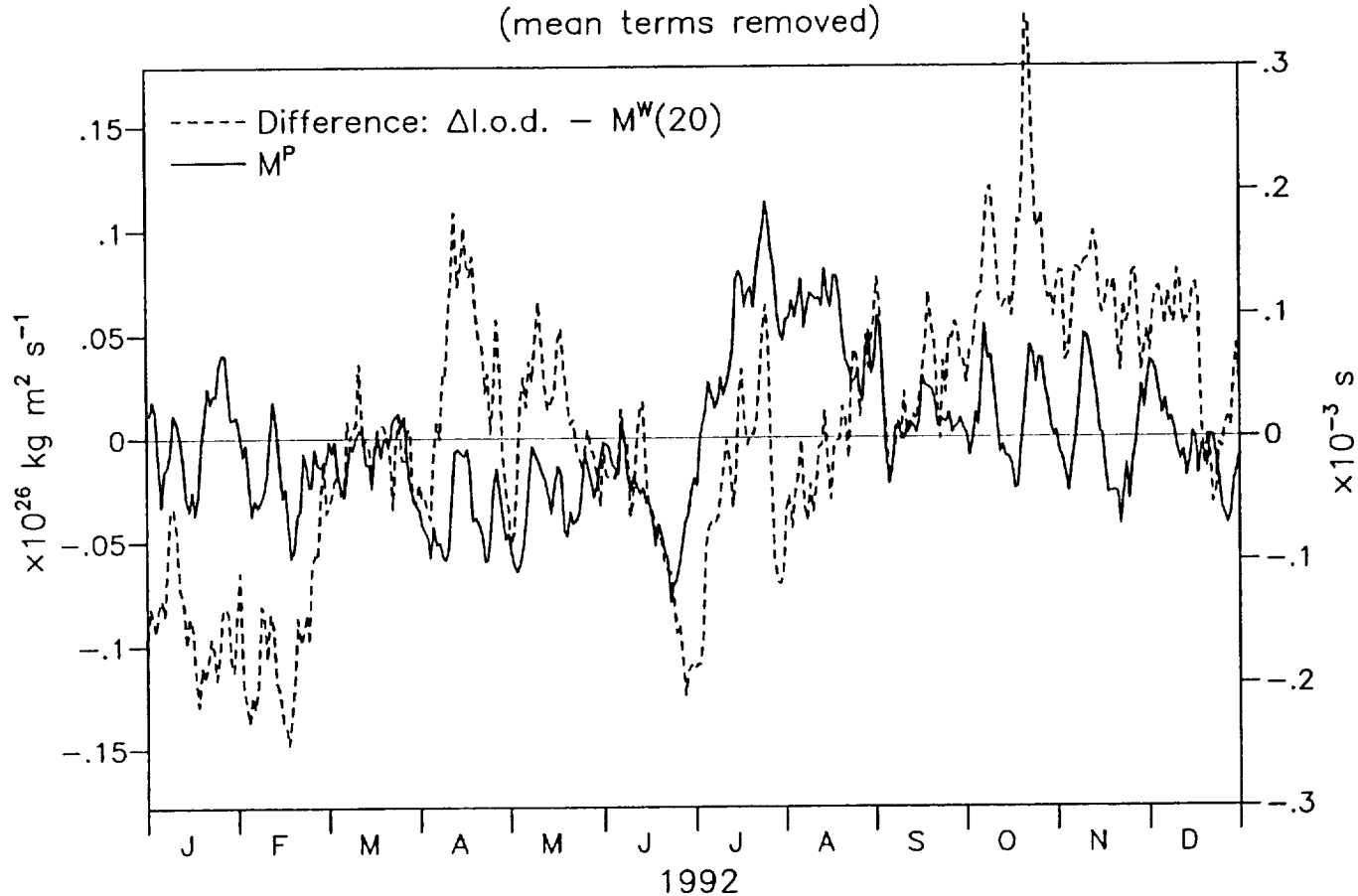


Fig. 4.4

M^P Anomalies, June–July 1992

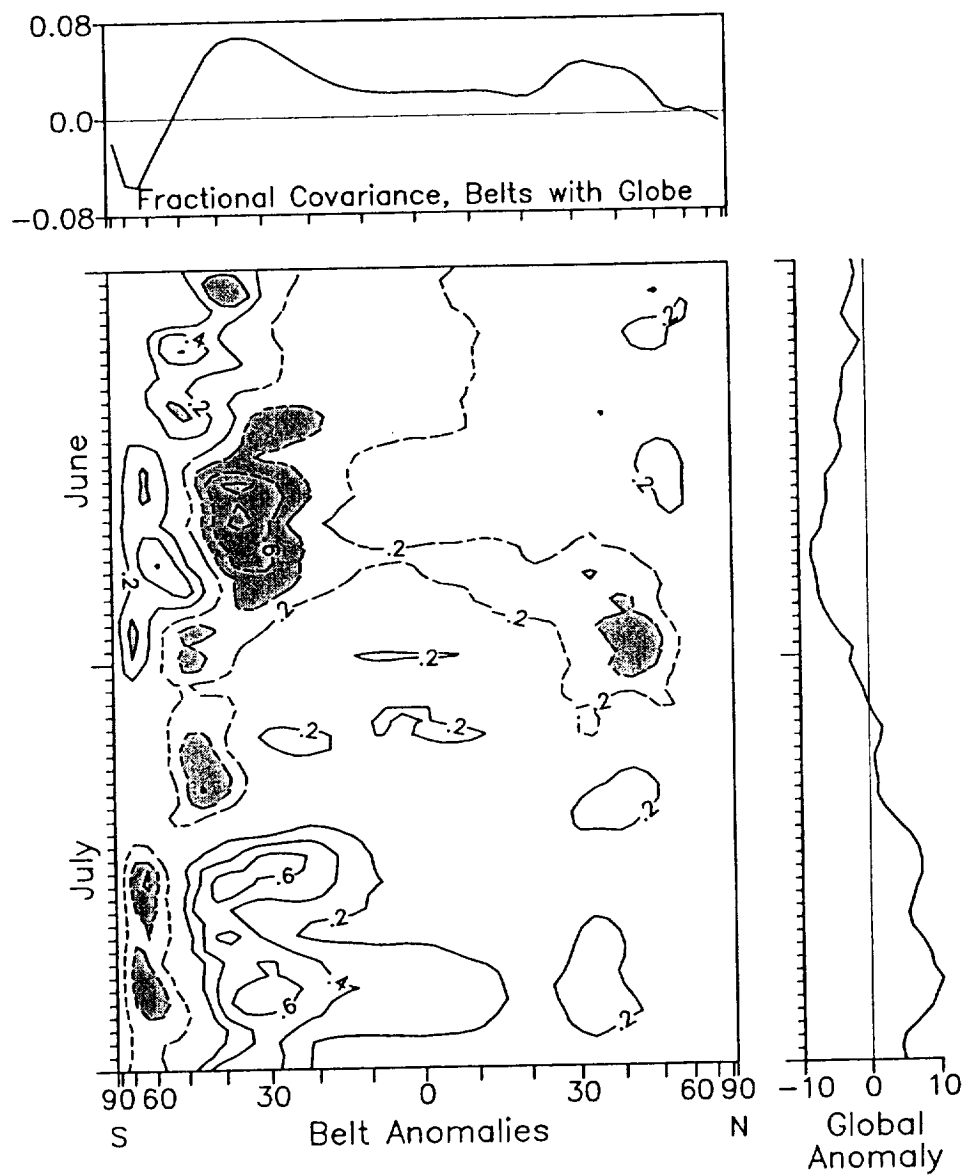


Fig. 4.5

Local M^P Anomalies

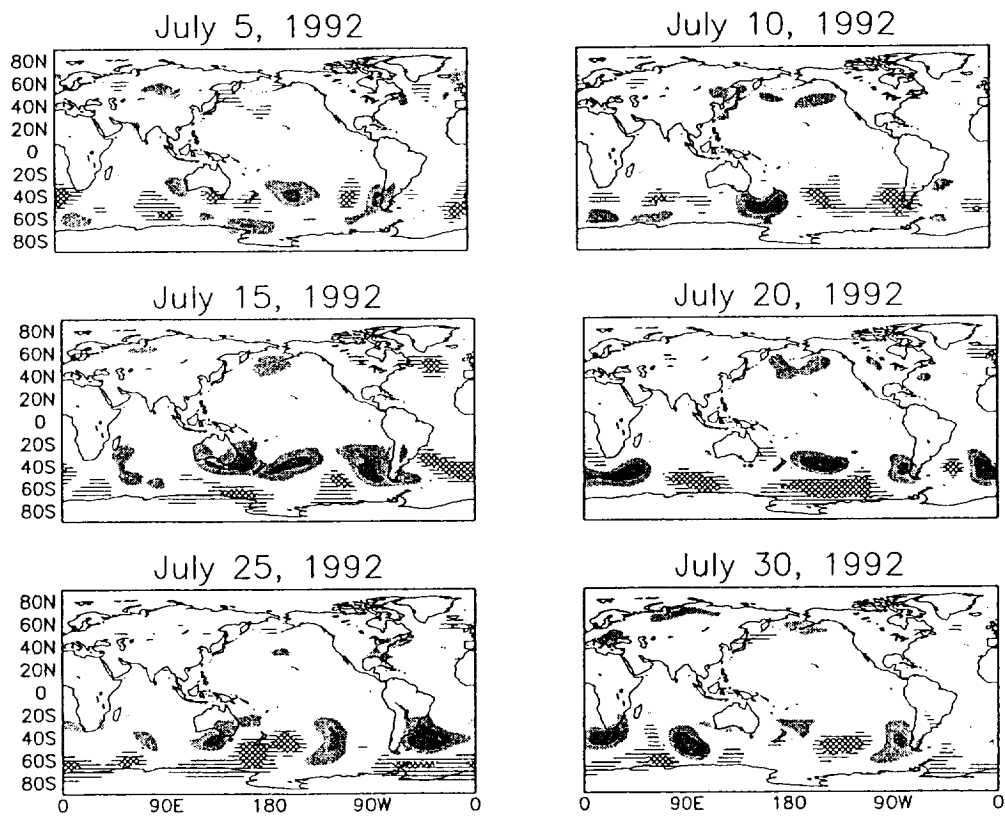
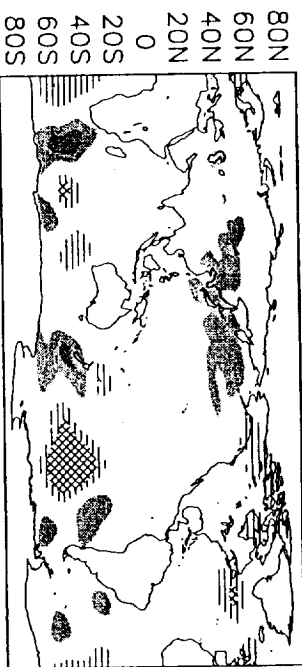


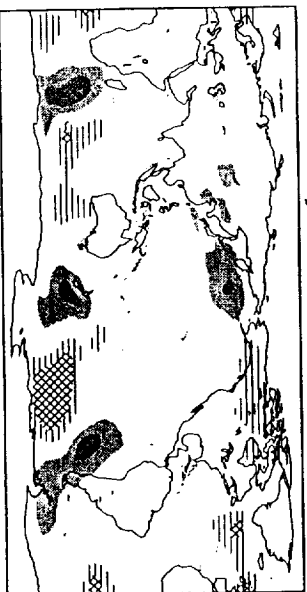
Fig. 4.6

Local M^P Anomalies

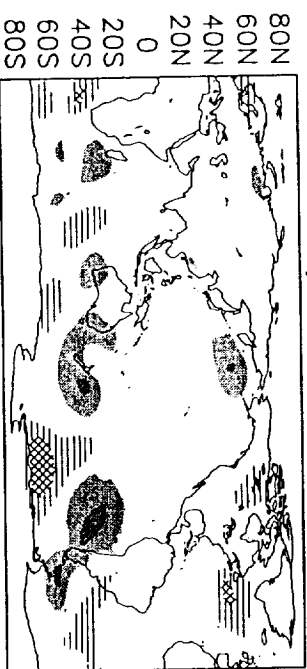
July 12, 1992



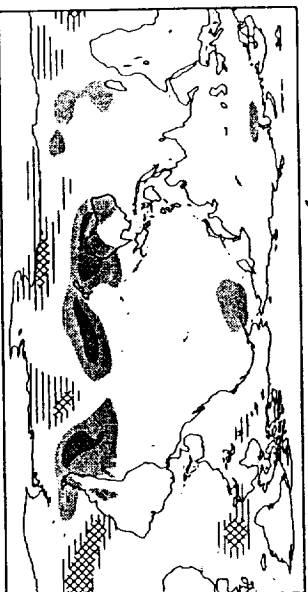
July 13, 1992



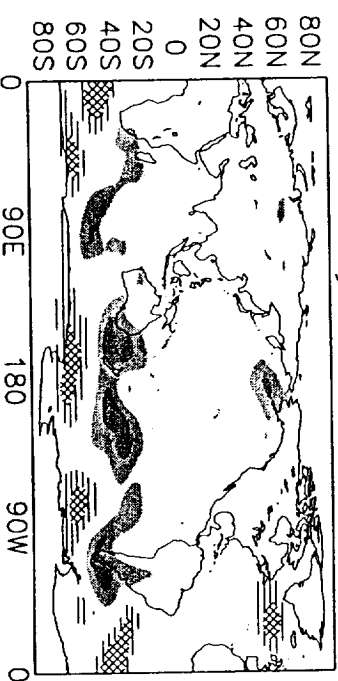
July 14, 1992



July 15, 1992



July 16, 1992



July 17, 1992

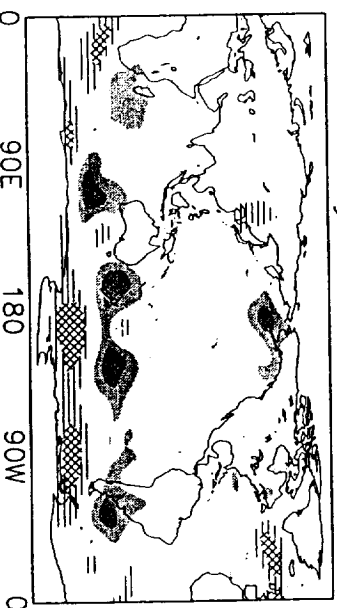


Fig. 4.7

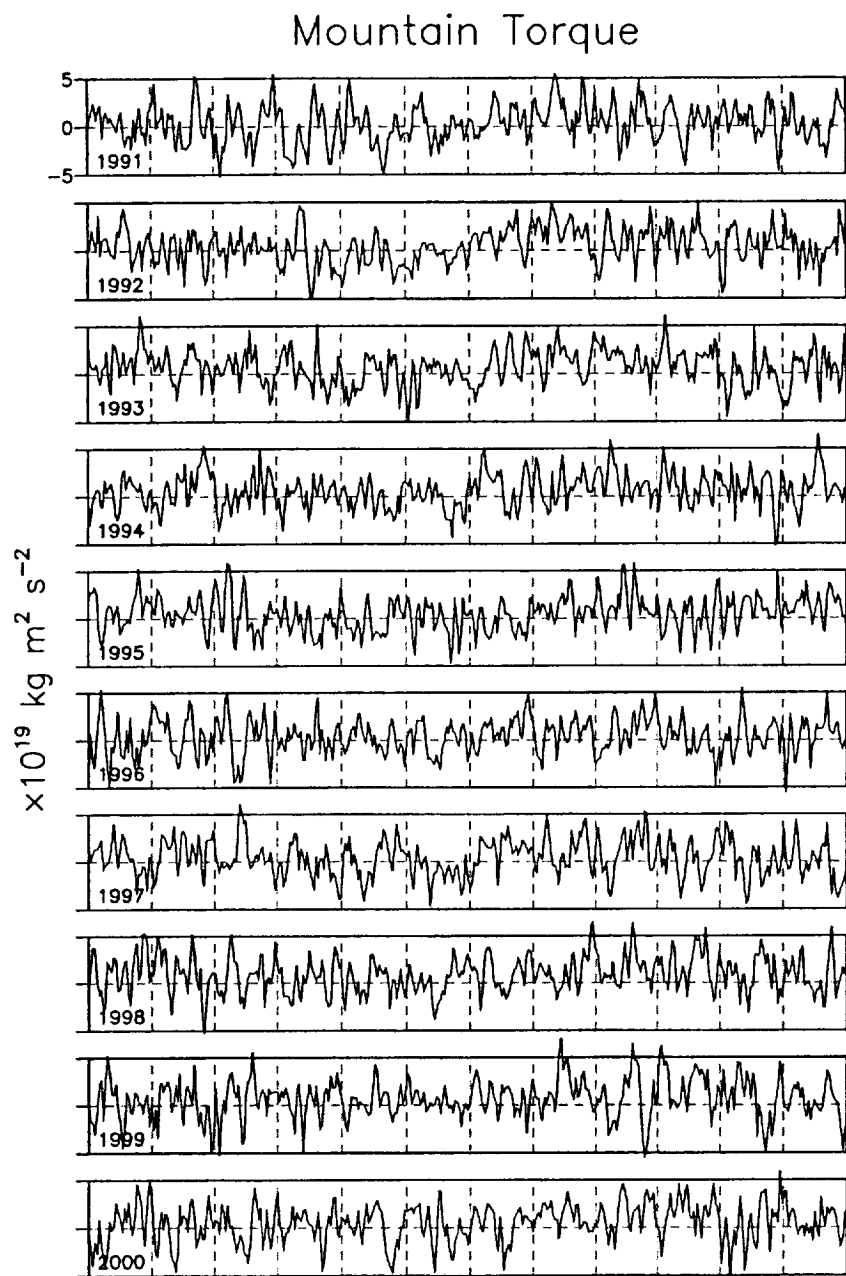


Fig. 4.8

Friction Torque

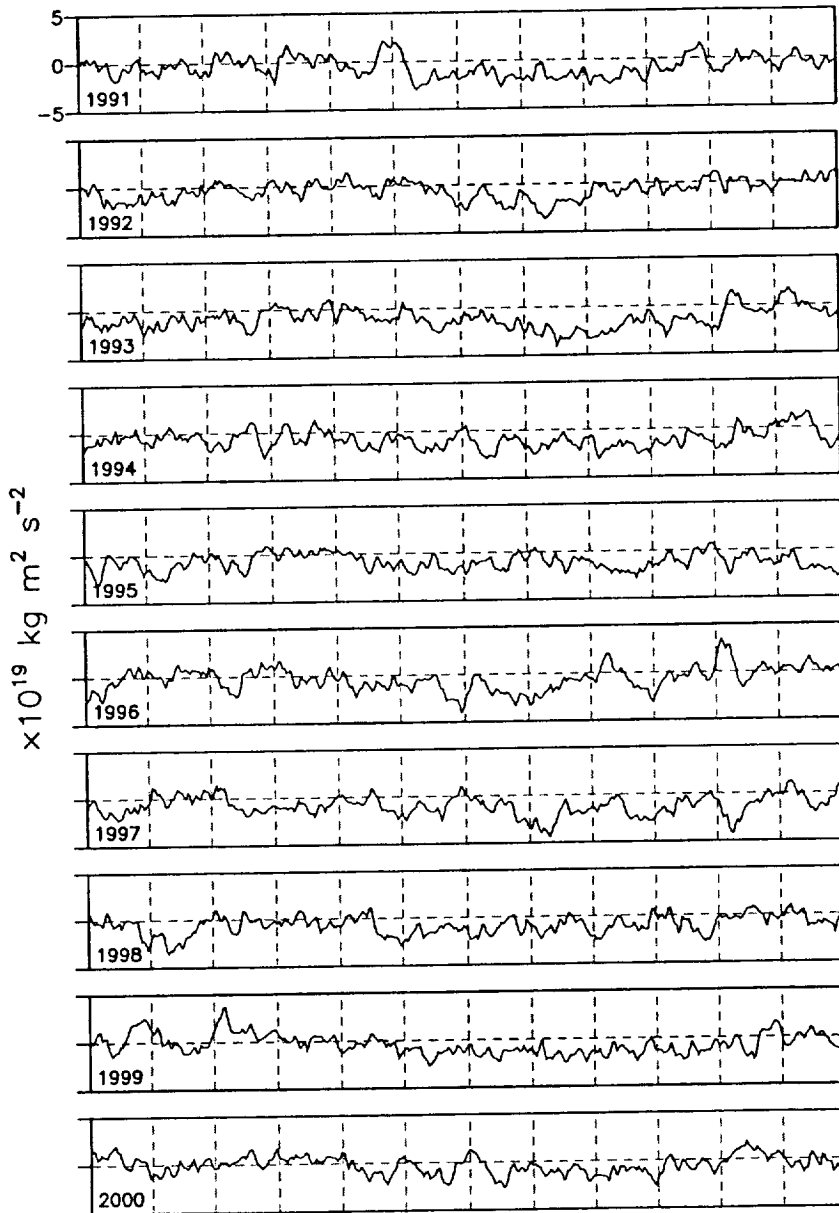


Fig. 4.9

We have compared several models participating in the Atmospheric Model Intercomparison Project, a project in which the general circulation models in the world's major weather centers have been run with prescribed sea-surface temperatures.. In the prior annual report, we noted that two models were available. We noted that for angular momentum, model-based quantities had improved the simulations, mostly because of improved parameterizations at the lowest latitudes. With sixteen models now available, we focus on the characteristics of the mean, and of the spread amongst models as well. The 17 year mean (1979-1995) of the AMIP-2 experiment has allowed us to examine the angular momentum between different ENSO years, and we have also studied a composite seasonal circulation. The 17-year mean appears to have a new bias of the models in AMIP-2 (Fig. 5.1) but the seasonal and interannual components are reasonably well simulated (Fig. 5.2 and 5.3). We note that eight of the model (four high, including the GLA, and four low) all demonstrate different characteristics in their departure from the NCEP-NCAR reanalyses in the zonal winds, from which are integrated the global atmospheric angular momentum (Figs. 5.4 and 5.5).

We have also looked at the large-scale models for AMIP moisture and moisture fluxes. Here, though we have focused more at the regional balances, because of other considerations, and this work is largely sponsored by other agency. Nevertheless, we were able to look at the flux divergence in the North American region, and see the progression of all the AMIP models. To the suite of AMIP models and that from reanalysis, we compare them with a NASA model, that of Sud and Walker (1999), including the McRAS scheme. That model result, the mean signal for each month of 4 years, is given here (Fig. 5.6) shows the seasonal progression of water divergence across North America. The mean seasonal signature is compared with the suite of AMIP models in Fig. 5.7

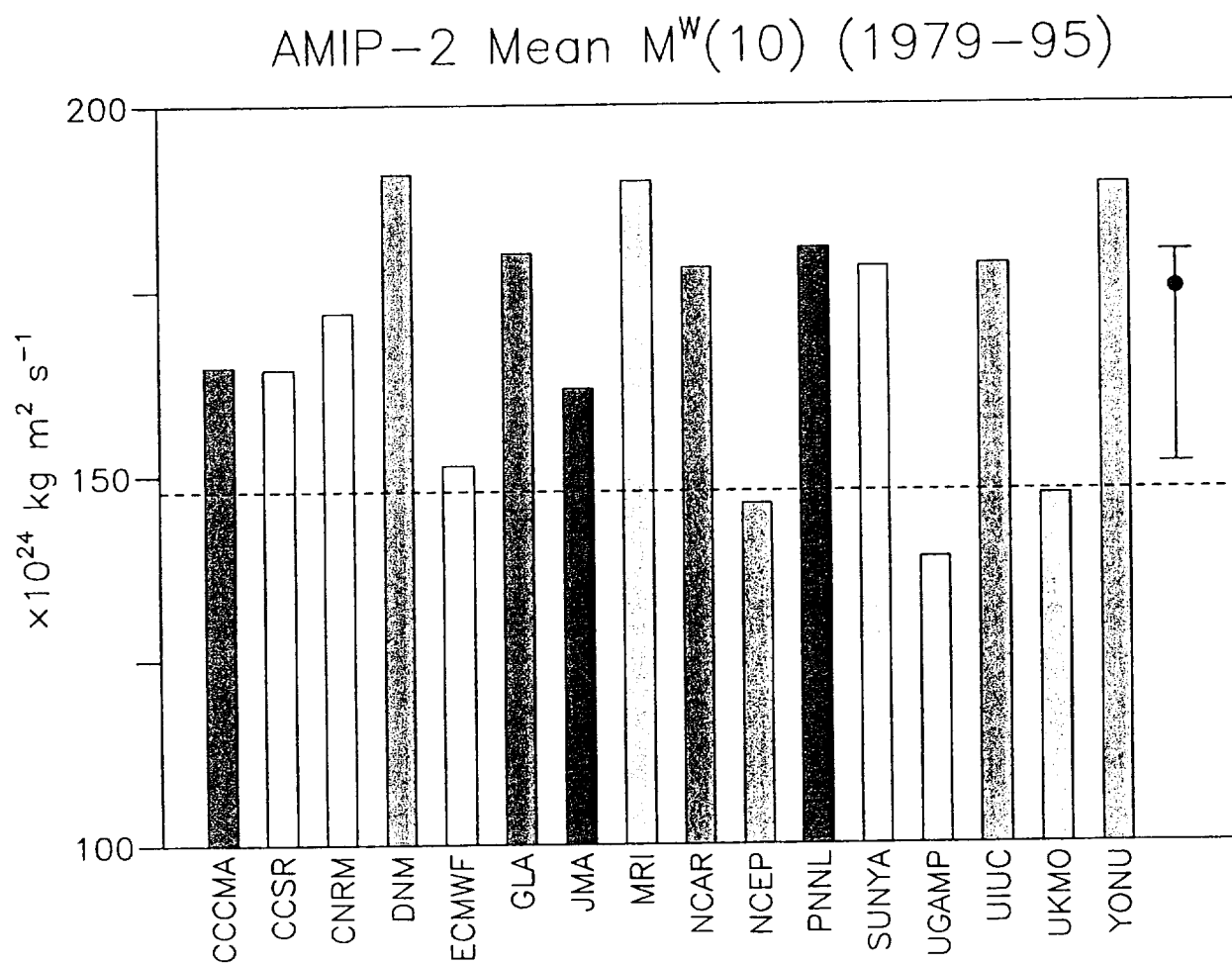


Fig 5.1

AMIP-2 $M^w(10)$, Seasonal Component

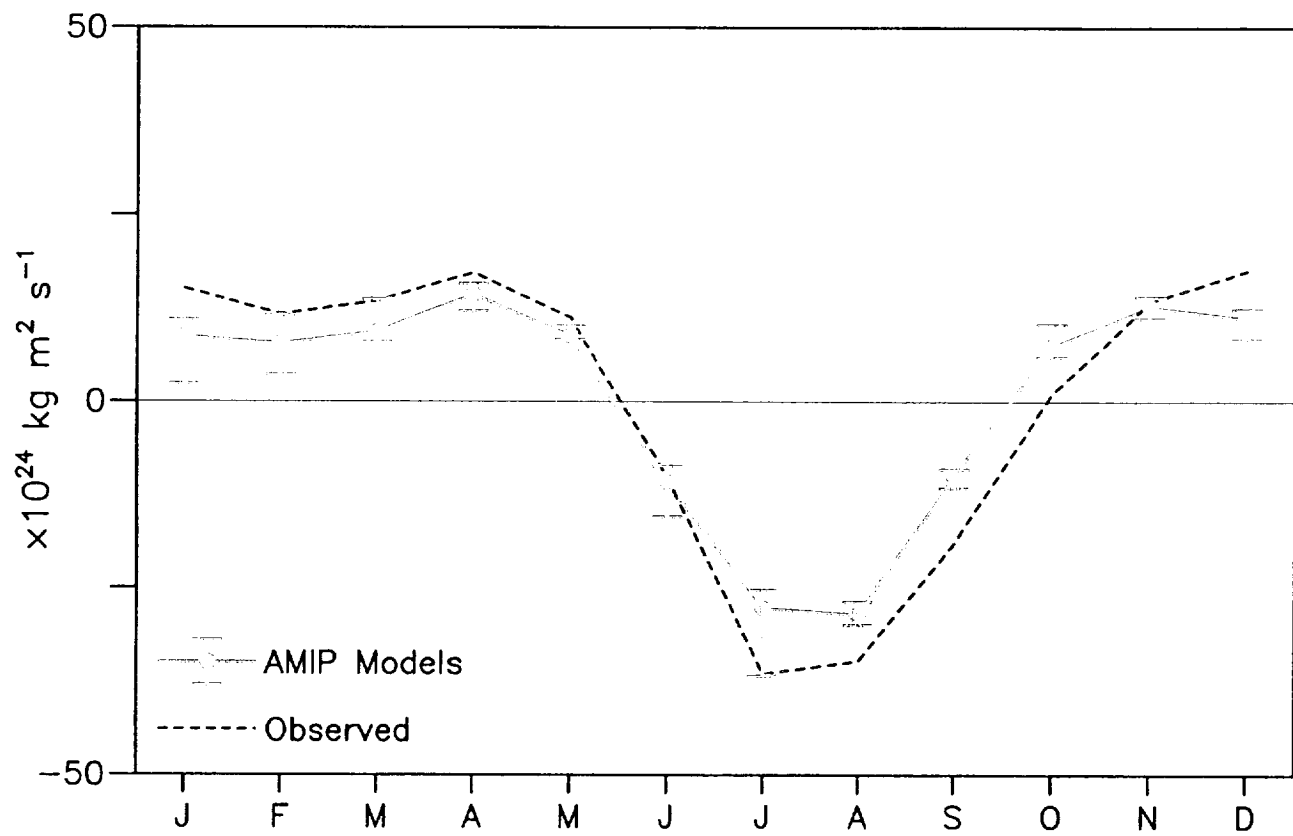


Fig. 5.2

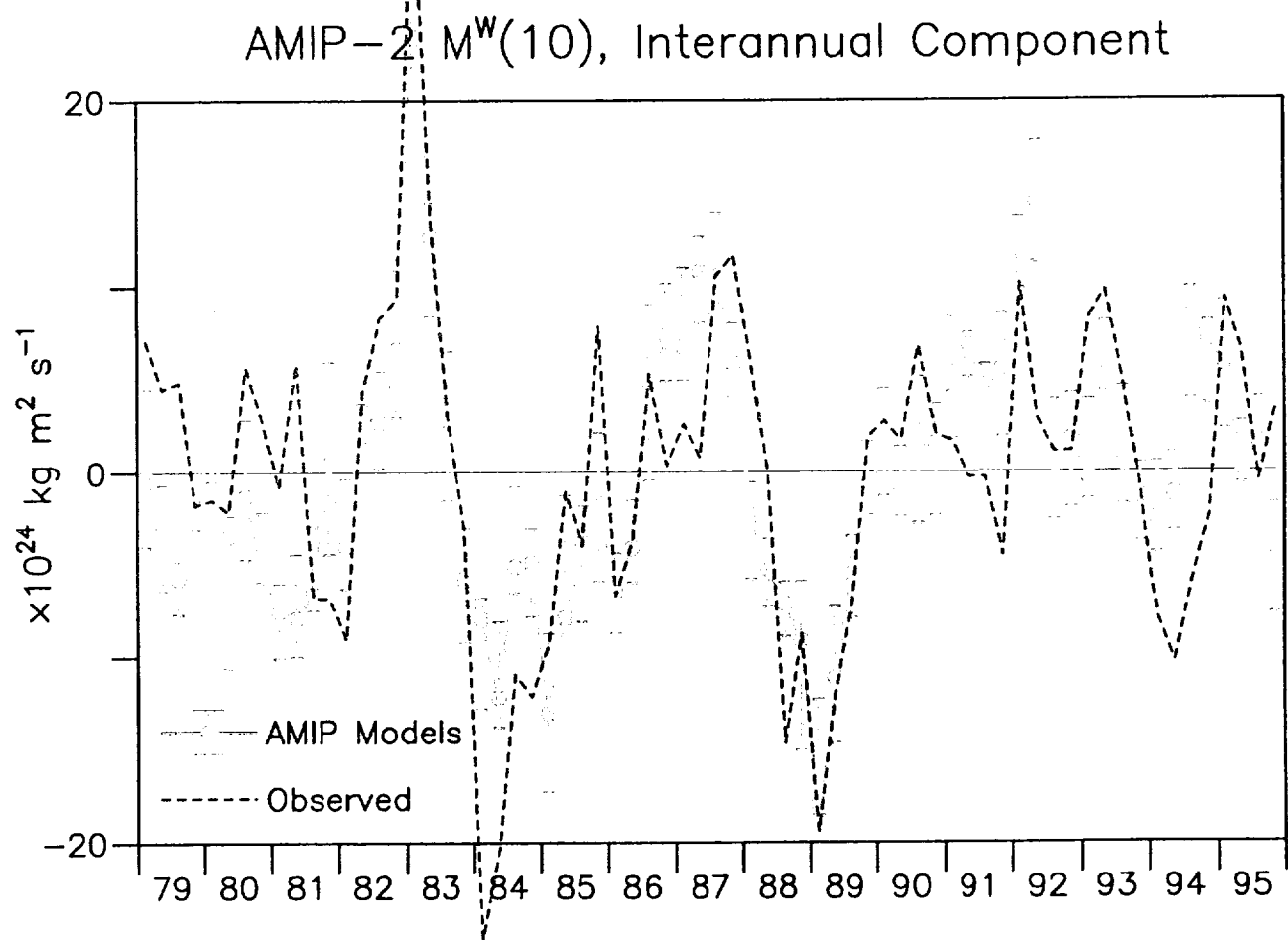


Fig. 5.3

AMIP-2 [u], 1979-1995

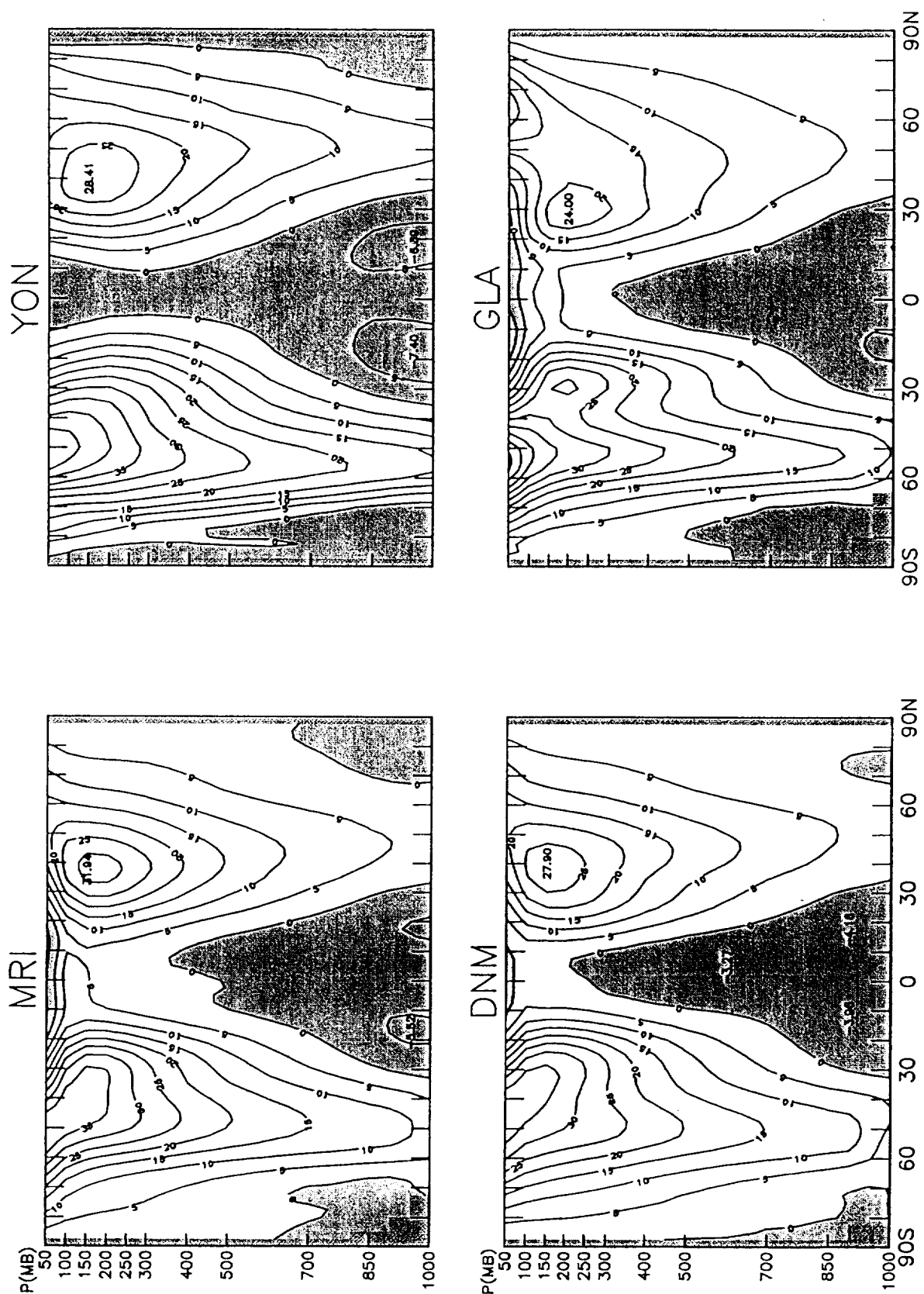


Fig. 5.4, part 1

Figure 10 consists of four contour plots arranged in a 2x2 grid, showing the probability distribution of bias for four different models: YON, GLA, MRI, and DNM. Each plot has a vertical axis labeled 'P(MB)' ranging from 50 to 1000 and a horizontal axis representing longitude from 90S to 90N. The plots show various contour lines and shaded regions representing different probability levels. The YON plot shows a large shaded region in the center, with contours labeled 1.00, 1.50, and 2.00. The GLA plot shows a large shaded region in the center, with contours labeled 1.00, 1.50, and 2.00. The MRI plot shows a large shaded region in the center, with contours labeled 1.00, 1.50, and 2.00. The DNM plot shows a large shaded region in the center, with contours labeled 1.00, 1.50, and 2.00.

Fig. 5.4, part 2

AMIP-2 [u], 1979-1995

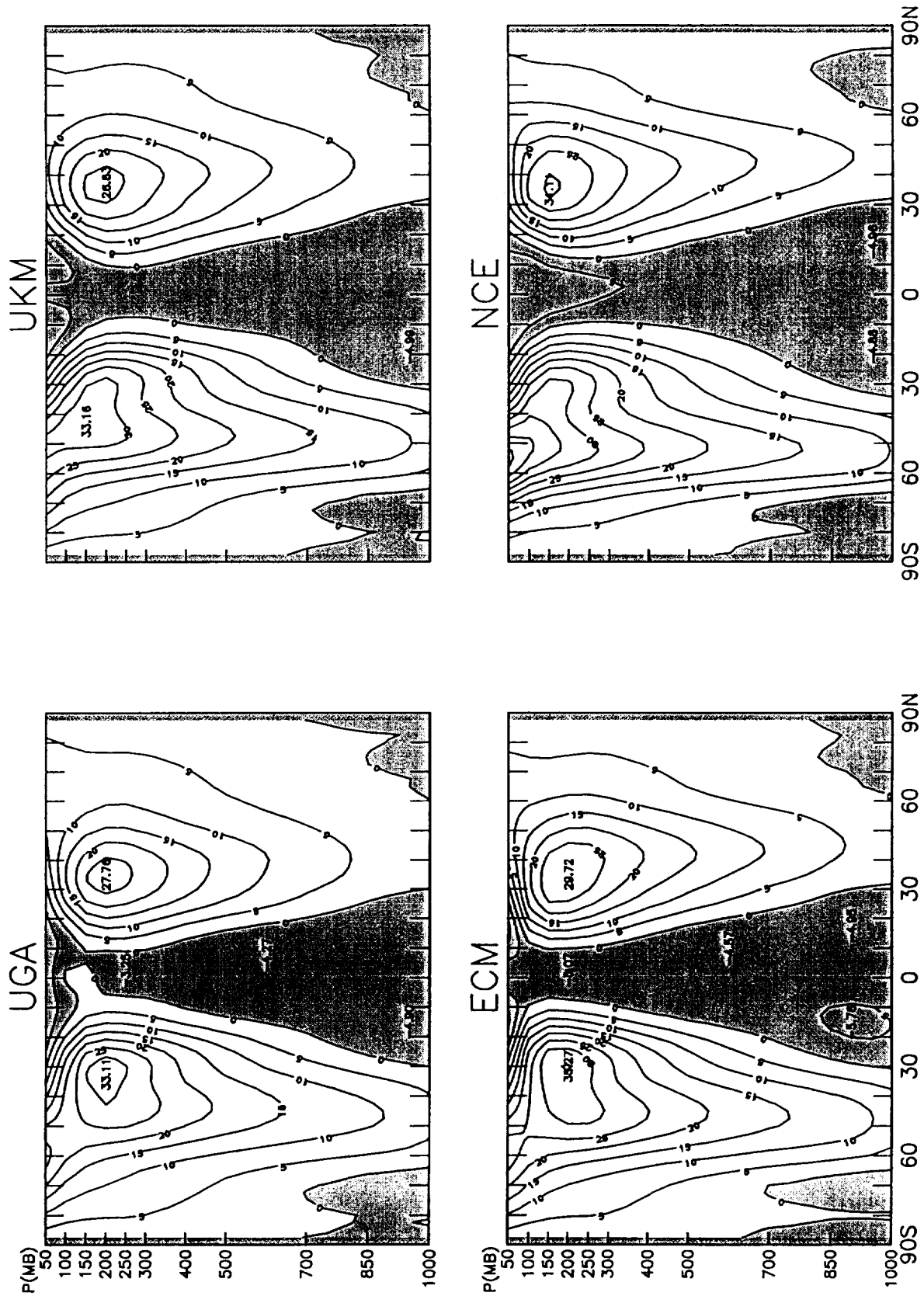


Fig. 5.5, part 1

Fig. 5.5, part 2

NASA Goddard MDL Mean $\text{div}(Q)$ (1987-1990)

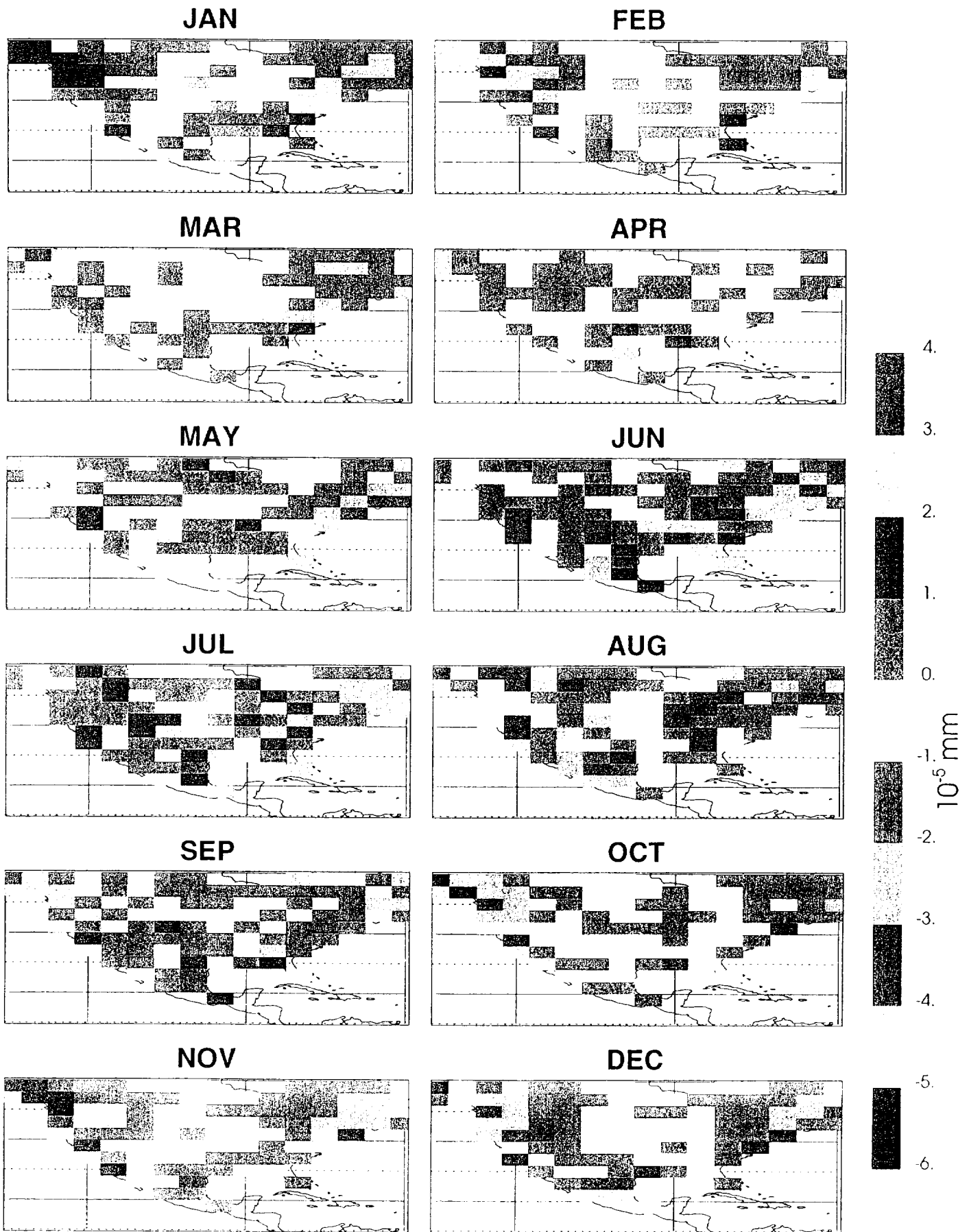


Fig. 5.6

Figure 1 is a line graph showing the monthly difference in precipitation (E-P) for the Conterminous US from January to December. The y-axis is labeled "E-P 10⁵ (mm/s)" and ranges from -3 to 2. The x-axis shows months from J to D. Three data series are plotted: MDL AVG E-P (solid line), RNL div(Q) (dashed line), and NASA Goddard (dotted line). Each data point includes vertical error bars. The MDL and RNL series show a significant deficit in winter (J-F) and surplus in summer (J-A), while the NASA Goddard series shows a more moderate deficit in winter and surplus in summer.

Month	MDL AVG E-P (mm/s)	RNL div(Q) (mm/s)	NASA Goddard (mm/s)
J	-1.5	-1.5	-0.5
F	-1.8	-1.8	-0.5
M	-1.2	-1.2	-0.5
A	-0.5	-0.5	-0.5
M	0.0	0.0	0.0
J	0.5	0.5	0.0
J	0.8	0.8	0.0
A	1.0	1.0	0.0
S	0.5	0.5	0.0
O	0.0	0.0	0.0
N	-0.5	-0.5	0.0
D	-1.0	-1.0	0.0

Fig. 5.7

Diabatic heating and the Atmospheric Energy Cycle

David A. Salstein

Atmospheric and Environmental Research, Inc., Cambridge, MA 02139, USA

1. Conservative quantities and their budgets

The overall energy of the atmosphere falls into the class of conservative quantities. As such, in the absence of exchanges of heat or other energy from outside the atmosphere, the total energy of the atmospheric system remains fixed, although it can change its form. Other examples of conservative properties in the atmosphere are angular momentum and mass, the latter counting dry air and of water mass separately; such a quantity cannot change its amount unless specific transfers occur from outside a system. This framework of conservative atmospheric processes was much appreciated and researched by Prof. Peixoto in a series of papers. His seminal book with Dr. A.H. Oort (Peixoto and Oort, 1992) was a culmination of much of that research.

Atmospheric angular momentum, for example, only changes by transfers across the surface below, but these can be important (e.g., Rosen, 1993). Thus, the changes in the angular momentum of the atmosphere are observed to cause very small but measurable variations in the rotation rate of the earth, as reckoned by changes in the length of day (Fig. 1). As a second example, the total water mass of the atmosphere is modified by exchanges of water substance into and out of the atmosphere, accomplished by means of precipitation and evaporation. Prof. J. P. Peixoto was the author of many papers concerning moisture fluxes and divergences (e.g. Peixoto, 1959; Starr et al., 1965). Such a divergence calculation using recent data over part of North America, a region that has long been the focus of intensive water resources studies, is given in Fig. 2.

2. Diabatic heating, total and components

Here we make a distinction of true heating, which changes the energy of a fluid, termed "diabatic," in contrast with those temperature tendencies of a fluid that are due merely to changes in pressure ("adiabatic"). Relevant processes that heat the atmosphere diabatically consist of sensible heating, by contact with either other air parcels or a surface, by latent heat release from phase changes of water vapor, by means of shortwave radiation from solar heating, and longwave radiational emission, a cooling (negative heating) process. The total diabatic heating is the sum of these individual processes. Because the diabatic heating components cannot be directly observed, we can turn to an atmospheric general circulation model to estimate them. The atmospheric model may be used alone, as a simulation, with only initial and boundary conditions; however, when it is part of a model-assimilation system it will make use of the observations as well to define the state of the atmosphere. Estimating rates of diabatic heating in such a way is, of course, greatly dependent upon the details and parameterizations of the particular model used.

An alternative to determining the total diabatic heating information is to examine the overall thermodynamic changes and infer the heating field that must cause such a change. This method will produce total diabatic heating, but not the individual components of diabatic heating. In comparing the sum of the diabatic components to the thermodynamics-derived fields, we can gain confidence in the models used. In fact, the best success in this comparison is at the lowest levels. The principal advantage to the component method is that by using it we can understand how each physical mechanism

Conservation of Angular Momentum in the Earth-atmosphere System (mean terms removed)

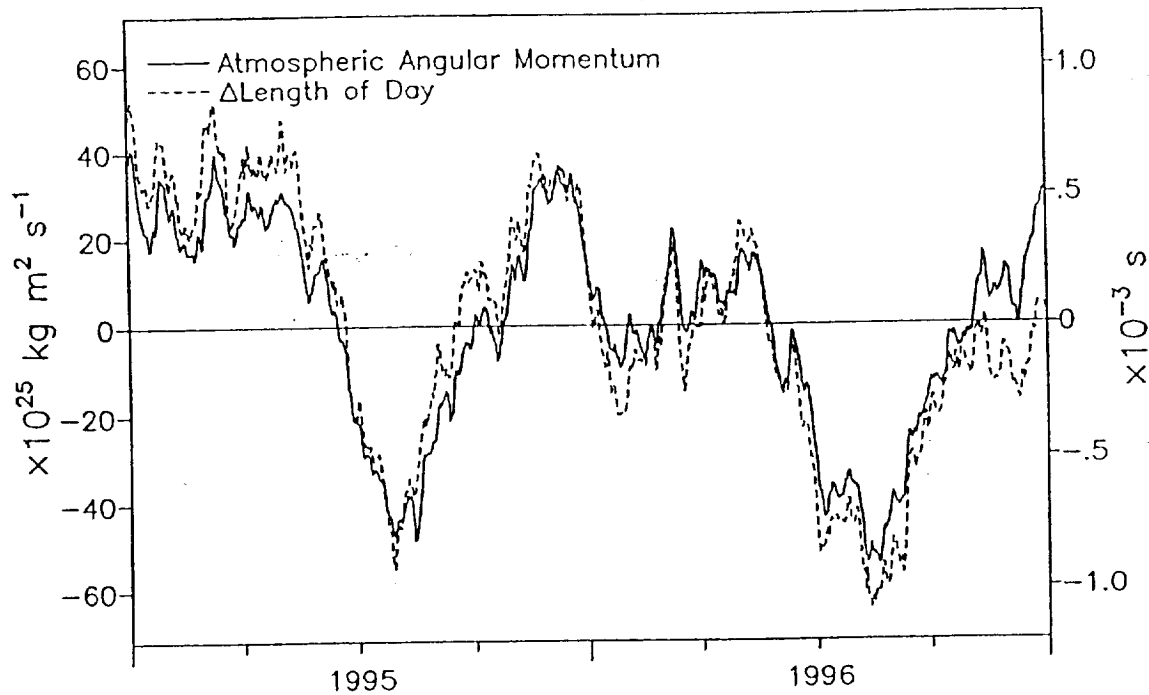


Fig. 1. The angular momentum of the atmosphere based on zonal winds from the NCEP/NCAR reanalysis system (solid line, scale at left) for a two-year period, and departures of the length of day from a constant (dashed line, scale on right). Mean terms are removed. Conservation of angular momentum would imply a near agreement on the scales plotted.

Divergence of Water Vapor at 850 hPa

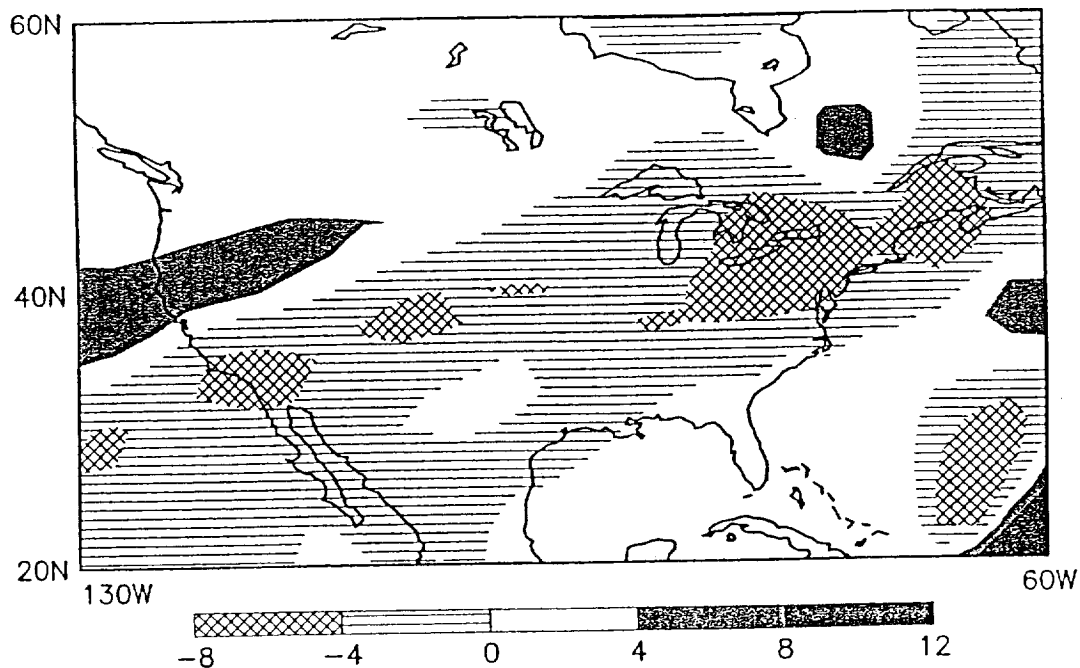


Fig. 2. Divergence of water vapor at 850 hPa based on the NCEP/NCAR reanalysis system. Vertical integrals of this term may be matched to the difference between evaporation and precipitation to the estimated conservation of water mass based on the models.

contributes to the energy cycle independently, through the generation of available potential energy.

We first determined the diabatic heating components with the United States' National Aeronautics and Space Administration (NASA)'s Goddard Laboratory for Atmospheres analyses for some months of the Global Weather Experiment (GWE) in 1978-1979. Subsequently we have examined the diabatic heating rates and energy cycle from 14 years of output from a later period, the full calendar years of 1981-1994. This period was part of the continuation from the GWE, and uses the Goddard Earth Observing System Data Assimilation System, on which we will concentrate here (Schubert et al., 1983).

We note that the largest portion of the latent processes results from condensation due to the process of cloud formation. It may occur by means of a number of distinct subprocesses, including those on large scales and those on the smaller convective scales. Conversely, latent processes also cool the atmosphere as a result of evaporation, principally near the ground.

Sensible heating involves contact with the ground, as well as transfer of heat between levels within the atmosphere. Much of the transport from the ground takes place by means of turbulent exchanges in the boundary layer, also considered one of the sensible heating processes. Above the boundary layer, sensible heating exchanges are considerably weaker.

Shortwave radiation from the sun peaks in the visible band, near wavelength $0.5\ \mu\text{m}$, whereas longwave processes, that is to say, radiational emission from the Earth, peak in the infrared near $10\ \mu\text{m}$. This difference between the maximum frequency for solar and terrestrial radiation is a result of Wien's law, which states that the wavelength of maximum emission is inversely proportional to the temperature of the emitting body. The principal gases that absorb solar radiation include water vapor molecules of the lower atmosphere and carbon dioxide. The strength of the input solar radiation varies strongly with time of day and season, due to the variability in the angle at which the radiation passes through the atmosphere.

3. Diabatic heating components from runs of the Goddard data assimilation system

Taken from the long-term simulations of the NASA Goddard Laboratory for Atmospheres Data Assimilation System, the diabatic heating components are quite dependent on both latitude and height, as shown by the zonal mean heating in Fig. 3.

Longwave radiational processes produce negative heating everywhere but the strongest areas of this cooling are found just above the earth's surface, in the lower latitude subtropics. Shortwave heating is positive, with strongest values near the lower latitudes and in the lower troposphere. Sensible heating is concentrated near the ground, and reaches a mean rate of nearly $3\ \text{K day}^{-1}$. The value of latent heating has its largest maximum in the tropics near the 500 mb level (also $3\ \text{K day}^{-1}$) due to strong convection there. Secondary maxima occur in the middle to higher latitudes.

A summary of the heating processes may be reviewed by examining maps at each pressure level. For example, sensible heating during January 1986 at the 950-hPa level (Fig. 4) is strong over the Southern Hemisphere continents, where the summer land surface is warm and over the relatively warm currents in the North Atlantic and North Pacific Oceans (the Gulf Stream and the Kuroshio, respectively).

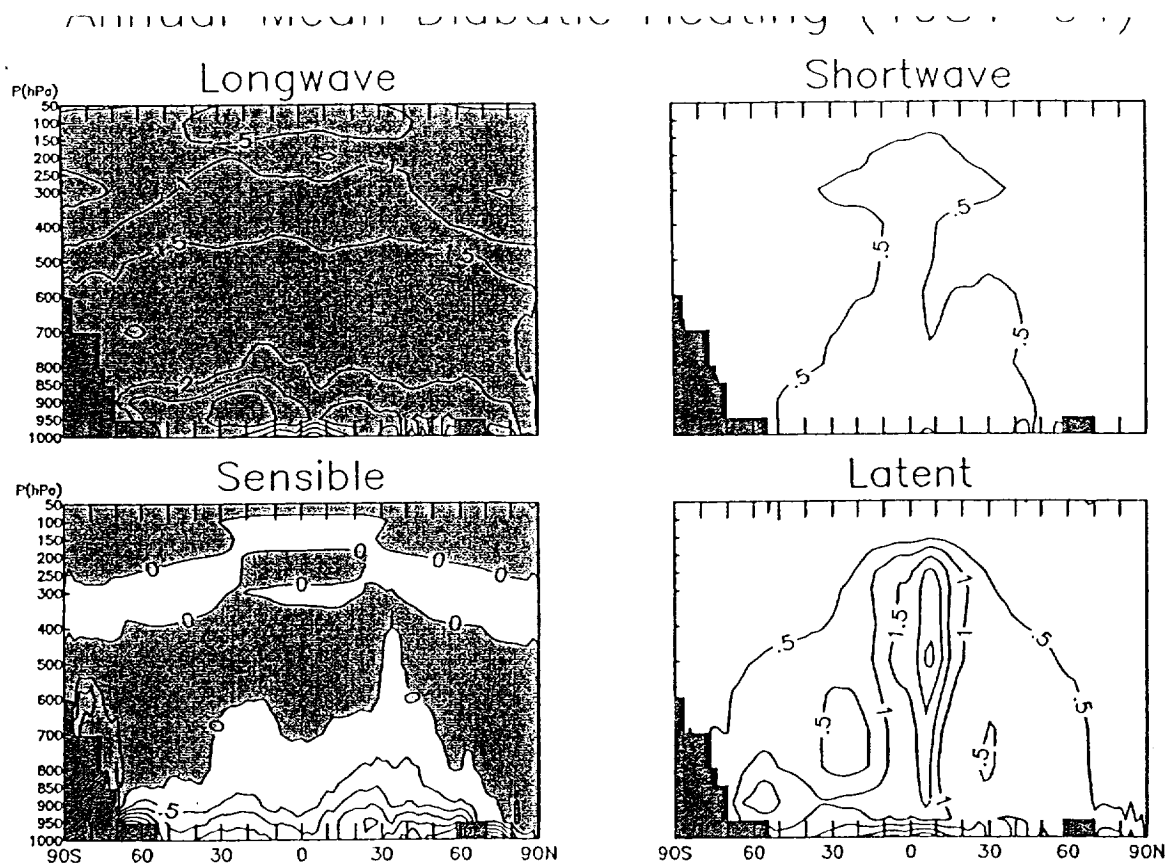


Fig. 3. Zonal mean values of the four forms of diabatic heating for the mean period 1981-1994, based on the NASA GEOS-1 Data Assimilation System. Units are K day^{-1} .

Sensible Heating 950 hPa, January 1986

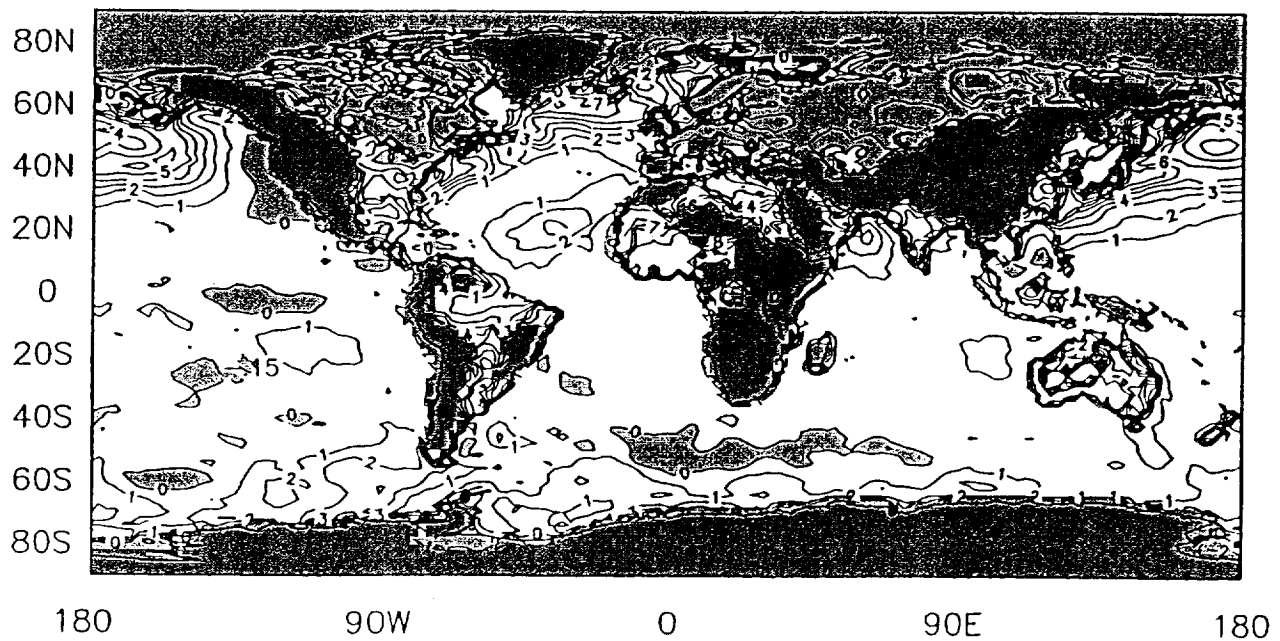


Fig. 4. Mean sensible heating for January 1986 at the 950-hPa level from the NASA GEOS-1 Data Assimilation System. Units are K day^{-1} .

The latent processes within the model, in particular, are sophisticated, and involve complex motions with cloud convection schemes (Arakawa and Schubert, 1974; Sud and Walker, 1993). At higher levels, near 400-500 hPa, very deep convection produces strong latent heating over areas including the western tropical Pacific and maritime continent (Indonesia), across to India, and over much of the areas close to the equator. Minima in latent heating occur in the sub-tropics, in the region of reduced convection near the descending portions of the mean meridional circulation cells, like the Hadley circulation. Further poleward, maxima in the latent heating rates occur again, with the middle latitude values resulting from shallower convective activity and large-scale cloudiness, though some deeper convection can occur there too.

The zonal and vertical mean heating can be understood in the synthesis in Fig. 5 in which a meridional profile of all four terms and the total are given. In this case (for a January period), the latent heating is clearly strongest, and essentially, contains the shape of the total, whereas the longwave process provides negative heating throughout. Indeed, the longwave, shortwave and sensible processes appear very nearly to cancel, providing reconfirmation of the importance of the latent heating.

Interestingly, keeping track of the diabatic heating, particularly the sensible heating throughout the diurnal cycle is important too. The strong value of sensible heating occurs around local noon over the continents (e.g., for the southern hemisphere, Australia at 6 UT, Africa at 12 UT, and South America at 18 UT). It is important thus to maintain the records several times per day to get a complete picture of the heating and energy balance of the atmosphere.

4. Generation of available potential energy

Although diabatic heating yields energy input into the whole system, how the heating is distributed within the system is important to whether it can be transformed to other forms of energy. If the diabatic heating distribution is applied uniformly, it will tend to raise the temperature of a large area evenly. Although the total energy of the system would be modified in this case, in the form of internal energy, this additional energy cannot be released into the kinetic energy form, which requires heating by uneven horizontal gradients to increase the "available potential energy (APE)" of the system. The APE relates to the differences in temperature (density) of air particles all located at the same geopotential level. When such differences in temperature gradient exist, the atmosphere can potentially rearrange its state by air movements to eliminate such a gradient; in this case the available potential energy would be converted into kinetic energy, and, in so doing, tend to eliminate the temperature gradient on the same equipotential.

For APE to increase requires the distribution of diabatic heating to be positively correlated with the temperature field on a given equipotential surface. In that case, the areas that start warmer than the spatial temperature mean will become relatively warmer yet, while the colder areas will increase their relative negative temperature anomaly because of a heating deficit. Thus, the combined spatial distribution of heating and temperature is instrumental to the generation of APE from diabatic heating.

As described above, the values of the sensible, latent, and shortwave radiational heating components all generally decrease from equator to poles, and they are thus positively correlated with the mean temperature pattern. Because of this distribution, their actions lead to act to increase the existing meridional temperature gradient, and in so doing have the capacity to increase the potential energy available for the atmosphere to convert to kinetic energy. Conversely, longwave radiation is negatively correlated with

Diabatic Heating

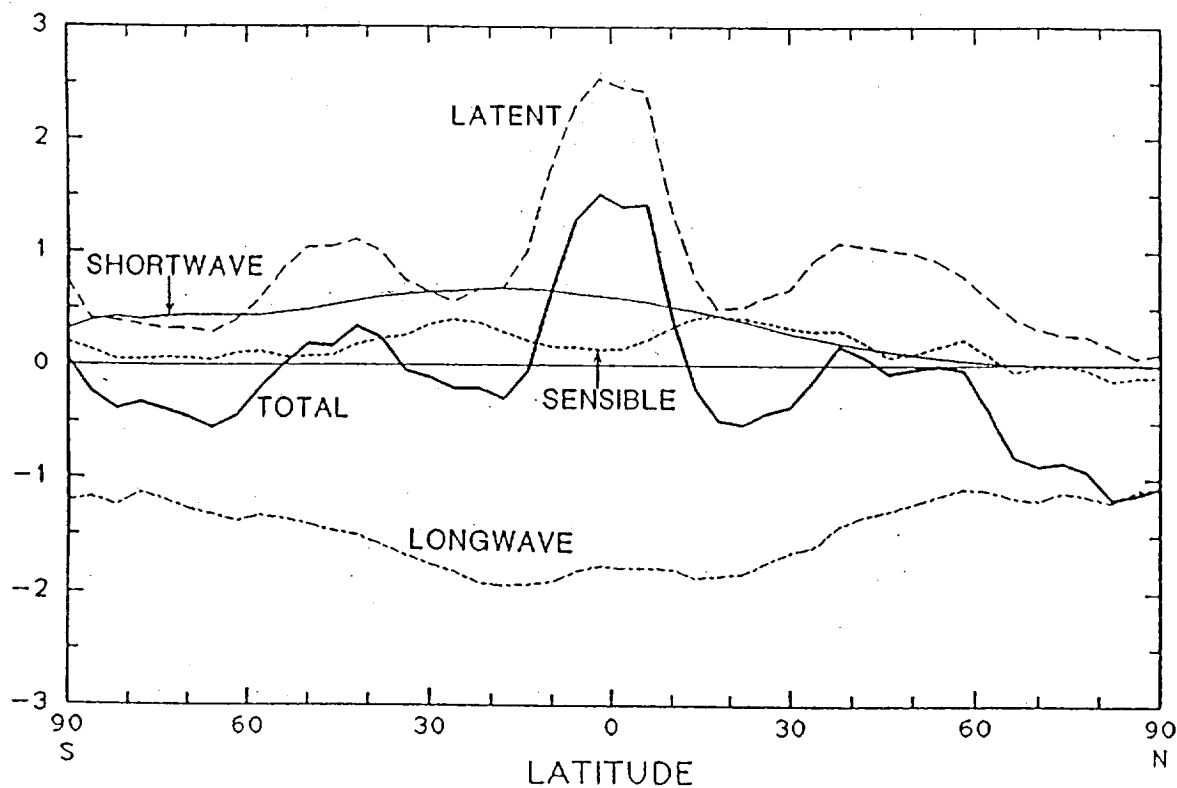


Fig. 5. The vertical mean components of diabatic heating and total heating for a January month, based on the NASA Goddard Data Assimilation System. Units are K day^{-1} .

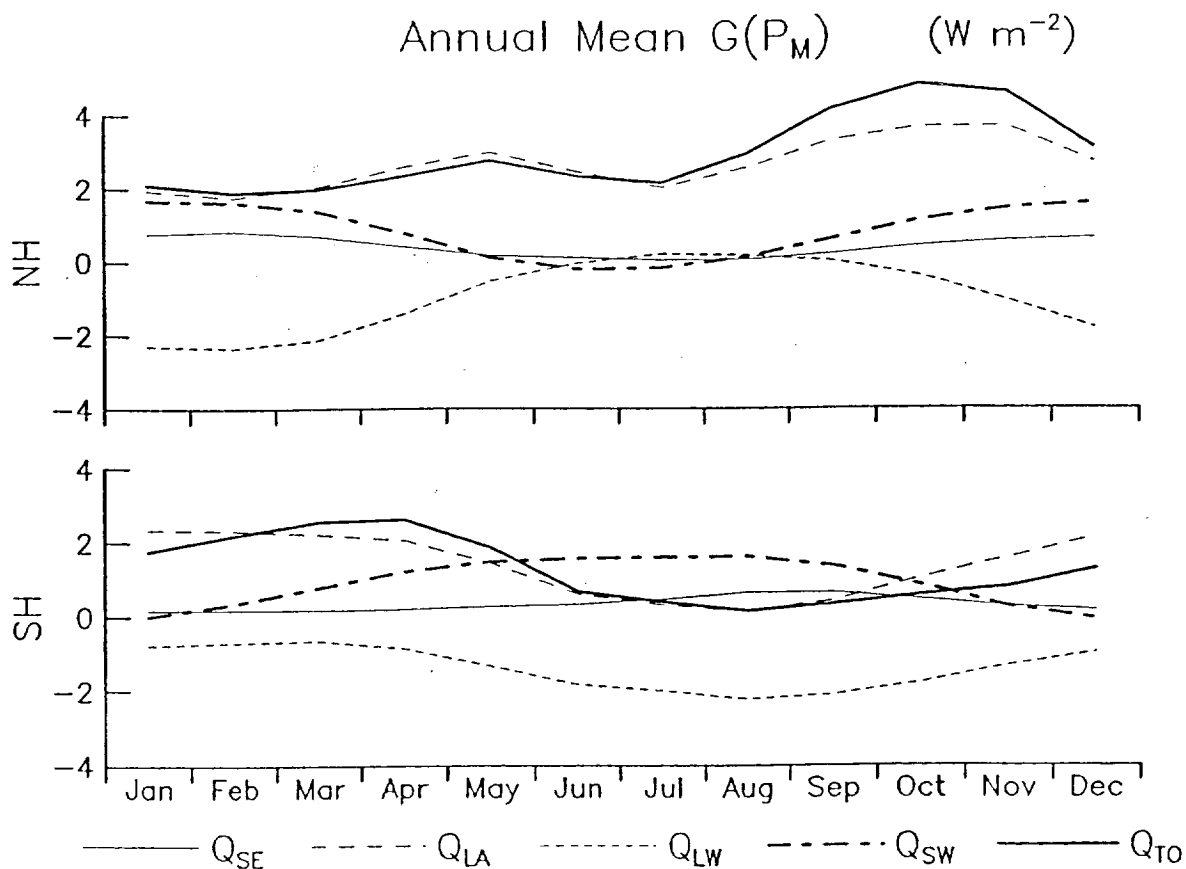


Fig. 6. Mean annual signal for the generation of zonal mean available potential energy between 1980 and 1995 from each of the diabatic heating (Q) components. Here SE=sensible; LA=latent; LW=longwave; SW=shortwave; TO=total). Units are W m^{-2} .

temperature, cooling in relatively warm areas, and vice versa. Longwave radiation thus acts to reduce this potential energy. Nevertheless, the reduction due to the longwave term is less than those of the other three diabatic heating terms, and so, overall, the meridional distribution of heating helps to maintain the energy cycle of the atmosphere's general circulation.

Available potential energy can be generated by the zonal mean state, or it can be generated by the action of eddies, either transient or standing. To calculate the generation of zonal mean APE requires the use of the anomalous temperature and heating fields. From an analysis of the generation of APE between 1980 and 1995 with the NASA Goddard data assimilation system, the effect of sensible, shortwave and longwave tend to cancel, while the generation $G(\text{APE})$ due to latent heating is rather close to that of the total. There are anomalies at the months around the El Niño/La Niña cycles in 1982-1984 and 1986-1987. The annual mean values for $G(\text{APE})$ from the four processes for the two hemispheres is given in Fig. 6 and also shows how the total signal is similar to the latent contribution alone.

5. Role of the generation of available potential energy in the energy cycle

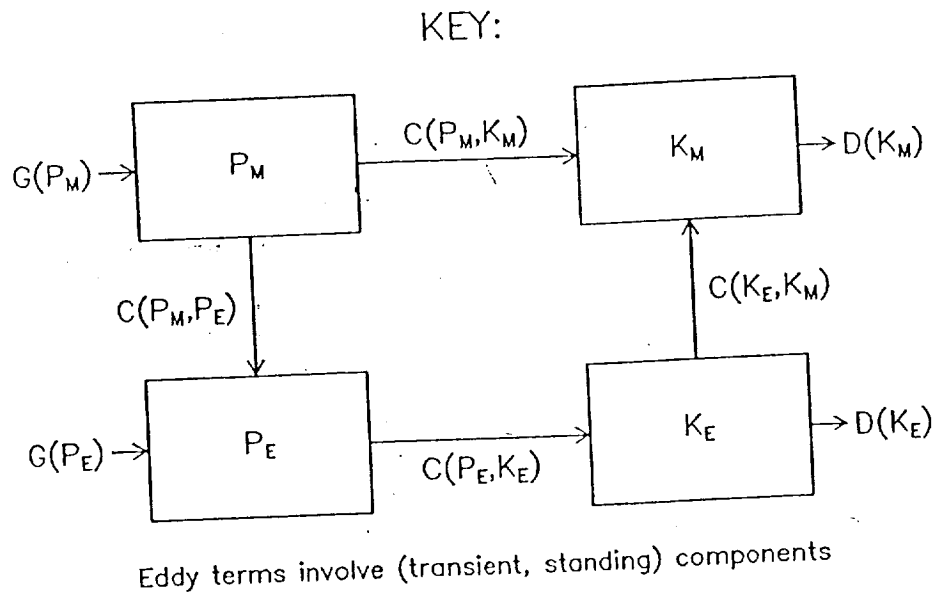
The energy of the atmosphere can be viewed as generated to be available potential energy from the diabatic heating fields, in either mean or eddy forms, and converted to kinetic energy by the act of eddies or by mean atmospheric overturning. A view of these processes is given in the energetics flowchart in Fig. 7 (top). Given a computer simulation of the atmosphere using the data assimilation system of the NOAA Geophysical Fluid Dynamics Laboratory, we can determine many of these energetics numbers and we show them in Fig. 7 (bottom). We also determine, by residual means in the sense of Fig. 7b, the generation of available potential energy for this period in both the zonal mean and eddy forms (bottom lines in both parts of Table 1). The top sets in Table 1 show the generation of available potential energy from each of the components of diabatic heating, from the NASA Goddard Laboratory for Atmospheres system. The zonal mean values, $G(P_M)$, are stronger than the eddy values, $G(P_E)$, but, again, the latent heating component is the largest in both forms.

The sum of the contributions from all four components can be compared with the values from residual method. Given the uncertainties in all these numbers and the fact that the total diabatic involves values of both signs, the two methods produce relatively close values. It is still uncertain, however, which technique of the two is better to use to determine values for the generation of available potential energy.

6. Summary

Energy, like angular momentum and mass, is a property of the atmospheric system subject to conservation, which was a fundamental view in Prof. Peixoto's work. In this light, we turned to estimates of the diabatic heating of the atmosphere to understand how the energy from this heating is distributed throughout the atmosphere and drives the atmospheric energy cycle through the generation of available potential energy.

However, the components of diabatic heating can only be determined with the aid of a modern analysis-forecast system, and to do so adequately requires calculations several times per day. By looking at the diabatic heating in this way, we can also examine the generation of APE in zonal mean and eddy forms, and we are led to an understanding of how the different processes are responsible for driving the general circulation. Latent heating has a particularly strong role in the generation of available potential energy.



Global Energetics

GFDL

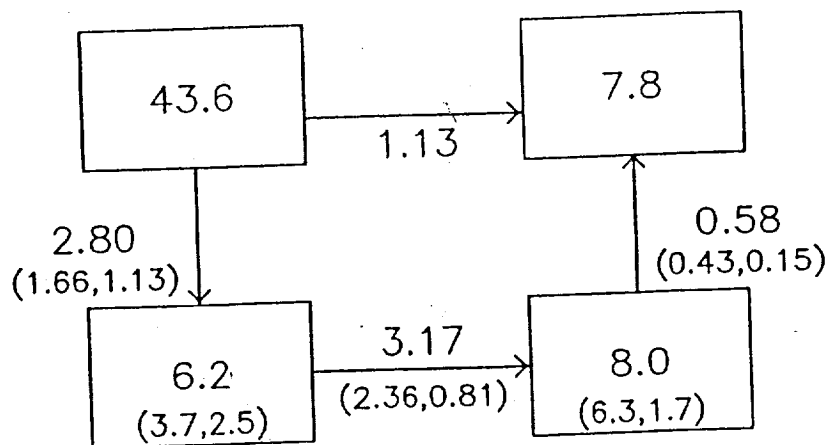


Fig. 7. (a) Key for the energy cycle involving available potential energy (P) and kinetic energy (K) terms). Subscripts M and E indicate zonal mean and eddy forms. Conversions (C terms;) are from the first quantity to the second quantity written in parentheses. G and D indicate generation and dissipation terms respectively. (b) Values for the energy (units 10^5 J m^{-2}) and conversion (units W m^{-2}) terms in the energy cycle for the globe, according to the key in (a), from the NOAA Geophysical Fluid Dynamics Data Assimilation System.

Acknowledgments. The author wishes to acknowledge the kindness and hospitality of his Portuguese hosts during the symposium. The United States National Aeronautics and Space Administration (NASA) supported the research through contract NAS5-98179.

References

- Arakawa, A., and W. H. Schubert, 1974: Interaction of cumulus cloud ensemble with the large-scale environment, Part I. *J. Atmos. Sci.*, 31, 674-701.
- Oort, A.H., 1974: On estimates of the atmospheric energy cycle, *Mon. Wea. Rev.*, 11, 483-493.
- Peixoto, 1959; O campo da divergência do transporte do vapor da agua na atmosfera. *Revista da Faculdade de Ciências de Lisboa*, 2A, Ser. B, Vol. VIII, pp. 25-56.
- Peixoto, J.P. and A.H. Oort, 1992: *Physics of Climate*, AIP Press, 520 pp.
- Rosen, R.D., 1993: The axial momentum balance of Earth and its fluid envelope. *Surveys in Geophysics*, 14, 1-29.
- Schubert, S., R. Rood, and J. Pfaendtnr, 1993: An assimilated data set for Earth science applications, *Bull. Am. Meteorol. Soc.*, 74, 2331-2342.
- Starr, V.P., and J.P. Peixoto, 1965: The hemispheric eddy flux of water vapor and its implications for the mechanics of the general circulation. *Archiv. Fur Meteorologie, Geophysick und Bioklimatologie*.
- Sud, Y.C. and G.H. Walker, 1993: A rain evaporation and downdraft parameterization to complement a cumulus updraft scheme and its evaluation using GATE data. *Mon. Wea. Rev.*, 121, 3019-3039.

$G(P_M)$

Shortwave	1.66
Longwave	-3.05
Sensible	0.49
Latent	3.72
Total diabatic	2.82
<hr/>	
Residual method /GFDL	(3.92)

$G(P_E)$

Shortwave	0.11
Longwave	-0.31
Sensible	-0.07
Latent	0.56
Total diabatic	0.29
<hr/>	
Residual method /GFDL	(0.37)

Table 1. The generation of zonal mean (M) and eddy (E) available potential energy over the globe from each of four heating components and the total diabatic heating for an annual period, based on the NASA GEOS-1 Data Assimilation System. The lowest line of each part indicates the generation terms based on a residual method (using the GFDL system) for a similar period. Units are $W m^{-2}$.

Generation of APE (by Latent), Mean Jan. (W kg^{-1})

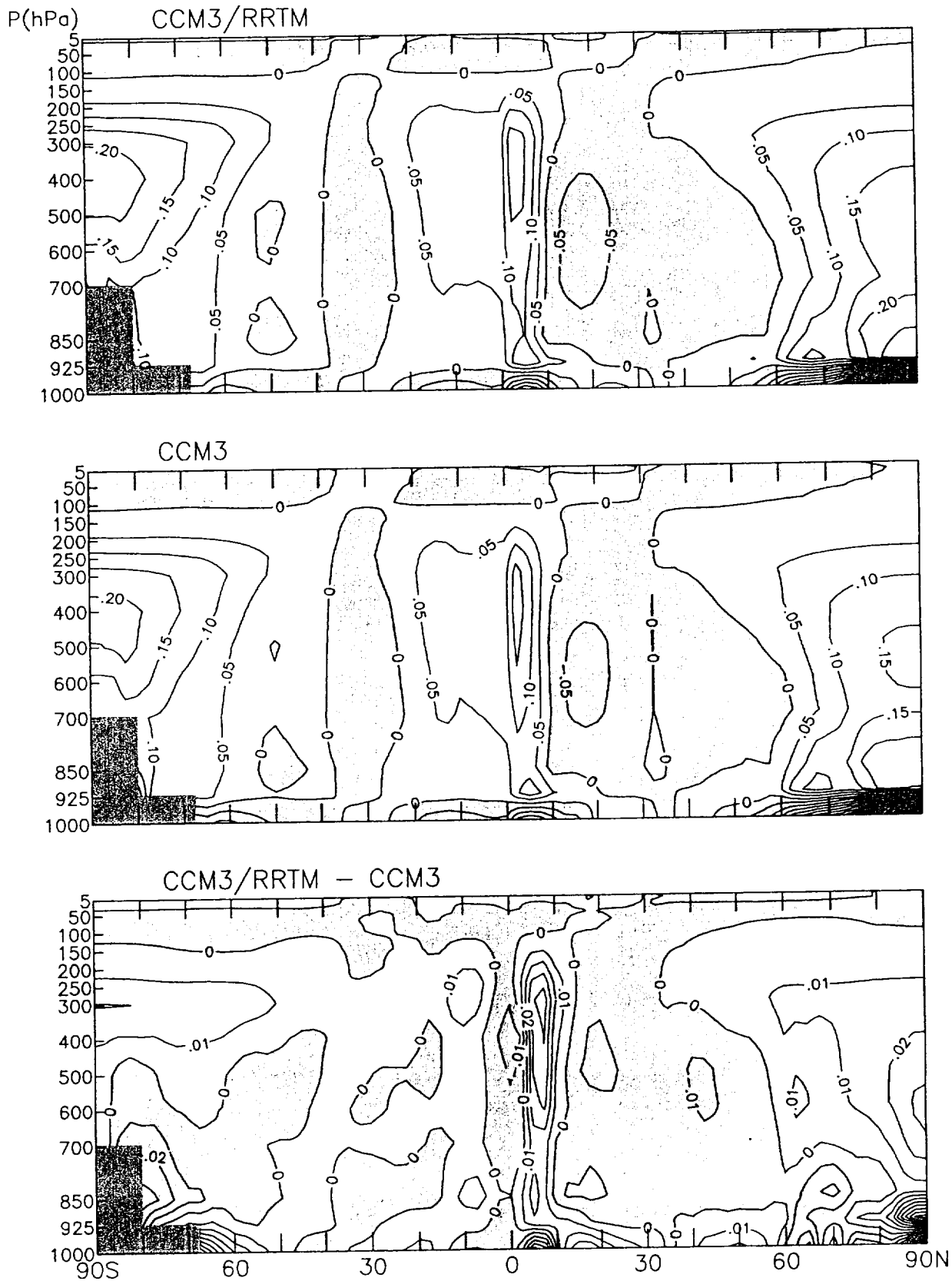


Fig. 3a.1

7. Abstract for paper to appear in Geophysical Research Letters

A dynamical framework to understand and predict the major Northern Hemisphere climate mode

Judah Cohen, David Salstein and Kazuyuki Saito

The dynamics of the leading mode of boreal winter and its excitation by varying boundary conditions remain mostly unclear. A novel framework is presented to explain the evolution of this dominant winter mode. It is shown that there exists a dichotomy of pathways with the characteristics of the dominant mode dependent upon the pathway taken. All winters examined fall into one of the two different dynamic evolutions presented, the knowledge of which clarifies prior uncertainties associated with the dominant mode and provides excellent potential for the successful prediction of subsequent winter mean climate states.

REPORT DOCUMENTATION PAGE			Form Approved OMB No. 0704-0188	
Public reporting burden for this collection of information is estimated to average 1 hour per response, including the time for reviewing instructions, searching existing data sources, gathering and maintaining the data needed, and completing and reviewing the collection of information. Send comments regarding this burden estimate or any other aspect of this collection of information, including suggestions for reducing this burden, to Washington Headquarters Services, Directorate for Information Operations and Reports, 1215 Jefferson Davis Highway, Suite 1204, Arlington, VA 22202-4302, and to the Office of Management and Budget, Paperwork Reduction Project (0704-0188), Washington, DC 20503.				
1. AGENCY USE ONLY (Leave blank)		2. REPORT DATE November, 2001	3. REPORT TYPE AND DATES COVERED: Final Report, October 14, 1998 to October 14, 2001	
4. TITLE AND SUBTITLE Momentum and energy assessments with NASA and other model and data assimilation systems			5. FUNDING NUMBERS NAS5-98179	
6. AUTHORS David Salstein, Peter Nelson, Wenjie Hu				
7. PERFORMING ORGANIZATION NAME(S) AND ADDRESS(ES) Atmospheric and Environmental Research, Inc. 131 Hartwell Avenue Lexington, MA 02421			8. PERFORMING ORGANIZATION REPORT NUMBER P0785	
9. SPONSORING/MONITORING AGENCY NAME(S) AND ADDRESS(ES) National Aeronautics and Space Administration Goddard Space Flight Center Greenbelt, MD 20771			10. SPONSORING/MONITORING AGENCY REPORT NUMBER	
11. SUPPLEMENTARY NOTES				
12a. DISTRIBUTION/AVAILABILITY STATEMENT			12b. DISTRIBUTION CODE	
13. ABSTRACT (Maximum 200 words) Aspects of the angular momentum cycle, energetics, and related diagnostics from a number of models, including some from the Goddard Laboratory for Atmospheres, and from the Atmospheric Model Intercomparison Project (AMIP) are examined. Torques that dynamically excite changes in angular momentum, including strong torques at mountains were studied. The measure of how atmospheric mass from a strong weather signal can notably change the angular momentum is studied. For AMIP, there is a spread in the angular momentum amongst models, while the GLA model does reasonably well compared to the other models in the diagnostics examined, namely angular momentum and water vapor. Trends and interannual variability in water vapor over a lengthy period was examined. The role of the diabatic heating components, especially latent heating, in the energy cycle and the terms converting available potential energy to kinetic energy, among other parts of the energy cycle, are studied. Modes of climate of the atmosphere, especially the Arctic and North Atlantic Oscillations are analyzed as well.				
14. SUBJECT TERMS			15. NUMBER OF PAGES 70	
			16. PRICE CODE	
17. SECURITY CLASSIFICATION OF REPORT Unclassified	18. SECURITY CLASSIFICATION OF THIS PAGE Unclassified	19. SECURITY CLASSIFICATION OF ABSTRACT Unclassified	20. LIMITATION OF ABSTRACT Unlimited	